ALTERNATIVE METHODS TO FABRICATE AND EVALUATE COPPER ZINC TIN SULFIDE BASED ABSORBER LAYERS ON TRANSPARENT CONDUCTING ELECTRODES

by

Prashant Kumar Sarswat

A dissertation submitted to the faculty of
The University of Utah
in partial fulfillment of the requirements for the degree of

Doctor of Philosophy

Department of Metallurgical Engineering

The University of Utah

August 2012

The University of Utah Graduate School

STATEMENT OF DISSERTATION APPROVAL

The dissertation of **Prashant Kumar Sarswat**

has been approved by the following supervisory committee members:

Michael L. Free	, Chair	**5/21/2012** Date Approved
Michael S. Moats	, Member	**5/21/2012** Date Approved
Zhigang Zak Fang	, Member	**5/21/2012** Date Approved
Hong Yong Sohn	, Member	**5/21/2012** Date Approved
Agnes Ostafin	, Member	**5/21/2012** Date Approved

and by **Jan D. Miller**, Chair of the Department of **Metallurgical Engineering**

and by Charles A. Wight, Dean of The Graduate School.

ABSTRACT

This study is focused on fabrication and characterization of Cu_2ZnSnS_4 (CZTS) films on transparent conducting substrate. CZTS films were synthesized using solution based methods. A specially designed sequential and single stage electrochemical method as well as spin coating method was used to grow layers of precursors. Deposition of constituent metallic layers was carried out on SnO_2/F (Fluorinated tin oxide or FTO) coated glass substrates. The electrodeposited/spin coated layers were annealed in a sulfur environment to obtain CZTS. Structural, morphological and optical characterization experiments were performed using several techniques including x-ray diffraction, Raman and UV-visible spectroscopy, scanning electron microscopy, and atomic force microscopy. All characterization experiments indicated the films are single phase with a measured direct band gap of ~1.5 eV.

Photocurrent response of CZTS film grown on FTO substrate was measured using alternating front illumination and rear illumination in a Eu^{3+}/Eu^{2+} solution environment. The photoelectrochemical response exhibited during rear illumination is comparable to that obtained for front illumination. The promising photocurrent data for CZTS films suggest these films have potential application in a variety of photovoltaic devices.

A comparative study revealed that photoelectrochemical response exhibited by the films grown on molybdenum substrate is greater than that obtained for film grown on FTO substrate. A modified form of the Gärtner model to explain J-V characteristics for

CZTS-electrolyte solution has been proposed. Fundamental information such as energy band gap-temperature relationship and temperature dependent study of Raman 'A' mode for CZTS thin films were also investigated in this research.

DEDICATED TO ALMIGHTY

TABLE OF CONTENTS

LIST OF TABLES

LIST OF FIGURES

PUBLICATIONS AND PRESENTATIONS

List of publications related to this thesis

[1] P K Sarswat, M L Free, and A Tiwari, "Temperature Dependent Raman Study of CZTS (Cu_2ZnSnS_4) thin film" *Phys. Status Solidi B* 248 (2011) 2170.

[2] P K Sarswat and Michael L Free, "A Demonstration of Sol - gel Synthesized Bifacial CZTS-Photoelectrochemical cell" *Phys. Status Solidi A* 208 (2011) 2861.

[3] P K Sarswat, M L Free, A Tiwari, and M Snure, "CZTS Thin Films on Transparent Conducting Electrodes by Electrochemical Technique" *Thin Solid Films* 520 (2012)1694.

[4] P K Sarswat and M L Free, "An Evaluation of Energy Band Gap versus Temperature for CZTS Absorber Material", *Physica B* 407 (2012)108.

[5] P K Sarswat and M L Free, "An Evaluation of Depletion Layer Photoactivity in Cu_2ZnSnS_4 Thin Film", *Thin Solid Films* 10.1016/j.tsf.2012.02.066 (2012).

[6] P K Sarswat and M L Free, "A Comparative Study of Co-electrodeposited CZTS Absorber Material on FTO and Molybdenum Substrate", *Journal of Electronic Materials* 2012 DOI: 10.1007/s11664-012-2042-5.

[7] P K Sarswat, M L Free, and A Tiwari, "A Study of Increased Resistivity of FTO Back Contact for CZTS Based Absorber Material Grown by Electrodeposition-Annealing route", *Mater. Res. Soc. Symp. Proc. Vol. 1315,* Boston, USA, 2010.

[8] P K Sarswat, M L Free, and A Tiwari, "A Factorial Design of Experiments Approach to Synthesize CZTS Absorber Material from Aqueous Media", *Mater. Res. Soc. Symp. Proc. Vol. 1288,* Boston, USA, 2010.

List of presentations related to this thesis

[1] "Adhesion Study of CZTS Layer Deposited from Ink Type Precursor onto a Back Contact for Photovoltaic Applications" by P K Sarswat and M L. Free, *Materials Research Society (MRS) 2011 Fall meeting*, Boston, MA, USA.

[2] "Processing Parameter Optimization to Synthesize High Quality Single Phase CZTS Film" by P K Sarswat , M L Free and A Tiwari, *The Minerals, Metals and Materials society (TMS) 2011 Annual meeting* ,San Diego, CA, USA.

[3] "A Study of Increased Resistivity of FTO Back Contact for CZTS Based Absorber Material Grown by Electrodeposition-Annealing Route" by P K Sarswat, M L. Free and A Tiwari, *Materials Research Society(MRS) 2010 Fall meeting*, Boston, MA, USA.

[4] "A Factorial Design of Experiments Approach to Synthesize CZTS Absorber Material from Aqueous Media" by P K Sarswat, M L Free and A Tiwari, *Materials Research Society(MRS) 2010 Fall meeting*, Boston, MA, USA.

[5] "Surface Characterization of CZTS Absorber Layers Synthesized by Solution Based Methods" by P K Sarswat, M L. Free and A Tiwari, *NanoUtah 2010 Symposium* Salt Lake city, UT, USA.

ACKNOWLEDGEMENTS

I would like to express my sincere thanks to my supervisor, Prof. Michael L. Free, for encouragement, guidance, and support during course of this dissertation research. I also want to extend thanks to Prof. H. Y. Sohn, Prof. Z. Z. Fang, Prof. M. Moats, and Prof. A. Ostafin for valuable advice and comments on different aspects of my research. I am also very thankful to Makrand Karmarkar, Michael Snure, Jiajia Tan, Vishal Gupta, Dr. K. Samantha, Prof. Ashutosh Tiwari, Soumya Kar and Yakun Zhu for help in various stages of my research. Thanks are also due to all working staff of Department of Metallurgical Engineering. Finally, I would like to express my deep love and thanks to my parents, my family members, and my wife.

CHAPTER 1

INTRODUCTION

Considerable attention has been given in recent years to sustainable development of energy resources. Specific attention has been given to renewable energy resources as an alternative to fossil fuels, which are a major source of CO_2 emission. Among various renewable energy sources solar energy can be categorized as a very promising source. However, the cost of electricity production from photovoltaic cells is much higher than that from fossil fuels. Another challenge is that the power conversion efficiency of photovoltaic devices is low. Most photovoltaic devices utilize silicon, which generally comes from expensive single crystal wafers.

The requirement of a thick ~ 100 μm silicon absorber layer (thick due to the low absorption coefficient of silicon), combined with the typical high temperature processing to make single crystal silicon, makes single crystal silicon solar cells expensive. Consequently, single crystal Si solar cell electricity production is very low compared to that produced by fossil fuels. Thin film solar cells, which are not made from silicon, are projected to be less expensive than silicon based solar cells. Amongst thin film solar cells, CIGS (copper indium gallium selenide/sulfide), CdTe (cadmium telluride), and a-Si (amorphous silicon) are the most popular solar cells. Though these cells are commercially

produced, certain issues such as limited availability of rare elements and the toxicity of cadmium need to be addressed before large production is feasible. Copper zinc tin sulfide/selenide (CZTS) is emerging as a wide band gap p-type quaternary chalcogenide for use in inexpensive, efficient, and environmentally friendly, thin film solar cells for which the needed materials are readily available for large scale production. It is a direct band gap material with a band gap energy of ~1.5 eV and a very high absorption coefficient of ~ 10^4 cm^{-1}. Although most of the research carried out for CZTS absorber material is in an early stage, significant energy conversion efficiency ~ 9% has been reported by IBM [1]. To date most of the CZTS based solar cells have been fabricated by evaporation or sputtering followed by annealing and sulfurization at elevated temperatures (250-550 ^{o}C). It is believed that the cost effectiveness of these cells can be further improved by developing alternate processing techniques such as solution based, high-throughput electro-chemical techniques.

1.1 Motivation and objectives

The primary goal of this research is to develop solution processable CZTS solar cell fabrication techniques for synthesis on substrates which are alternative to the conventional molybdenum-coated glass substrates. The feasibility of CZTS thin film fabrication on transparent conducting oxide (TCO) substrate has been systematically examined. There are various issues related to this targeted research such as film quality, phase purity, stability of CZTS phase, band gap of the film, and morphology associated with solution based techniques. Apart from these goals, another major task is an evaluation of optical and semiconductor properties of the CZTS film produced by

methods utilized in this research. Because CZTS is a new photovoltaic material, there are various parameters and properties that are unexplored. Hence, there is an urgent need for extensive research focusing on these parameters. Although most of the work in this piece of research is based on CZTS film grown on FTO substrates, some focus on comparison with films grown on molybdenum and FTO is essential.

1.2 Research organization

Chapter 2 is a background and literature survey related to CZTS absorber material.

Chapter 3 discusses synthesis and characterization of CZTS film on a transparent conducing electrode using sequential electrodeposition and elevated temperature annealing. A detailed study related to film quality and morphology as well as optical properties is conducted for solution processable synthesis of CZTS films.

Sequential electrodeposition is a three-step time consuming process; hence in order to save time, a recipe for co-deposition of Cu-Zn-Sn on FTO substrate from a single bath is needed. A detailed study to analyze film quality and optical properties of single bath deposited films is discussed in Chapter 4.

Chapter 5 discusses sol-gel processing technique for CZTS film growth on FTO substrate. Bifacial photovoltaic performance of the CZTS photoelectrochemical cell is evaluated.

A comparative study is also desirable to identify the differences between film grown on FTO and molybdenum substrates. Some of the important parameters which are examined and compared in Chapter 6 are: film quality, morphology, phase purity, optical property and most importantly, photovoltaic properties.

Electrical properties of CZTS on FTO back contact are essential and need to be examined. High series resistance causes reduced device performance (such as low power conversion efficiency and reduced fill factor). Correspondingly, Chapter 7 discusses a study related to sheet resistance of FTO film before and after sulfurization.

Chapter 8 discusses depletion layer photoactivity of CZTS thin films. CZTS films were examined in Eu^{3+}/Eu^{2+} electrolyte to evaluate various analytical expressions for photocurrent response as a function of applied potential. Various existing models and relevant fitting parameters, which consider charge transfer (across the double layer) were evaluated.

Chapter 9 discusses temperature a dependent Raman study of 'A' mode vibration for CZTS absorber material. A detailed quantitative analysis showed that the Raman data for the "A" mode of vibration, the strongest peak for kesterite CZTS films, fit very well to a damped harmonic oscillator (DHO) model.

Chapter 10 discusses the energy band gap-temperature relationship for CZTS absorber material. Near band edge transition with respect to temperature is an important parameter for optimizing the performance with respect to operating temperatures of CZTS based photovoltaic devices, which can vary significantly daily and seasonally.

Chapter 11 discusses contact engineering of CZTS-back contact interface.
Finally, a summary of all results and future work is discussed in chapter 12.

1.3 Reference

[1] T. K. Todorov, K. B. Reuter, and D. B. Mitzi, Adv. Mater. 22 (2010) E156.

CHAPTER 2

BACKGROUND AND LITERATURE REVIEW

2.1 Working principle of photovoltaic (PV) cells

The term 'photovoltaic' is used for material that can convert sunlight or photon energy into electricity. A photovoltaic cell (or solar cell) is a semiconductor device in which combinations of semiconducting materials are used to fabricate a device. The principle is that incident photons of sufficient energy create electron-hole pairs, which are separated due to built-in electric field. The most common device is a p-n junction device. Most of the time silicon (c-Si or a-Si) is used for photovoltaic energy generation. Though silicon has numerous advantages as a photovoltaic material, the requirement of thick wafers ~ 200μm and the high cost of manufacturing has resulted in a search for alternative photovoltaic materials. An alternative technology, "thin film PV technology" is becoming popular because of its dramatic materials savings (less than $1/50^{th}$ of the thickness of c-Si) and easier synthesis methods. Thin semiconducting layers are commonly deposited on low cost substrates (such as soda lime glass) coated with a back contact material. Thin film PV material possesses high light absorptivity. The most common materials for thin film solar cells (apart from silicon) are cadmium telluride (CdTe), copper indium diselenide ($CuInSe_2$) and copper indium gallium selenide

($CuIn_xGa_{(1-x)}Se_2$) [1]. A relatively new thin film photovoltaic absorber material 'CZTS' is discussed in this report.

2.2 CZTS Crystal structure

Copper zinc tin sulfide crystallizes in three phases, namely, kesterite (space group $I\bar{4}$), stannite (space group $I\bar{4}2m$) and the primitive mixed CA structure (PMCA) (space group $P\bar{4}2m$). Of these three phases, kesterite and stannite are most widely studied. Kesterite consists of a cubic closed packed (ccp) array of sulfur atoms, with metal atoms occupying one half of the tetrahedral voids. Crystallization of stannite-type compounds occurs in the tetragonal space group $I\bar{4}2m$ (D_{2d}^{11}) with two formula units in each unit cell. Although kesterite and stannite-type structures are widely studied, kesterite is thermodynamically the most favorable phase. In this work, analyses are done assuming CZTS as kesterite. Some physical properties of kesterite CZTS absorber is shown in Table 2.1. The lattice parameters for kesterite crystal structure are: a = 0.54 nm and c = 1.09 nm. A kesterite crystal structure is shown in Figure 2-1. The p type conductivity of CZTS thin films is due to Cu_{Zn} antisite (copper atoms occupy the sites of zinc atoms)[2].

Table 2.1 CZTS properties

Physical property	Value
Molar mass	439.471
Density	4.56 gm/cm^3
Bandgap	1.4-1.5 eV

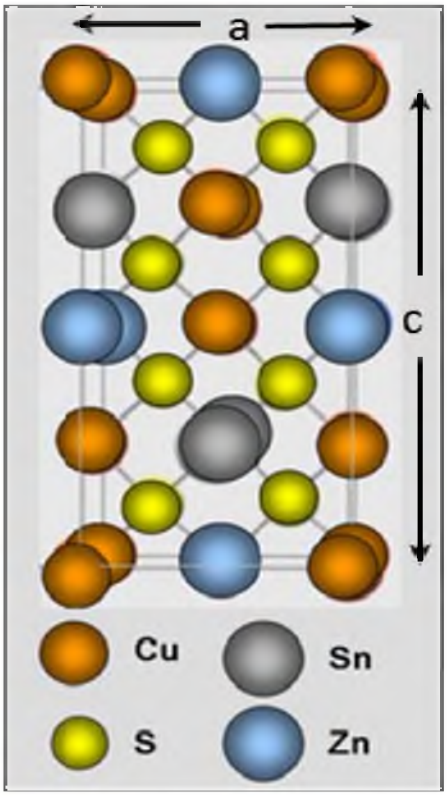

Figure 2.1: CZTS kesterite crystal structure.

2.3 Band gap of photovoltaic material

The energy difference between the top of the valance band and bottom of the conduction band of semiconductor is known as the band gap. It is assumed that there is no electronic state within the band gap. In other words this is an amount of energy required to liberate electron from the valance band to the conduction band. The solar spectrum contains low energy infrared photons, high energy ultraviolet photons along with visible light photons. Photovoltaic material response lies in a very narrow range of this spectrum, which is directly related to the band gap of the material. Incident photons of energy lower than the band gap escape unabsorbed while photons of higher energy create electron hole pairs and thermal energy. Therefore, solar cells with low band gap material are desirable. This is one of the reasons why c-Si solar cell with a band gap of ~1.1 eV is most popular and widely used. However, for large voltage solar cells a high band gap material is needed [1]. An effective band gap range that coincides with the solar spectrum is 1.1-1.7eV. CZTS photovoltaic material has a band gap of ~ 1.5 eV; thus it has a desirable band gap for photovoltaic applications [2]. It is estimated that most solar cells provide a maximum of only ~ 33% of the incident solar in the form of electricity production. The rest of the energy from original sunlight is lost.

2.4 CZTS thin film nonvacuum fabrication techniques

Despite the great potential as an absorber material, the research on fabricating thin film solar cells using CZTS is still in a very primitive stage. To date most of the CZTS based solar cells have been fabricated by evaporation or sputtering followed by annealing and sulfurization at elevated temperatures (250-550 ^{o}C). Nonvacuum techniques such as

spray pyrolysis, solvo-thermal, and SILAR (successive ionic layer adsorption and reaction)/chemical bath deposition (CBD) have also been reported [3]. In the spray-pyrolysis synthesis technique an aqueous solution of salts containing copper, zinc, tin and thiourea (source of sulfur) is used [4]. This solution is further sprayed on a heated substrate. A pneumatically controlled air-atomizing spray nozzle is used for spraying. During CBD processing the substrate is immersed in an aqueous solution of the precursors. The growth rate and morphology of film depend on various factors such as duration of deposition, bath composition and bath temperature. For deposition of sulfide salts a typical chemical bath contains ammonium hydroxide, thiourea and the salts of the precursors. The SILAR technique is a modified form of the chemical bath deposition technique in which successive layers of zinc sulfide, tin sulfide, copper sulfide, and sodium sulfide are deposited sequentially using different baths [4]. The stoichiometry of film can be adjusted by manipulating immersion time and changing the deposition sequence. After each adsorption step rinsing with deionized water is performed. This technique suffers from high chemical consumption.

It is believed that the cost effectiveness of these cells can be further improved by developing alternate solution processing techniques particularly electrochemical and sol-gel methods. These techniques are cost-effective and can produce high throughput with minimum wastage of chemicals. Recently, Mitzi *et al.* [5] reported fabrication of a CZTS based PV (Photovoltaic) device, synthesized from a solution based method, with significant efficiency ~ 9.3%.

Several research groups have recently attempted production of CZTS thin films using electrochemical methods. For example, Zhang *et al.* [6] reported synthesis of CZTS on

Ag-substrates by Electrochemical - Atomic Layer Epitaxy, while Araki *et al.* [7-9] and Scragg *et al.* [10] reported the preparation of CZTS films on molybdenum coated glass substrates by electroplating; Chan *et al.* [11] reported the synthesis of CZTS thin films on copper coated glass substrates using ionic liquids. To obtain the desired 2:1:1:4 stoichiometry of Cu:Zn:Sn:S in sulfurized films, proper control of the molar stoichiometric ratio of Cu:Zn:Sn in the electrodeposited film is required. Scragg *et al.* [10] reported the requirement of a nonstoichiometric initial metal composition of Cu/(Zn+Sn) ~ 0.7 to 1.1 with a Zn/Sn ratio of 1.0 for production of high quality of CZTS.

The sol-gel process, another solution based technique, utilizes hydrolysis and condensation reactions for precursor growth [12]. In this method generally hydrated precursors (of Cu, Zn and Sn) are coated on a substrate by spin coating. The coated substrate is then dried and annealed. Resulting films are sulfurized at elevated temperature to obtain CZTS. This method is inexpensive compared to other complicated vacuum based methods [12]. This method allows fine control of the product composition. Another advantage is allowance for a small quantity of dopants that can be introduced in the sol, which can be uniformly dispersed in the final coating.

2.5 CZTS based thin film solar cell fabrication

A conventional CZTS based thin film solar cell consists of ZnO:Al/ZnO/CdS/CZTS/Mo/Soda lime glass structure as shown in Figure 2.2 [13]. A front contact mesh of Ni/Al was evaporated on top of an aluminum doped zinc oxide layer. This device structure is very similar to that utilized for CIGS based thin film solar

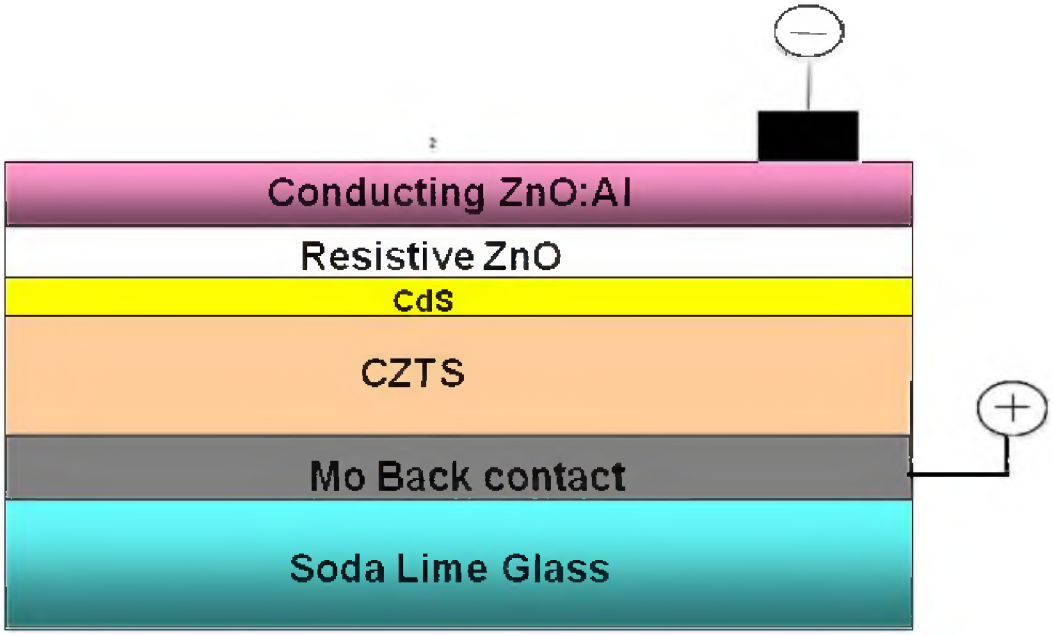

Figure 2.2: Conventional CZTS based photovoltaic device

cells. Figure 2.2 represents a schematic diagram of such a device. Sputtered molybdenum (thickness ~ 700 nm) coated glass substrate is often used for fabrication of such a device. Advantages of molybdenum back contact are discussed in another section. An absorber layer (p-type) semiconductor is required next to the back contact.

CZTS, a p- type absorber material, can be coated by various techniques including thermal evaporation and solution based techniques. The thickness of absorber layer coating is ~ 1 micron. A n-type emitter layer (of thickness 50 nm) such as CdS can be grown on top of the CZTS layer by chemical bath deposition. A ZnO top layer is generally deposited using magnetron sputtering. In many cases an anti-reflection coating of MgF_2 is also deposited. Ni-Al mesh is utilized as a contact grid [13]. In some cases a protective layer is also provided, such as glass lamination.

2.6 Photovoltaic device operation

Thin film solar cells are effectively semiconductor diodes that contain a p-type absorber layer and an n-type emitter layer. When light of appropriate wavelength and sufficient energy encounters this layer, an exciton (electron –hole pair) is generated near the active depletion layer. In other words, quantized excitation by an electromagnetic field causes electron hole pair generation. Some electron-hole generation also occurs because of thermal energy. The generation of electron- hole pairs depends on the band gap energy of the absorber layer. In ideal cases this generation occurs only when the energy of the photon is greater than the band gap. A junction between p-type and n-type layers separates some of the holes from the electrons because of the internal electric field of the diode structure [14]. However, recombination of electrons and holes also takes place in this process. The holes move upward energetically and the electrons move downward energetically across the junction on application of load.

Other details can be understood by examining a real solar cell internal circuit as shown in Figure 2.3. A solar cell can be understood as an ideal diode with light induced current. Therefore, it can be represented as a current source which is connected with an ideal reverse biased p-n junction diode. Some loss is encountered due to resistance of the external circuit. However, a series of cells can be used to reduce these losses. The recombination of electrons and holes is included by considering some shunt resistance (R_{sh}). Because recombination causes some short circuiting of current, a reduced output is expected. A high value of shunt resistance is a characteristic of a good photovoltaic device, because it will in turn increase availability of high power output to the load.

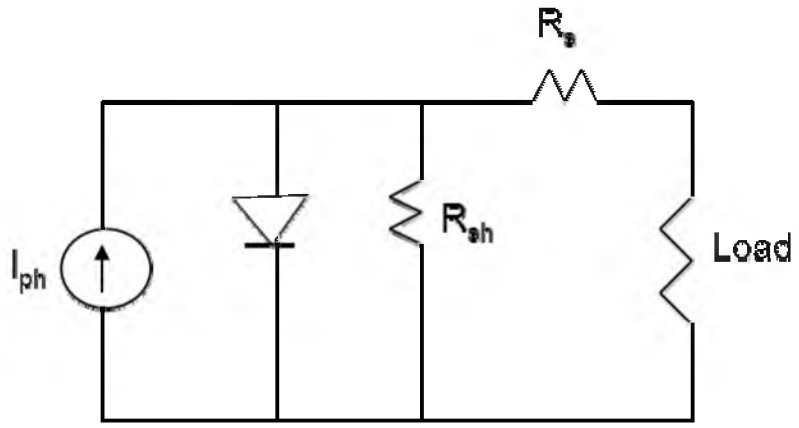

Figure 2.3: A typical photovoltaic device circuit diagram

However, a low value of series resistance (R_s) is needed for good photovoltaic performance.

2.7 Photovoltaic device characteristics

The current-voltage or I-V behavior of a PV device follows the one diode equation. According to this model, current during forward bias increases exponentially while current is very small during reverse bias voltage scanning. Additional current flow can be seen when a PV device is illuminated due to drift of generated charge carriers in an electric field. Photovoltaic performance of device is evaluated by examining I-V characteristics under standard illumination (incident power ~ 100mW/cm^2) [1]. Generally for this purpose, a solar simulator, which has spectral output very similar to that of solar spectrum, is used. To maintain standardization, current is reported as current/unit area or mA/cm^2. There are various important terms essential to understand. The open circuit voltage (V_{oc}) is the voltage at the zero current condition. It is the maximum voltage produced by a PV device. The short circuit current (I_{sc}) is the current through a PV device

at zero bias condition. The short circuit current depends on various factors such as area of the solar cell and number of incident photons. Fill factor (FF) is the ratio between maximum power delivered to an external circuit and the potential power.

$$FF = \frac{P_{\max}}{V_{oc} I_{sc}} \tag{2-1}$$

Power conversion efficiency of a photovoltaic device can be defined as:

$$\eta = \frac{V_{oc} I_{sc} FF}{P_{in}} \tag{2-2}$$

where P_{in} is the incident power input to the PV device. A schematic diagram is shown in Figure 2.4.

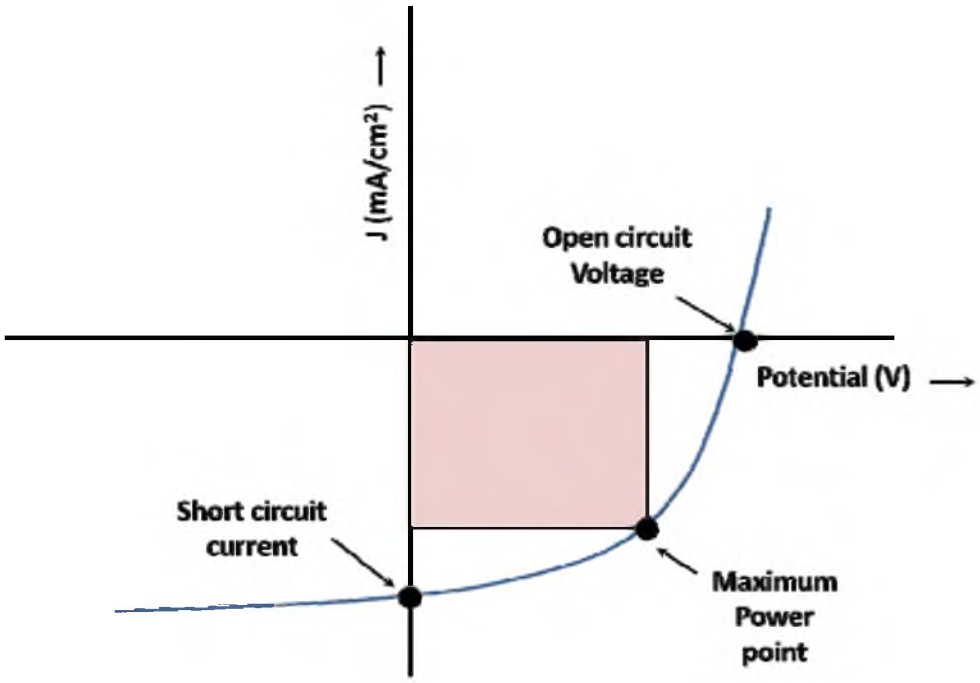

Figure 2.4: A typical photovoltaic device I-V curve

2.8 Substrate used for CZTS film growth

Most of the time molybdenum coated on soda lime glass has been utilized for CZTS photovoltaic device fabrication [13]. However, other substrates are reported [15,16]. Some efforts are given to fabricate flexible PV device by roll to roll manufacturing. Tian *et al.* [15] utilized molybdenum coated aluminum foil for flexible CZTS PV device fabrication. Zhou *et al.* [16] fabricated a flexible CZTS PV device on molybdenum coated polyamide film.

2.9 Phase stability

CZTS synthesis conditions must be carefully controlled in order to avoid formation of other phases that have greater thermodynamic stability. A first principle study by Nagoya *et al.* [17] shows that the allowed chemical potential domain for the CZTS phases for copper rich condition is very small (see Fig 2.5). Furthermore, the area of this confined domain is reduced at low copper activity levels. It can be seen that the CZTS phase stability region is surrounded by various sulfide phases such as copper sulfide, tin sulfide, zinc sulfide and copper tin sulfide.

2.10 Microstructure and grains study of CZTS

A new study reveals that grain boundaries in CZTS are not effective recombination centers or sites for electrons [18]. First principle simulation results also strengthen this assumption [18]. A noncontact atomic force microscopy study was performed to record spatial maps of topography and surface potential of CZTS [18]. It was observed that surface potential at grain boundaries is higher than at the surface of grains. A relative

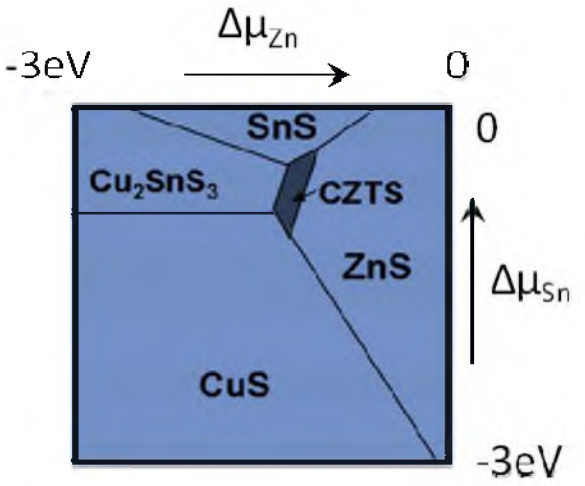

Figure 2.5: A schematic diagram (drawn from reference [17]) showing CZTS phase stability region.

positive grain boundary potential causes attraction of electrons (p-type semiconductor) towards the grain boundary. Contact mode AFM reveals that current flow in the grain boundary area is greater than in the rest of the grains. Such evaluations reveal that grain boundaries in CZTS act as current channels rather than recombination centers. Most of the CZTS solar cells suffer from secondary phase formation, which causes reduced device efficiency [18].

Scragg *et al.* [19] synthesized CZTS on molybdenum substrates by electrodeposition-sulfurization. Their CZTS samples show some evidence of the ZnS phase as revealed by a lighter area in SEM imaging. An external quantum efficiency measurement also reveals that copper deficient precursors are beneficial for effective films. It was also observed that copper rich precursors results in formation of secondary phases such as Cu_xS and Cu_2SnS_3. It is important to note that the presence of ZnS in the film causes reduction in total active area of material and hence overall reduction in efficiency. Though

sulfurization of as deposited film can be done by H_2S, we adopted evaporation of elemental sulfur for sulfurization. It is reported that fine grains of size ~1μm grow in the case of evaporated sulfur –sulfurization. However, film sulfurized in an H_2S environment results in large grains (diameter ~5μm). The carrier concentrations of H_2S annealed films were nearly half of those films that were annealed in evaporated sulfur.

Chan *et al.* [11] reported synthesis of CZTS using ionic liquids. Electrodeposition has been carried out in chloride media and choline chloride. Annealing was carried out using evaporated sulfur at a temperature of 450°C. It was observed that large grains formed (diameter ~2μm). It was also reported that thicker film (with thickness great than 5μm) results in poor adhesion to the substrate.

CZTS films grown on molybdenum substrate show various pores adjacent to the CZTS/Mo interface. A MoS_2 layer has also been reported between CZTS and Mo back contact. Formation of Cu_2SnS_3 has been reported close to the Mo/MoS_2 interface [20].

2.11 Effects of KCN etching

It has been observed that a KCN etch helps to remove secondary phases such as copper sulfide from CZTS thin films. KCN etching also improves external quantum efficiency (EQE) of CIGS solar cells. A widening of surface band gap of CZTS absorber materials was reported due to KCN etching [21]. It was also observed that increased interface band gap acts as enhanced energy barriers which help to prevent charge carrier recombination [21]. Removal or dissolution of secondary phases by KCN is a two-step process. Potassium cyanide reacts with copper sulfide and forms copper cyanide, which forms a cyanide complex with excess potassium cyanide [22].

$$Cu_2S + 2KCN \rightarrow 2CuCN + K_2S$$

$$2CuCN + KCN \rightarrow KCu(CN)_2$$

This type of complex formation is known for transition metals of the first subgroup such as: Cu, Ag and Au. Other metals such as thallium and mercury also form cyanide complexes, which are less stable than those of silver and copper.

2.12 Incorporation of sodium

Sodium incorporation sometime increases the efficiency and reliability of solar cells. Samples on borosilicate glass delaminate frequently compared to that on sodalime glass [23]. Reducing deposition temperature can help to mitigate delamination. Grains larger than 1 micron are formed for the Na exposed sample; however some smaller grains and porosity are also present. Larger grains and/or very Na rich conditions may be more susceptible to evaporation of CZTS or some of its components, especially from grain boundaries. Plasma cleaning of the surface before CZTS deposition also improves quality of the interface.

2.13 Fluorinated tin oxide as an alternative back contact

A transparent conducting film (TCF) coated glass substrate is not only useful as a supporting structure but it also provides a pathway for illumination and part of the device encapsulation. TCFs for photovoltaic applications can be fabricated from both inorganic and organic materials. Inorganic films are generally made up of a layer of TCO (transparent conducting oxide), such as indium tin oxide (ITO), fluorine doped tin oxide

(FTO), and doped zinc oxide. Transparent materials possess band gaps with energies corresponding to wavelengths that are shorter than the visible range. As such, photons with energies below the band gap are not collected by these materials and thus visible light passes through. Current transport in these oxides arises from three fundamental sources: interstitial metal ion impurities, oxygen vacancies, and doping ions. In the visible region, the optical transmission of FTO is high (»90%) and independent of the fluorine doping. The superstrate configuration using ZnO and FTO has been examined for Cu (In, Ga)Se_2 (CIGS) absorber layer [24]. Generally a molybdenum back contact coated on a glass substrate has been utilized for fabrication of CIGS solar cells. This configuration gives power conversion efficiency as high as ~ 19%. Haug *et al.* [24] discussed the advantages of an alternative transparent back contact for CIGS solar cells and reported low manufacturing cost, use in tandem solar cells, and utilization of the short wavelength part of the solar spectrum. It was reported that quasi-ohmic behavior exhibited by an FTO-CIGS junction makes it possible to use it as an alternative to a molybdenum back contact. The work of Nakada *et al.* [25] suggests possible fabrication of semitransparent CIGS thin film solar cells for top tandem and bifacial devices using SnO_2/F (FTO) as a back contact. Nakada *et al.* [25] reported CIGS PV fabricated directly on FTO coated glass substrates, at temperatures less than 520 °C, had performance that is comparable to devices fabricated on Mo coated substrates.

While there has been published literature for CIGS superstrate solar cells (here glass is above the all active layers), there is need for investigation for transparent back contact-CZTS solar cells. These solar cells will be more useful for places where availability albedo radiation is high (Figure 2.6). In addition, these devices will be more

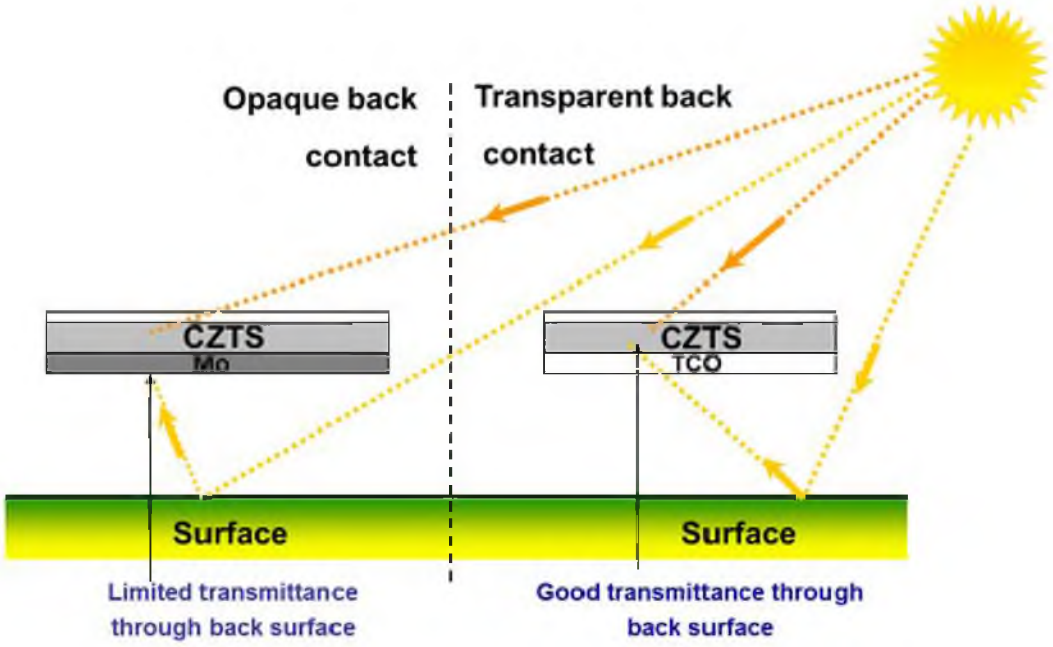

Figure 2.6: A schematic diagram showing comparison of CZTS based monofacial device using Mo back contact and bifacial device using transparent conducing back contact.

prone to electron–hole pair generation during simultaneous, dual side illumination.

2.14 CZTS-FTO Band alignment

CZTS absorber material is being widely accepted as a "p-type" material. Consequently, the Fermi stabilization energy can be assumed to be close to the valence band maximum. An ohmic contact between p-type CZTS and back contact is desirable for good solar cell performance. Spies *et al.* [26] concluded that according to Schottky barrier theory, ohmic contact between CIGS and high work function metal is impossible.

However, the formation of $MoSe_2$ at the molybdenum- CIGS interface promotes ohmic contact. The Schottky barrier height should be zero or negative for ohmic contact formation [26]. Similarly for CZTS, back contact blocking is reported due to the Schottky barrier, which prevents hole transport across Mo to the absorber layer [13]. An estimated barrier height ~ 0.32 eV was reported. It was observed that in the case of the CZTS-Mo junction, formation of thin MoS layer promotes lowering of the barrier height. This results in CZTS-Mo interface behavior close to ohmic. However, no information is available for the CZTS –FTO interface.

2.15. FTO-CZTS contact behavior

To determine FTO-CZTS contact behavior current-voltage (I-V) characteristics were examined. Room temperature I-V characteristics (Figure 2.7) reveal that contact between FTO and CZTS is not perfectly ohmic as indicated by the slight nonlinearity in the I-V data. However, it is a quasi ohmic contact, as expected. Rectifying behavior is not observed. These observations suggest that FTO can be used as a back contact for fabrication of CZTS based thin film solar cells.

2.16. Characterization of CZTS absorber material

This section discusses some details about characterization techniques that have been utilized to investigate phases, morphology, electronic and electrochemical properties of CZTS absorber materials. XRD and Raman spectroscopy were utilized to investigate phase purity of thin film, while SEM and AFM were utilized to investigate microstructure

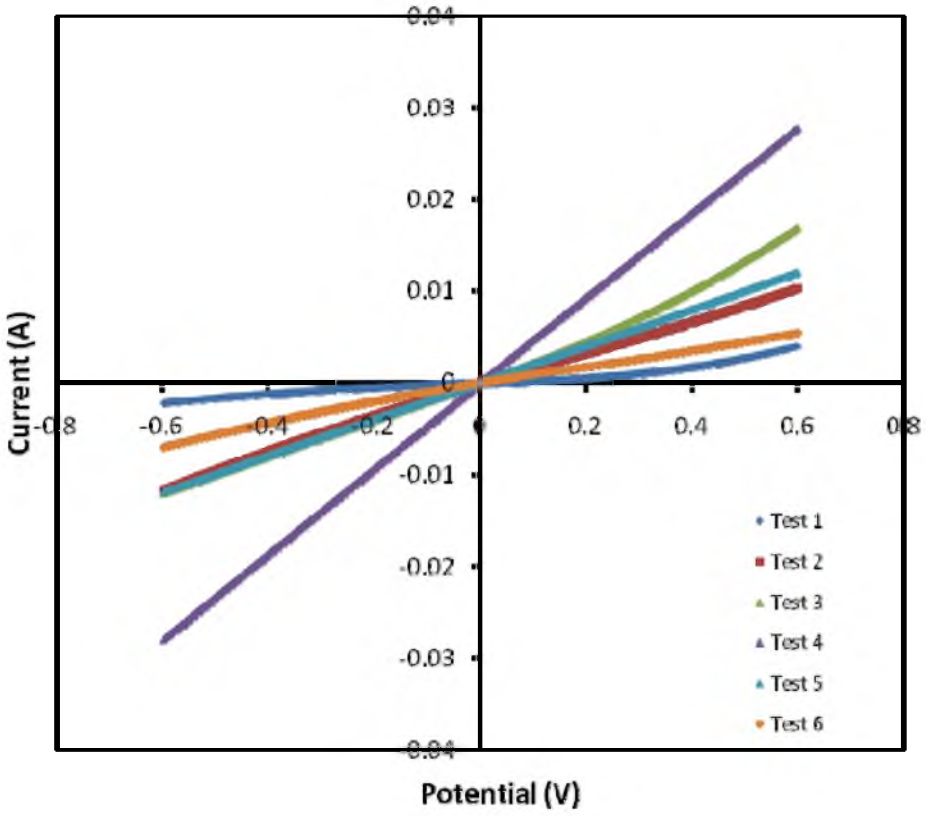

Figure 2.7: I-V characteristics of CZTS –FTO contact; Different I-V characteristics are observed for tests for different interfacial sulfur thickness.

and film quality evaluations. UV-Vis spectroscopy was utilized to determine the fundamental band gap of CZTS. Electrochemical tools such as Mott-Schottky analysis were used to investigate doping density, flat band potential, and charge carrier type. The hot probe method was also used to determine majority charge carrier type.

2.16.1 X-ray diffraction (XRD) technique

XRD is a nondestructive technique that provides material property information such as crystal structure, lattice parameters, grain size and the presence of secondary phases

[27]. For this technique a short wavelength of a few angstroms is used, which is comparable to the lattice dimension of most crystals. When X-rays collide with atoms some of the rays are deflected from their original path. There is generation of secondary EM waves during scattering through a regular array of atoms. Most of these waves cancel out due to destructive interference between waves, while in certain directions these waves interfere constructively. Thus, the resultant intensity distribution in these specific directions is very high compared to other directions. Bragg's law is used for interpretation of X-ray data. According to Bragg's law:

$$2dSin\,\theta = n\lambda \tag{2-3}$$

where d is the spacing between diffracting planes, θ is incident angle, n is an integer, and λ is the wavelength of excitation. XRD scans were run using a Philips X'Pert XRD diffractometer with Cu Kα radiation over the 2θ range 20–80°. Step sizes of 0.005° and a receiving slit size of 1/8° were used in order to achieve high resolution.

2.16.2 Raman spectroscopy

Raman spectroscopy is a good tool to investigate photon-matter interaction for evaluation of various properties [28]. In this technique, during inelastic interaction of monochromatic light and material the final energy of laser photons shifts either up or down. The resulting shift contains information such as vibrational and rotational transitions in the matter. The laser beam, which is a source of sinusoidal EM wave, induces a dipole moment, which is directly proportional to molecular polarizability. Such sinusoidal (or periodic) deformation causes vibration of molecules with a characteristic frequency [28]. In other words, it can be said that some of the photon energy is

transferred to the Raman active molecule and the resulting frequency of scattered light is reduced. These Raman lines are known as Stokes lines. In some cases when photons interact with molecules which are already in an excited vibrational state, the resulting frequency of scattered light is enhanced. These Raman lines are known as anti-Stokes lines. It is very important to note that majority of scattered light contains a frequency which is same as that of excitation source due elastic scattering of light. Only a small percentage of scattered light contains information about the Raman mode (for Raman active molecule). Generally a sample is illuminated with monochromatic laser light. Backscattered light from illuminated spot is again collected and sent through a monochromator to obtain a Raman spectrum (Figure 2.8). Raman spectroscopy requires minimal sample preparation steps and very useful for wide range of materials. Wet samples, solids and gas, and liquids can be analyzed using this nondestructive technique.

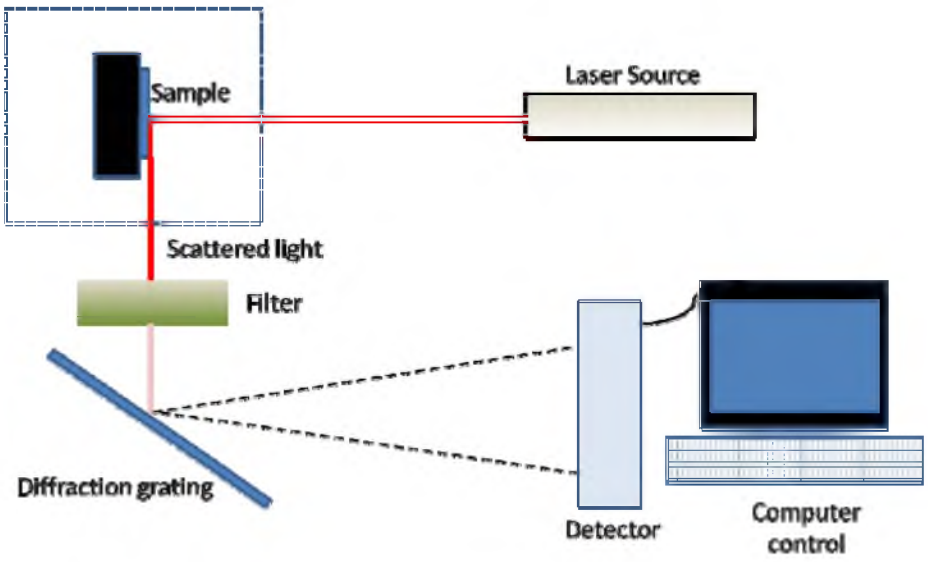

Figure 2.8: A schematic diagram showing a simplified Raman spectroscopy set-up

Raman spectroscopy in this piece of research was carried out by using R 3000 QE portable Raman spectrometer (made by Raman Systems) a 785 nm laser with a power of ~ 140mW used for excitation.

2.16.3 Optical transmission spectroscopy

This technique provides an indication of optical band edge within a semiconducting material [29]. Typically, a fraction of radiation that is transmitted at each wavelength is measured. A sample is illuminated using UV-Vis light source and the spectrum of transmitted light is recorded. In the case of CZTS thin film, it can be useful to provide information related to optical transition. An SD 2000 spectrophotometer was used to record transmission data of CZTS thin film in the range of 300nm-900nm.

Photons of energy greater than semiconductor band gap are absorbed and therefore a change in absorbance is observed. For a direct band gap semiconductor, α obeys the following equation:

$$\alpha(h\nu) \propto \frac{\sqrt{h\nu - E_{gap}}}{h\nu} \tag{2-4}$$

The fitting of a straight line on a plot of the photon energy '$h\nu$' versus $(\alpha h\nu)^2$ and extracting the constant band gap (E_{gap}) term.

Normalized transmission is related with absorption coefficient:

$$T_{normalized} = e^{-\alpha L} \tag{2-5}$$

where α is the absorption coefficient and 'L' is sample thickness.

2.16.4 Hot probe method

This method is a quick way to determine the majority carrier type in a semiconductor [30]. The probes of a potential measuring device are placed on the surface of the semiconductor and one end of the probe is simultaneously heated with a heating device such as a soldering iron. A negative voltage reading when the heat source is placed at the positive lead of voltammeter confirms that majority charge carriers are p-type. Heating of one of the probe causes localized heating of semiconductor also. This causes movement of charge carriers away from the contact point, leading to generation of charge difference between probes (see Figure 2.9). Now consider a p-type semiconductor. Heating of a positive lead causes movement of holes towards the other end (negative lead side). Hence a built-in electric field inside the semiconductor causes a potential difference between probes, which can be read using a voltammeter.

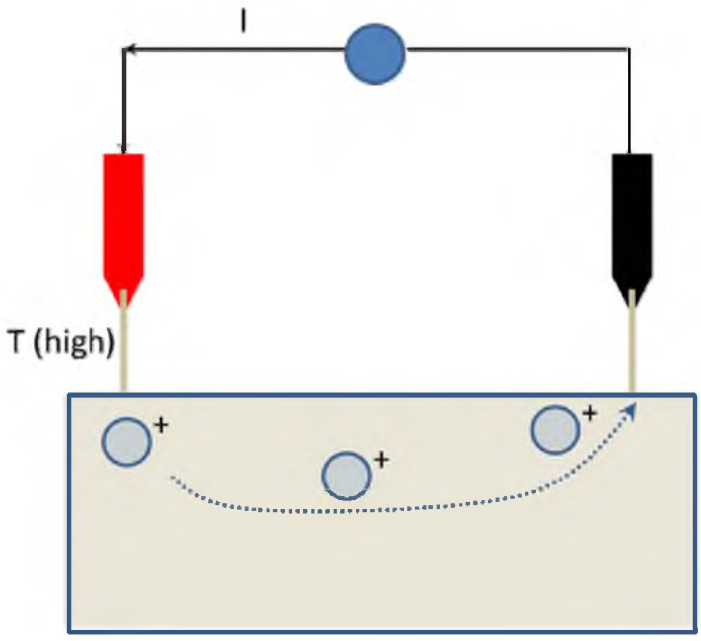

Figure 2.9: Hot probe method for p-type semiconductor. A flow of hole is also shown.

2.16.5 Scanning electron microscopy (SEM)

Scanning electron microscopy was used extensively to examine surface microstructure of CZTS films [31]. An advantage of SEM is that it has a large magnification range of up to ~100000X, which is beneficial for information such as topography, grain size, and film quality. In contrast to optical microscopy, an electron optical system is used for imaging. The resolution of the image is related to the wavelength of electron but also limited to size of interaction volume. A typical resolution of an SEM image is in the range of 5-20 nm.

2.16.6 Atomic force microscopy (AFM)

This technique is generally used for probing fundamental intermolecular force between substances. For most AFMs, the sample is mounted on a piezoelectric scanner, which permits atomic level movements with precision [32]. The sample is scanned in a plane, where force is continuously sensed using a tip attached to a cantilever. The bending or deflection of cantilever depends on the nature of the force that acts between the sample and the tip. This deflection is monitored, and using these raw data a three dimensional topographical image can be created. The most common method for AFM imaging is 'contact mode imaging' where the tip is bought in direct contact with the sample surface. In most of this study contact mode imaging was used for CZTS sample analyses.

2.16.7 Semiconductor electrolyte interface

The Fermi level (a theoretical concept) is used to represent the level of potential energy for an electron inside the crystalline solid. The Fermi level of a semiconductor changes with biasing voltage. Application of more negative potential causes an increase in the Fermi level. When a semiconductor electrode is immersed in redox electrolyte, the redox potential of the electrolyte and the Fermi level of the semiconductor will try to come to the same level by movement of charge carriers [33]. Excess charge carriers within the semiconductor are distributed in a region that extends from a few nm to 1000nm inside the semiconductor. This region is generally known as the space charge layer. The semiconductor and electrolyte system can be understood as an electrical system containing interfacial double layer and a space charge double layer capacitance. For a p-type semiconductor (whose Fermi level is lower than that of electrolyte), downward bending of the band (see Figure 2.10) is observed due to accumulation of

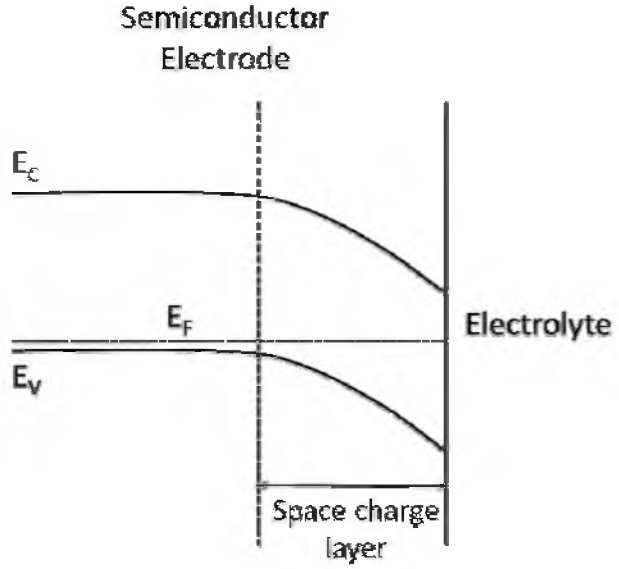

Figure 2.10: A schematic diagram showing band edge when applied potential is less than flat band potential.

electrons. Now consider a situation when there is no band bending. It is possible if movement of charge carriers can be controlled by application of some biasing voltage or potential applied to the semiconductor. A potential when there is no band bending is known as flat band potential. At a potential negative to the flat band potential there is an existence of a depletion layer. However, on the other hand at a potential positive to the flat band potential, an accumulation layer exists and the electrode can act as an anode. Now it should be noted that more and more downward bending is useful for transfer of an electron from the semiconductor side to the solution side. Increased downward bending can be achieved by applying potential more negative to that of the flat band potential. For a p-type semiconductor a decrease of potential (away from the flat band potential and towards negative side) will cause enhancement of the depletion layer width and hence capacitance will increase. Thus the reciprocal of the capacitance will decrease towards the negative side of the flat band potential and it will increase on application of potential greater than the flat band potential. The Mott- Schottky relationship is a generalized equation to represent such behavior [33]. According to this relation, the modulus of the squared reciprocal of capacitance versus potential graph will be approximately a straight line (with positive slope for p-type semiconductor). Figure 2.11 shows such simulated behavior for a p-type semiconductor (Acceptor concentration>Donor concentration). The flat band potential and charge carrier density can be determined from the intercept and slope of the line using proper equations discussed in later section of thesis.

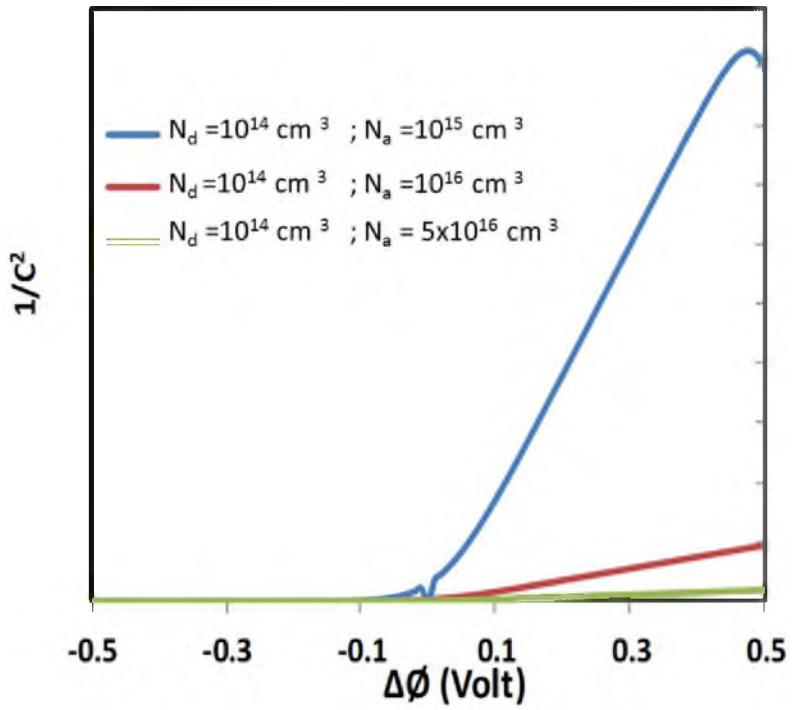

Figure 2.11: A simulated Mott-schottky plot using different value of acceptor concentration

2.17 Fermi level of redox electrolyte

In contrast to crystalline materials, electrons in solution are not free. Electrons are generally bound with the ions in solution, hence the "Fermi level in solution" is not very good nomenclature. Electrochemical potential term is more appropriate. However, the equivalent term for redox couples can be calculated [34]:

$$E_{F\ (redox)} = -4.5\ eV - e_o E_{redox} \qquad (2\text{-}6)$$

where 'E_F' is equivalent Fermi level term, 'e_o' is electronic charge and 'E_{redox}' is redox potential (versus standard hydrogen electrode).

As an example:

Eu^{3+}/Eu^{2+} redox couple: Potential = -1.08 V (versus MSE) ~ -0.40 versus SHE

So E_F = -4.1 eV (Europium redox couple).

For Cr^{3+} / Cr^{2+} redox potential (SHE) = -0.43, E_F = -4.07 eV

We can think using of other redox couple such as Cr^{3+} / Cr^{2+} . Use of cadmium and iron is avoided because of toxicity and precipitation issues.

2.18 References

[1] S. Hegedus and A. Luque, in Handbook of Photovoltaic Science and Engineering, 2nd ed., edited by A. Luque and S. Hegedus (John Wiley and Sons, Chichester, 2011).

[2] S. Chen, J. H. Yang, X. G. Gong, A. Walsh, and S. H. Wei, Phys. Rev. B 81 (2010) 245204.

[3] N. Kamoun, H. Bouzouita, B. Rezig, Thin Solid Films 515 (2007) 5949.

[4] [Sawanta S. Mali, Bharmana M. Patil, Chirayath A. Betty, Popatrao N. Bhosale, Young Woo Oh, Sandesh R. Jadkar, Rupesh S. Devan, Yuan-Ron Ma, Pramod S. Patil, Electrochimica Acta 66 (2012) 216.

[5] T. K. Todorov, K. B. Reuter, and D. B. Mitzi, Adv. Mater. 22 (2010) E156.

[6] X. Zhang, X. Shi, W. Ye, C. Ma, C. Wang, Appl. Phys. A. 94 (2009)381.

[7] H. Araki, Y. Kubo, A. Mikaduki, K. Jimbo, W. S. Maw, H. Katagiri, M. Yamazaki, K.Oishi, A. Takeuchi, Sol. Energ. Mat. Sol. Cells. 93 (2009) 996.

[8] H. Araki, A. Mikaduki, Y. Kubo, T. Sato, K. Jimbo, W. S. Maw, H. Katagiri, M. Yamazaki, K.Oishi, A. Takeuchi, Thin Solid Films 517 (2008) 1457.

[9] H. Araki, Y. Kubo, K. Jimbo, W. S. Maw, H. Katagiri, M. Yamazaki, K.Oishi, A. Takeuchi, Phys. Status Solidi C 6 (2009)1266.

[10] J.J. Scragg, P.J. Dale, L.M. Peter, Thin Solid Films 517 (2009) 2481.

[11] C.P. Chan, H. Lam, K. Y. Wong, C. Surya, Mater. Res. Soc. Symp. Proc. 1123 (2009)06.

[12] K. Tanaka, N. Moritake, and H. Uchiki, Sol. Energ. Mat. Sol. Cells. 91 (2007) 1199.

[13] K. Wang, O. Gunawan, T. Todorov, B. Shin, S. Chey, N. Bojarczuk, D. Mitzi, S. Guha, Appl. Phys. Lett 97(2010) 143508.

[14]. A. Shah, P. Torres, R. Tsharner, N. Wyrsch, H. Keppner, Science 285 (1999) 692.

[15] Qiwei Tian , Xiaofeng Xu , Linbo Han , Minghua Tang , Rujia Zou , Zhigang Chen , Muhuo Yu , Jianmao Yang and Junqing Hu , CrystEngComm DOI: 10.1039/c2ce06552e

[16] Zhihua Zhou, Yanyan Wang, Dong Xu, Yafei Zhang, Solar energy materials and solar cells 94 (2010)2042.

[17] A Nagoya, R Asahi, Phys. Rev. B 81 (2010)113202.

[18] J. B. Li, V. Chawla, and B. M. Clemens, Adv. Mater. 24 (2012) 720.

[19] J.J. Scragg, P. J. Dale, L. M. Peter, Thin Solid Films 517 (2009) 2481.

[20] A. Ennaoui, M. Lux-Steiner, A. Weber, D. Abou-Ras, I. Kötschau, H.-W. Schock, R. Schurr, A. Hölzing, S. Jost, R. Hock, T. Voß, J. Schulze, A. Kirbs, Thin Solid Films 517 (2009) 2511.

[21] M. Bär, B.-A. Schubert, B. Marsen, R. G. Wilks, S. Pookpanratana, M. Blum, S. Krause, T. Unold, W. Yang, L. Weinhardt, C. Heske, and H.-W. Schock Appl. Phys. Lett. 99 (2011)222105.

[22] E. Wiberg, N. Wiberg, A. F. Holleman, in Inorganic Chemistry. Edited by N. Wiberg (Academic Press, London, 2001)

[23] W.M. HLAING Oo, J.L. Johnson, A. Bhatia, E.A. Lund, M.M. Nowell and M.A. Scarpulla, J. Electron. Mater. 40 (2011) 2214.

[24] F. J. Haug, D. Rudmann, A. Romeo, H. Zogg, A. N. Tiwari, 3rd World Conference on Photovoltaic Energy Conversion, May 11-18, 2003, Osaka, Japan, pp-2853-2858.

[25] T. Nakada, Thin Solid Films 480-481 (2005) 419.

[26] J. Spies, R. Schafer, J. F. Wager, P. Hersh, H. Platt, D. Keszler, G. Schneider, R. Kykyneshi, J. Tate, X. Liu, A. D. Compann, W. N. Shafarman, Sol. Energy. Mat. Sol.Cells. 93 (2009)1296.

[27] B. D. Cullity,S. R. Stock in: Elements of X-Ray Diffraction (3rd Edition), Addition-Wesley Publishing Company, Inc. Reading, Massachusetts (1956).

[28] B. Schrader, Infrared and Raman Spectroscopy (VCH Publishers, New York, 1995), p. 414.

[29] Peter Y Yu, M Cardona, in: Fundamental of Semiconductors: Physics and Materials Properties (4^{th} Edition), Springer New York (2010).

[30] S. M. Sze, Physics of Semiconductor Devices, 3rd ed., (Wiley, New York 2006). pp-63-129.

[31] J. Goldstein, D. Newbury, D. Joy, C. Lyman, P. Echlin, E. Lifshin, L. Sawyer, and J. Michael, Scanning Electron Microscopy and X-ray Microanalysis, 3rd Ed., Kluwer Academic/Plenum Publishers, New York (2002).

[32] K. M. Lang, D. A. Hite, R. W. Simmonds, R. McDermott, D. P. Pappas, and John M. Martinis, Rev. Sci. Instrum. 75 (2004) 2726.

[33] R. Memming, Semiconductor Electrochemistry, 1^{st} ed., (Wiley, Weinheim, 2001).

[34] H. Gerischer, W. Ekardt, Appl. Phys. Lett. 43(1983)393.

CHAPTER 3

CZTS THIN FILMS ON TRANSPARENT CONDUCTING ELECTRODES BY ELECTROCHEMICAL TECHNIQUE

3.1 Introduction

Electrochemical techniques are high throughput and very much cost effective for synthesis of quaternary chalcogenide thin film PV materials. Many research groups have reported fabrications of CZTS using electrochemical techniques [1-6]. However, all these reports were for opaque (metal coated glass) substrates. In view of this aspect, electrochemical growth of CZTS on transparent conducting oxide coated glass substrates was done, which is essential for realizing high efficiency tandem and bifacial solar cells.

This chapter discusses the synthesis and characterization of Cu_2ZnSnS_4 on transparent conducting substrate using a specially designed sequential electrodeposition method. Sequential electrodepositon of constituent metallic layers was carried out on SnO_2/F coated glass substrates using a platinum counter electrode and a saturated calomel reference electrode. Unique bath compositions were formulated for each of these constituents. Sequentially deposited tri-layer stacks were annealed in sulfur environment

to get the CZTS phase. Detailed structural, morphological and optical characterization experiments were performed using several techniques including x-ray diffraction, Raman and UV-visible spectroscopy, scanning electron microscopy and atomic force microscopy.

3.2. Experimental details

3.2.1 Electrodeposition of stacked layers

Electrowinning cells enclosed in a water jacket were used to perform the electrodeposition at a controlled temperature of 58°C. FTO coated glass substrates (area exposed to electrolyte = 1.5-2.0 cm^2) were used as the working electrode. Electrodeposition was carried out in potentiostatic mode. Each electrowinning cell contained 50 ml of electrolyte. The deposition sequence of zinc/copper/tin was used for better adhesion [8]. Zinc was electrodeposited as the primary layer, using zinc chloride (0.088M). Sodium potassium tartrate (0.49M) was used as the complexing agent. The second layer, predominantly copper was deposited using a cyanide medium bath [NaCN(1.3M)/Na_2SO_4(0.017M)/ZnCN(0.068M)/$Na_2SnO_3.3H_2O$(0.018M)/CuCN(0.78M)] [9]. The final layer, tin, was deposited using a solution of tin chloride (0.088M) with sodium potassium tartrate (0.49M) as the complexing agent. Pre-investigations were carried out to determine the equilibrium potential for each species. For this we conducted linear sweep scans for each electrolyte mentioned above (using SnO_2/F coated glass as the working electrode). Results from linear sweep voltammetry shown in Figure 3.1 indicate the equilibrium potential for SnO_2/F coated glass in zinc plating solution to be

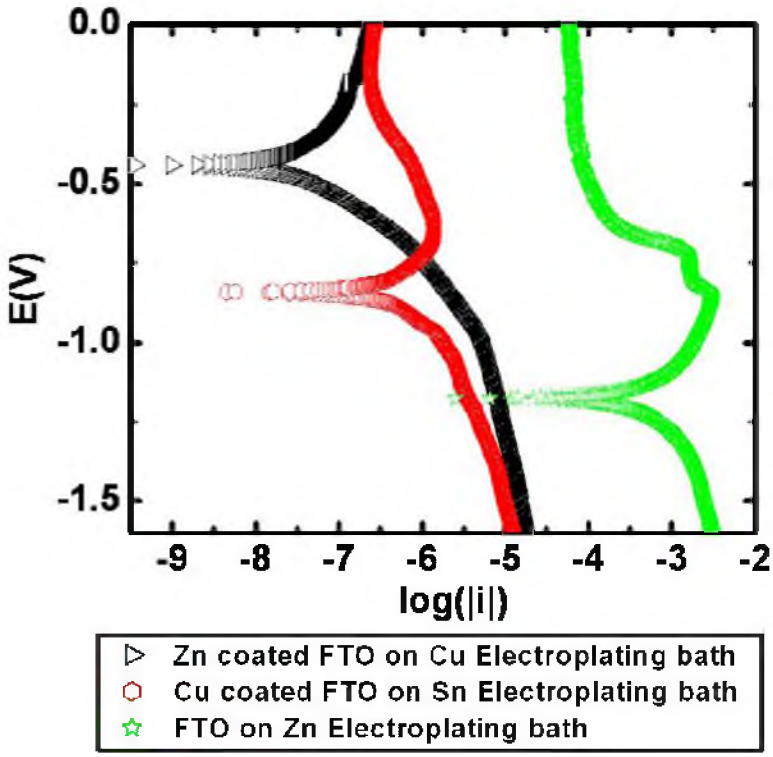

Figure 3.1: Potential vs. log(|i|) relationship for different electrochemical bath. The lowest equilibrium potential was obtained for the zinc electroplating solution ~ 1.2 V.

approximately -1.2 V. The equilibrium potential for Zn coated SnO_2/F in copper plating solution was -0.48 V. The equilibrium potential for Cu/Zn coated FTO in tin plating solution was ~ -0.87 V. The associated plots are shown in Figure 3.1. The depositions were carried out at -1.6 V for all the elements. All electrochemical tests and electrodepositions were performed using EG&G 273 and Gamry PCI4/750 Potentiostats. A Zn : Cu : Sn ratio of 1 : 2 : 1 was accurately controlled by varying the deposition time of each metal layer, where Zn, Cu, and Sn had average electrodeposition rate of ~ 4.5 mA/cm^2, 3 mA/cm^2, and 10 mA/cm^2, respectively. From initial deposition attempts it was found that high zinc and low copper content in the electrodeposited film gives good quality uniformity; however, excess zinc results in poor quality film with less adhesion. Zinc and tin content in electrodeposited film were kept almost equal for good quality film, which is desirable for good quality film as discussed in earlier reports [5]. Hence time of electrodeposition of different layers was precisely controlled to optimized film quality and optical property.

3.2.2 Sulfurization

After electrodeposition, films were soaked in de-ionized water and dried with Nitrogen. Cleaned films were sulfurized by annealing in a sulfur environment. Elemental sulfur (99.99%) was heated in a tube furnace and films were annealed at 550° C for 2hours. Prior to sulfurization the tube was purged with argon for 30 min to displace air. Sulfur was placed in a quartz boat and was held at a temperature of 150° C as the sulfur source. Sulfurized films were dipped in KCN (10% by weight solution in water) solution

followed by dipping in 50% aqueous solution of isopropyl alcohol to remove residual sulfide phases [8].

3.2.3 Film characterization

Thin films were characterized by x-ray diffraction (XRD), scanning electron microscopy (SEM), Inductively Coupled Plasma – optical emission spectroscopy (ICP-OES), Raman spectroscopy, atomic force microscopy (AFM) and transmission/absorption spectroscopy. XRD scans were run using a Philips X'Pert XRD diffractometer with Cu Kα radiation over the 2θ range 20–80°. Step sizes of 0.005° and a receiving slit size of 1/8° were used in order to achieve high resolution. Cross sectional SEM was performed using a Hitachi S3000-N scanning electron microscope. ICP-OES was done by Spectro Geneses optical spectrometer. Raman spectroscopy was carried out using a R 3000 QE portable Raman spectrometer (made by Raman Systems). A 785 nm laser with a power of ~ 140mW was used for excitation. The Raman spectrometer provides wavelength stability (less than $1cm^{-1}$ drift for over a 12 hour period). Optical transmittance measurements were performed using a DU 730 UV/Visible scanning spectrophotometer in wavelength scanning mode. An atomic force microscope equipped with Nanoscope V controller (make: Veeco Instruments) was used to analyze surface topography of the films. Measurements were carried out using Si_3N_4 (Silicon Nitride) cantilever in contact mode.

3.3. Results and discussion

3.3.1 Morphological characterization

The morphology of each electrodeposited metal layer is crucial to producing smooth dense CZTS films. Figure 3.2 (a-c) shows SEM micrographs of zinc (a), copper (b) and tin (c) film surfaces after each deposition. The initial zinc film has a uniform surface with few voids and a grain size between 200-300 nm. The subsequent copper layer is quite dense but has a noticeably different grain structure. The copper film has smaller and more regularly shaped grains in the range of 100-200 nm with better grain fusion than in the zinc film. (Figure 3.2(b)). The final tin on copper layer (Figure 3.2 (c)) has the largest grain size (~ 1 μm).

Surface morphology and thickness of sulfurized films characterized using SEM are shown in Figure 3.3. Figure 3.3(a) shows SEM micrographs of a characteristic film surface. From the lower magnification image two distinct gain structures, spherical and fiber are observed, which have average grain sizes measured to be 1.2 μm for spherical grains and 1.4 long by 0.2 μm wide for fiber grains. However, at higher magnification, shown in the inset, the film appears to be quite dense with few voids and a highly interconnected network of grains. Producing such dense film with good interconnection between grains is required for high performance photovoltaic devices [10]. Figure 3.3(b) shows a SEM micrograph of the cross section of a CZTS film on FTO coated glass. The micrograph shows a dense 1.7 μm thick CZTS film. An abrupt interface between the FTO coated glass substrate and the CZTS film can clearly be seen indicating good adhesion between film and substrate. A 2D AFM micrograph taken over a 25 μm^2 area of an annealed CZTS film is shown in Figure 3.3(c). The surface is quite smooth for most

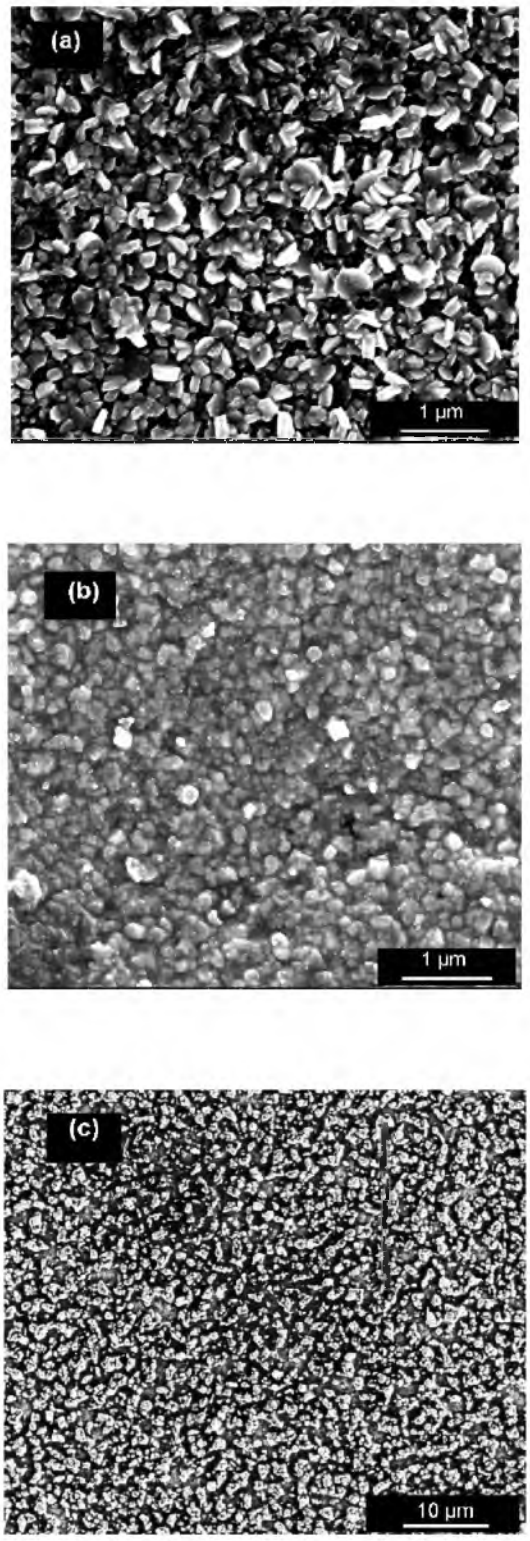

Figure 3.2: (a) SEM image of Zn electrodeposited on FTO coated glass, (b) SEM image of Cu electrodeposited on Zn, (c) SEM image of Sn electrodeposited on Cu film.

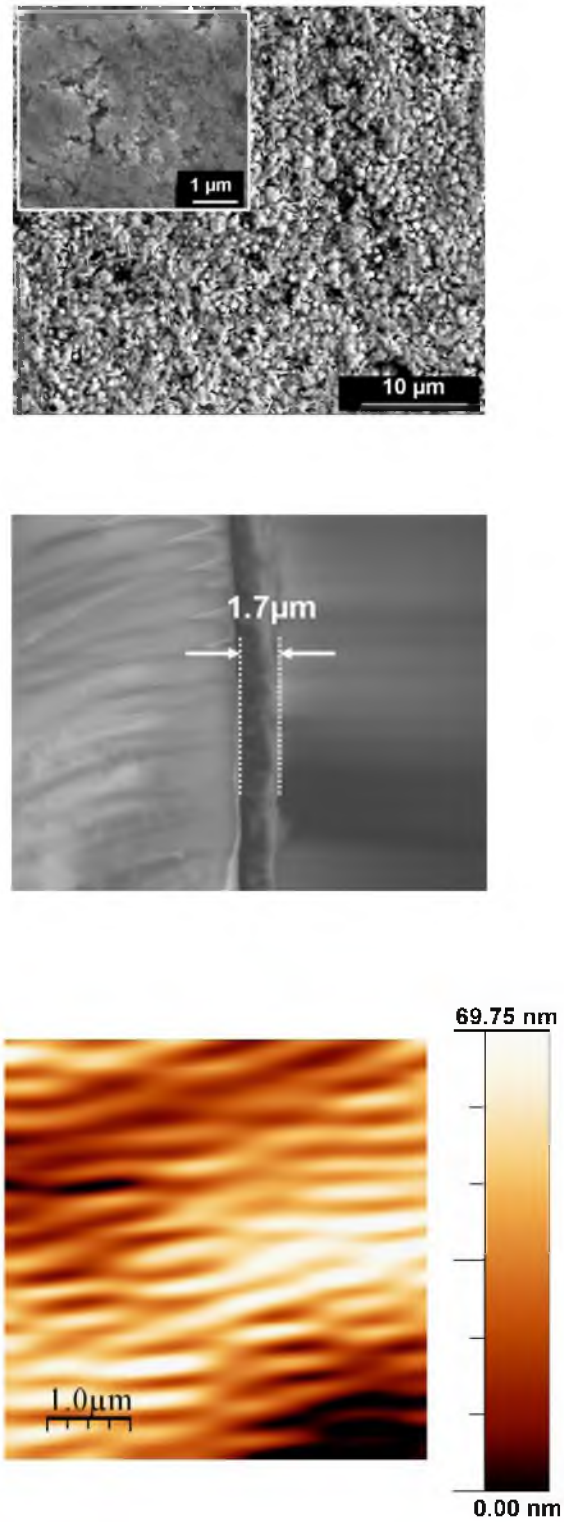

Figure 3.3: (a) SEM image of surface, (b) cross section, and (c) AFM micrograph of CZTS thin film. A dense film with few voids and interconnected grains can be seen.

regions of the film, and the vertical height between the highest and lowest features is in the range of 70-75 nm. This is quite smooth for CZTS films deposited by the electrochemical method. The above AFM 2D micrograph quality is comparable to the work of Kamoun *et al.* where the vertical height between lowest and highest features of "spray-pyrolysis deposited" CZTS thin film was ~ 80 nm [11]. However, the average roughness of our electrodeposited films is ~30 nm over this area, which is lower than that reported by Kamoun *et al.* for films synthesized by spray pyrolysis [11].

3.3.2 Chemical analysis

The chemical composition of as deposited film was analyzed by ICP-OES using smart analyzer vision software. The results shows Zn : Cu : Sn ratio of 1 : 2 : 1 , which is desired for stoichiometric CZTS formation.

3.3.3 Structural characterization

Figure 3.4 shows a characteristic XRD pattern for a postsulfurized film. This pattern matches very well with the kesterite structure of CZTS (JCPDS card 26-0575). Peaks corresponding to (112), (103), (200), (105), (220), (312), (224), (314), (008) and (332) planes were detected indicating the polycrystalline nature of the film. Few additional peaks corresponding to any secondary phase were observed, suggesting the high phase purity of the material. However, due to the complex nature of the quaternary compound CZTS, many secondary phases with similar crystal diffraction patterns may coexist, making phase identification with XRD complex. Therefore, to further confirm the phase purity of these films, Raman spectroscopy was carried out. The inset of Figure 3.4 shows

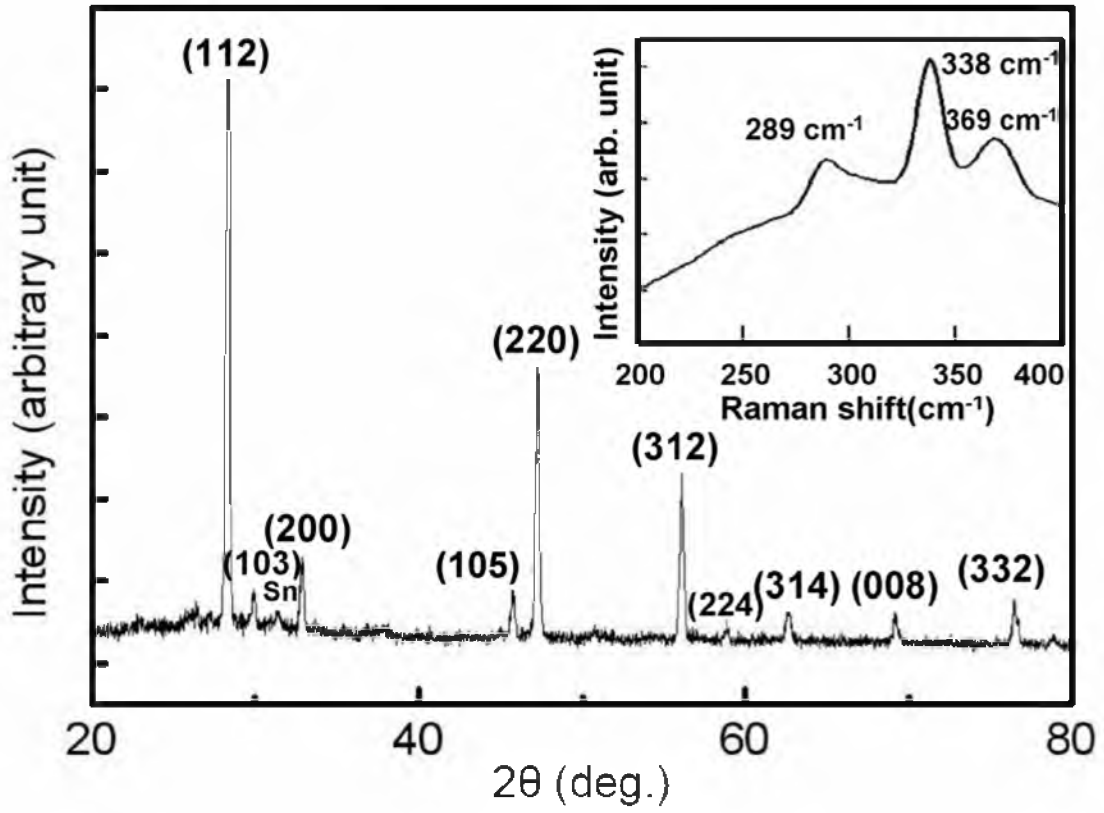

Figure 3.4: XRD pattern of CZTS films, Raman spectra is shown in inset. Both characterization methods confirm presence of Kesterite phase CZTS.

the Raman spectrum of a film over the range 200 to 400 cm^{-1}. In the Raman spectrum three peaks located at 289, 338 and 369 cm^{-1} can clearly be seen with the high intensity peak located at 338 cm^{-1}. The peak positions and relative intensities are in good agreement with the previously reported Raman spectra of CZTS absorber material [12].

3.3.4 Optical and electrical characterization

The optical properties of annealed films were analyzed using UV-VIS optical transmission spectroscopy. Figure 3.5 shows the transmittance of a CZTS film as a

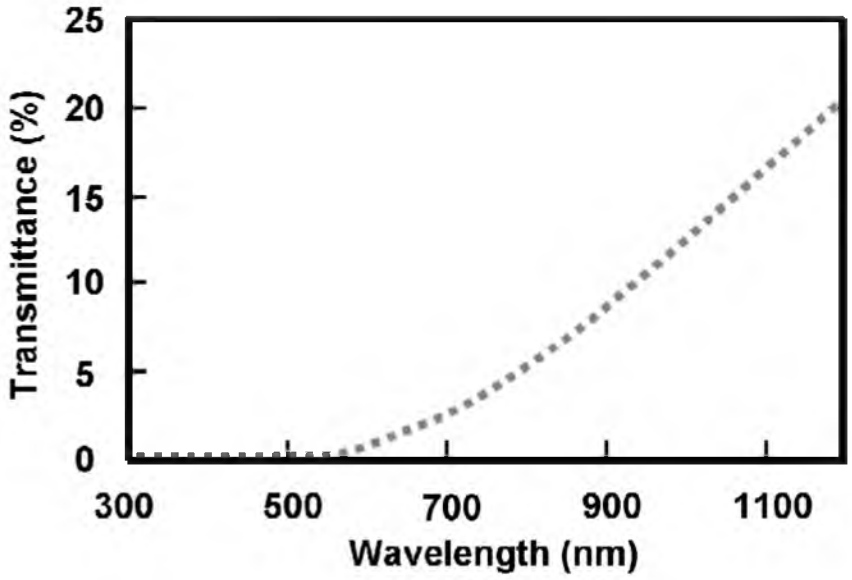

Figure 3.5: Transmittance vs. wavelength of CZTS films.

function of wavelength. Using the transmittance data from the absorption spectra the energy gap can be determined:

$$\alpha=A(h\nu-E_g)^{1/2} \tag{3-1}$$

where α is the absorption coefficient, A is a constant, E_g is the energy gap and *hν* is the incident photon energy [13]. Figure 3.6 shows α^2 as a function of incident photon energy for CZTS films deposited on FTO coated glass. By extrapolating the α^2 vs. photon energy curve to zero, the band gap was evaluated to be ~1.5 eV, which is consistent with reported literature values [1-16]. To determine the majority carrier type and insure the intrinsic p-type nature of our CZTS films a conventional hot probe test was implemented.

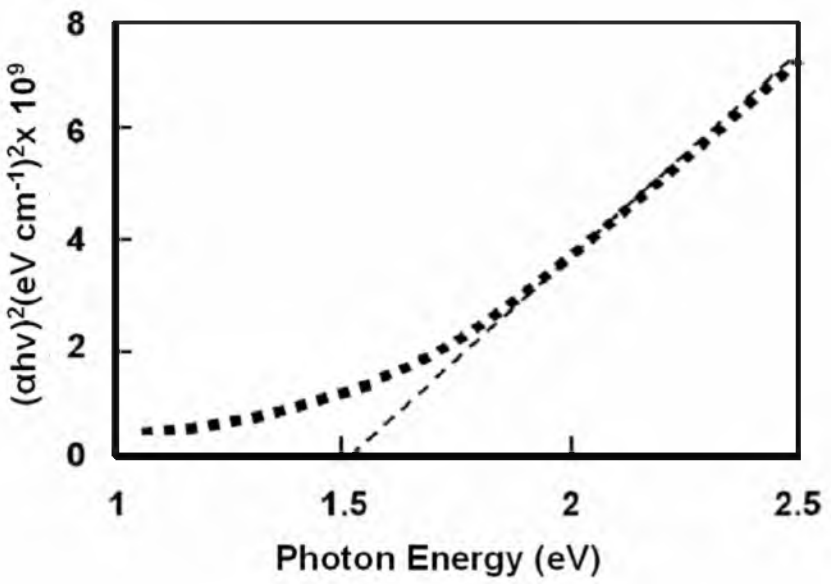

Figure 3.6: (α^2) vs. photon energy hv for CZTS films.

The films were connected to a volt meter and then the contact point between positive lead and the films surface was heated. This produced a temperature difference of ~10 K across the film. The formed temperature gradient then causes diffusion of the majority charge carriers from the hot to the cold end of the film, thus producing a voltage. All films showed a negative voltage at the hot end of sample, indicating the p-type nature of the electrodeposited CZTS films.

3.4. Conclusions

In summary, we have demonstrated the use of a low cost, highly scalable electrochemical method for production of CZTS thin films on FTO coated glass surface. CZTS films were synthesized by sequential electrodeposition of Zn/Cu/Sn metal films followed by sulfurization and annealing at 550^{o} C. Films were found to be single phase kesterite CZTS with holes as dominant charge carriers. AFM images of the films showed

smooth surface morphology with an average surface roughness less than 30 nm. The band gap of the films was evaluated to be 1.5 eV. The synthesis methodology discussed in this report can work as possible alternative of CZTS on Mo back contact, which can be extended to other CZTS synthesis technique.

3.5. References

[1] X. Zhang, X. Shi, W. Ye, C. Ma, C. Wang, Appl. Phys. A. 94 (2009)381.

[2] H. Araki, Y. Kubo, A. Mikaduki, K. Jimbo, W. S. Maw, H. Katagiri, M. Yamazaki, K.Oishi, A. Takeuchi, Sol. Energ. Mat. Sol. Cells. 93 (2009) 996.

[3] H. Araki, A. Mikaduki, Y. Kubo, T. Sato, K. Jimbo, W. S. Maw, H. Katagiri, M. Yamazaki, K.Oishi, A. Takeuchi, Thin Solid Films 517 (2008) 1457.

[4] H. Araki, Y. Kubo, K. Jimbo, W. S. Maw, H. Katagiri, M. Yamazaki, K.Oishi, A. Takeuchi, Phys. Status Solidi C 6 (2009)1266.

[5] J.J. Scragg, P.J. Dale, L.M. Peter, Thin Solid Films 517 (2009) 2481.

[6] C.P. Chan, H. Lam, K. Y. Wong, C. Surya, Mater. Res. Soc. Symp. Proc. 1123 (2009)06.

[7] T. Nakada, Thin Solid Films 480-481 (2005) 419.

[8] P.A. Fernandese, P.M.P Salomé, A.F.da Cunha, Semicond. Sci. Technol. 24(2009) 105013.

[9] W. S. Miu, J. Ross, F.Lau, B.L. Fong, Trans. Soc. Met. Finish. 75 (1997)137.

[10] T. Tanaka, T. Nagatomo, D. Kawasaki, M. Nishio, Q. Guo, A. Wakahara, A. Yoshida, H. Ogawa, J. Phys. Chem. Solids 66 (2005)1978.

[11] N. Kamoun, H. Bouzouita, B. Rezig, Thin Solid Films 515 (2007) 5949.

[12] P.A. Fernandese, P.M.P Salomé, A.F.da Cunha, Thin Solid Films 517 (2009) 2519.

[13] M. Snure, A. Tiwari, Appl. Phys. Lett. 91 (2007) 092123.

[14] H. Katagiri, K. Jimbo, W. S. Maw, K.Oishi, M. Yamazaki, H. Araki, A. Takeuchi, Thin Solid Films 517 (2009) 2455.

[15] Q. Guo, H. W. Hillhouse, R. Agrawal, J. Am. Chem. Soc. 131 (2009) 11673.

[16] C. Steinhagen, M. G. Panthani, V. Akhavan, B. Goodfellow, B. Koo, B. A. Korgel, J. Am. Chem. Soc. 131 (2009) 12555.

CHAPTER 4

A FACTORIAL DESIGN OF EXPERIMENTS APPROACH TO SYNTHESIZE CZTS ABSORBER MATERIAL FROM AQUEOUS MEDIA

4.1 Introduction

It seems very obvious to get the desired stoichiometry of electrodeposited component by sequential deposition. In this case, a different bath for each component is used to electroplate the metal layer. The amount of electrodeposited component is related to the total electric charge flow in each deposition. For CZTS synthesis using the sequential deposition approach, the whole process involves two additional steps and is time consuming. The single bath electrodeposition technique facilitates to reduce the additional electrodeposition step, but formulation of bath composition to get a molar ratio 2:1:1 of Cu/Zn/Sn, respectively is difficult. This chapter is focused on single stage Cu-Zn-Sn co-electrodeposition from aqueous solution based method and annealing, using factorial design of experiments approach. Factorial experiments allow study of the effects of each factor on the response variable, as well as effects of interactions between individual factors on the response variable [1]. A model has been developed to show and predict domain for best possible factors for CZTS based device fabrication.

Some research group recently reported single bath recipe of CZTS, though methodology of formulation is yet not explained [2]. Design of experiment approach explores relationship between several experiment input and response variable. Investigation domain will be shortening further.

4.2 Theory

In order to explore the effect of individual components like concentration of Zn^{2+} ion, concentration of Cu^{2+} ion, concentration of Sn^{2+} ion and concentration of complexing agent a factorial design of experiments was established. In most of the factorial experiments each factor has only two levels (high and low). Now consider an experiment using 4 factors A, B, C and D with two levels (high and low). It will result in 16 treatment combinations. A set of tests that follow factorial design approach with variables A, B, C and D tested at high (+) and low (-) levels is presented in Table. The value of main effect parameter and interaction effect parameter is indicative of how strong individual factor affects the response variable. The null outcome indicates the neutrality of effect parameter.

The relative effects of parameters are shown below:

$$A: (-Y_1+Y_2-Y_3+Y_4-Y_5+Y_6-Y_7+Y_8-Y_9+Y_{10}-Y_{11}+Y_{12}-Y_{13}+Y_{14}-Y_{15}+Y_{16})/16 \quad (4\text{-}1)$$

$$B: (-Y_1-Y_2+Y_3+Y_4-Y_5-Y_6+Y_7+Y_8-Y_9-Y_{10}+Y_{11}+Y_{12}-Y_{13}-Y_{14}+Y_{15}+Y_{16})/16 \quad (4\text{-}2)$$

$$C: (-Y_1-Y_2-Y_3-Y_4+Y_5+Y_6+Y_7+Y_8-Y_9-Y_{10}-Y_{11}-Y_{12}+Y_{13}+Y_{14}+Y_{15}+Y_{16})/16 \quad (4\text{-}3)$$

$$D: (-Y_1-Y_2-Y_3-Y_4-Y_5-Y_6-Y_7-Y_8+Y_9+Y_{10}+Y_{11}+Y_{12}+Y_{13}+Y_{14}+Y_{15}+Y_{16})/16 \quad (4\text{-}4)$$

A positive relative effect indicates enhancement of response variable due to increment of "particular factors". Experimental matrices are designed by choosing Cu^{2+},

Table 4.1: A four factors two level design of matrix

Run	A	B	C	D	Observation
1	-	-	-	-	Y_1
2	+	-	-	-	Y_2
3	-	+	-	-	Y_3
4	+	+	-	-	Y_4
5	-	-	+	-	Y_5
6	+	-	+	-	Y_6
7	-	+	+	-	Y_7
8	+	+	+	-	Y_8
9	-	-	-	+	Y_9
10	+	-	-	+	Y_{10}
11	-	+	-	+	Y_{11}
12	+	+	-	+	Y_{12}
13	-	-	+	+	Y_{13}
14	+	-	+	+	Y_{14}
15	-	+	+	+	Y_{15}
16	+	+	+	+	Y_{16}

Zn^{2+}, Sn^{2+} and amount of Potassium pyrophosphate as factors while CZTS phase %, adhesion, band gap and career concentration as response variable. CZTS phase was detected by XRD and Raman spectroscopy. An index is assigned based on peak intensity which corresponds to CZTS. Highest peak intensity was assigned value “100” while when there is no peak “0” value is assigned. This index was used as response variable. Similarly good quality film with highest adhesion was assigned value “100” while poor quality film with less adhesion as “0”. The carrier concentration was determined using Mott-schottkey analysis for best case.

4.3 Experiments

Electrowinning cells enclosed by water jacket were used to perform the electrodeposition on conducting substrate at the controlled temperature of 58°C. All electrochemical tests were performed using EG&G 273 and Gamry PCI4/750 Potentiostats. After electrodeposition, films were rinsed in deionized (DI) water and dried with nitrogen gas. Cleaned films were sulfurized by annealing in a sulfur environment. Annealing was performed in an argon environment with heated elemental sulfur (99.99%) in a tube furnace. Film characterization and analysis were conducted using XRD(by Philips X'Pert diffractometer with Cu Kα radiation over the 2θ range 20–80°), Raman spectroscopy (Raman systems), UV-Vis spectroscopy (Ocean optics spectrometer), electrochemical impedance spectroscopy and scanning electron microscopy. The co-electrodeposition was carried out using copper sulfate pentahydrate, tin chloride, zinc sulfate heptahydrate, and potassium pyrophosphate. The experiment matrix is shown in Table 4.2.

4.4 Discussion

The 3D profiling of response vs. different factors is represented in Figure 4.1. All statistical analysis were done using Statistica and Minitab software. From figure it can be concluded that CZTS formation best occurs for high zinc and low copper regime. Relative high tin regime is also not favorable as revealed by response variable. Relative high amount of pyrophosphate salt is also found favorable for CZTS synthesis. CZTS surface morphology is also monitored in all cases. It is found that high zinc content weakens adhesion while moderate copper amount improves adhesion.

Table 4.2: Four factors experiment matrix for CZTS synthesis by co-deposition

Serial Number	Cu^{2+} (M)	Zn^{2+} (M)	Sn^{2+} (M)	Sodium pyrophosphate(M)
1	0.0840	0.0140	0.0170	0.3000
2	0.0160	0.0140	0.0340	0.1500
3	0.0160	0.0700	0.0170	0.3000
4	0.0160	0.0700	0.0340	0.3000
5	0.0840	0.0700	0.0170	0.3000
6	0.0160	0.0140	0.0170	0.3000
7	0.0160	0.0700	0.0340	0.1500
8	0.0840	0.0700	0.0340	0.1500
9	0.0160	0.0140	0.0170	0.1500
10	0.0160	0.0700	0.0170	0.1500
11	0.0840	0.0700	0.0340	0.3000
12	0.0840	0.0700	0.0170	0.1500
13	0.0840	0.0140	0.0340	0.3000
14	0.0840	0.0140	0.0340	0.1500
15	0.0840	0.0140	0.0170	0.1500
16	0.0160	0.0140	0.0340	0.3000

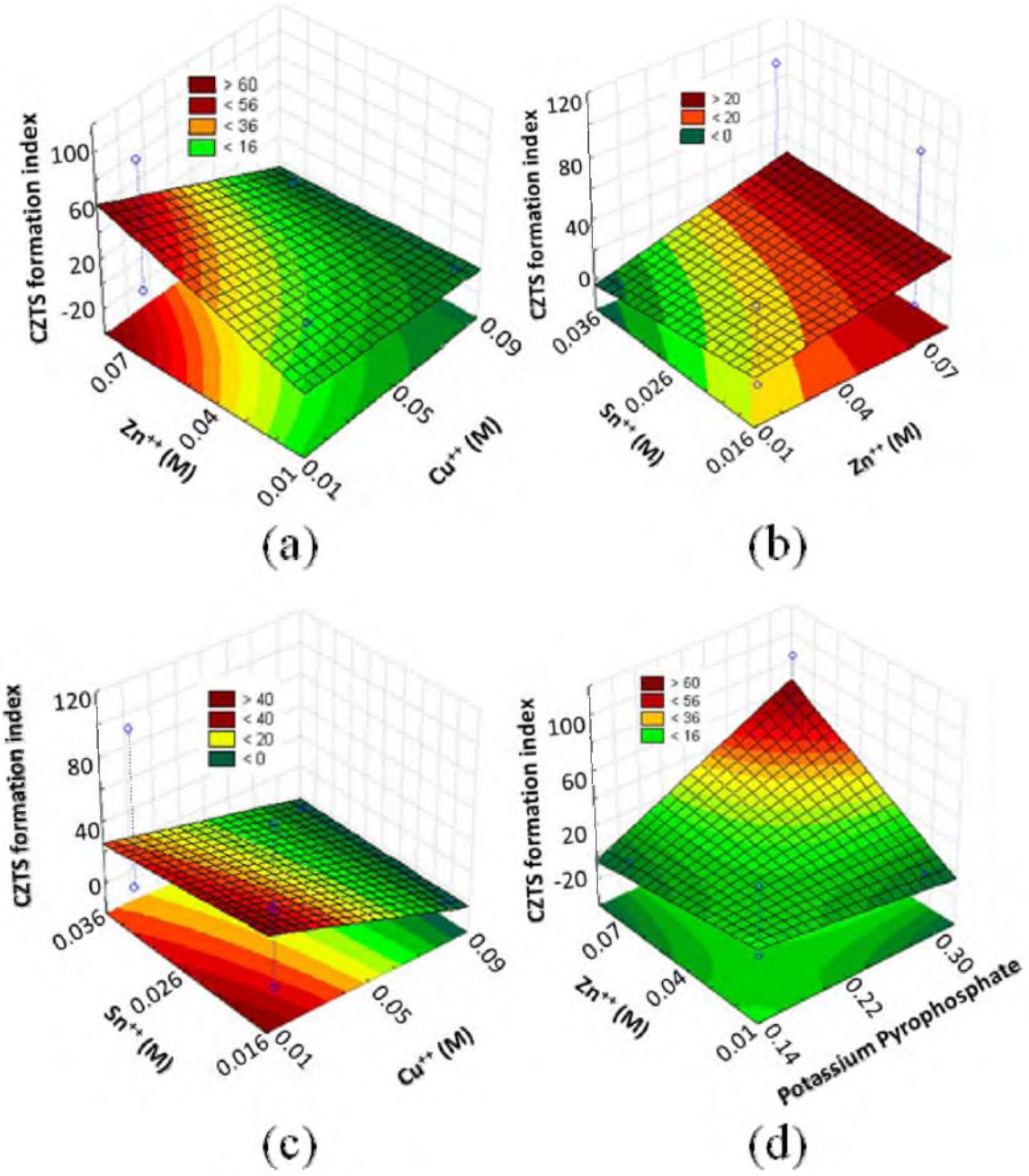

Figure 4.1: 3D profiling of CZTS formation index is plotted for different concentration of Cu^{2+}, Zn^{2+}, Sn^{2+} and Potassium pyrophosphate.

A conclusion can be made from Figure 4.1 that high zinc-low tin-moderate copper and high amount of pyrophosphate salt is best favorable case for CZTZ synthesis. Further factors-response analysis was carried out in the neighborhood of the best range obtained for CZTS formation. The band gap was determined using transmittance data of film by UV-VIS optical transmission spectroscopy [3]:

$$\alpha=A(h\nu-E_g)^{1/2} \tag{4-5}$$

where α is the absorption coefficient, A is a constant, E_g is the energy gap and $h\nu$ is the incident photon energy. The band gap vs. concentration 3D profiling is represented in Figure 4.2. It can be seen that band gap increases when relative concentration of zinc is high, on the other hand excess tin amount causes formation CTS (copper tin sulfide) which in turn reduces band gap ~ 1.3 eV.

The acceptor concentration of CZTS absorber layer was determined by measuring the apparent capacitance (unit area) as a function of potential and is based on the Mott-Schottky relationship [4]:

$$\frac{1}{C_{sc}^2}=\frac{2}{e\varepsilon\varepsilon_0 N}\left[E-E_{FB}-\frac{K_B T}{e}\right] \tag{4-6}$$

where ε is dielectric constant (10 for CZTS), C_{sc} is capacitance of the space charge region, of the semiconductor, εo is permittivity of free space, N is the acceptor concentration, E is the applied potential (biased voltage), K_B is Boltzmann's constant, e is the electronic charge and E_{fb} is flat band potential of film[4]. The value of the carrier concentration comes out to be ~ $10^{18}/cm^3$.

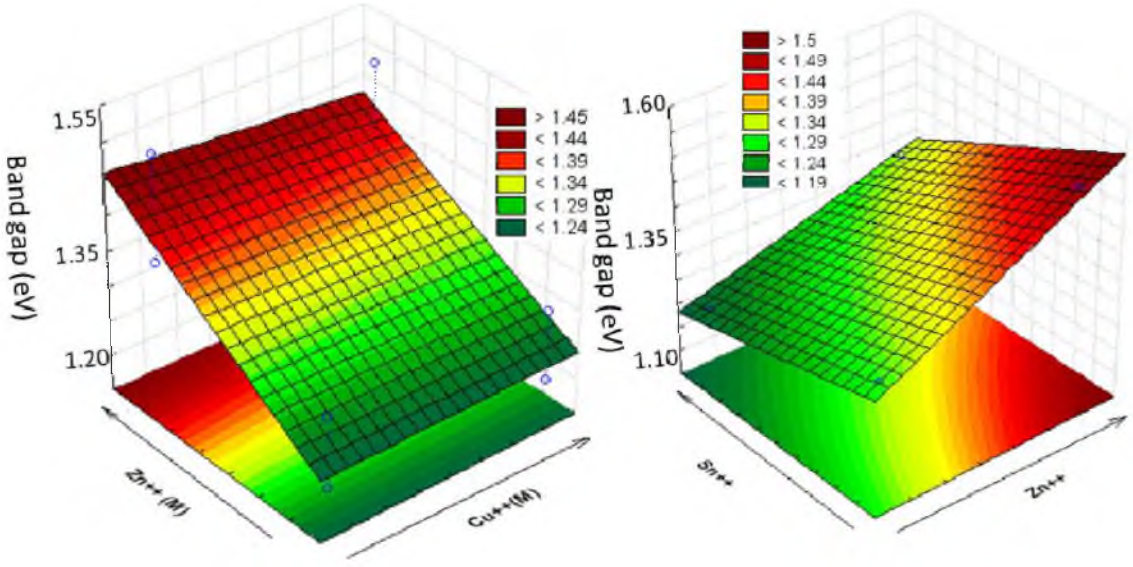

Figure 4.2: 3D profiling of band gap is plotted for different relative concentration of Cu^{2+}, Zn^{2+}, Sn^{2+} and 0.30 M/L Potassium pyrophosphate.

4.5 Conclusions

The results of design of experiment indicate that best domain for CZTS synthesis from single bath technique is: moderate amount of copper, high zinc and relative low amount of tin in the electroplating bath. However little modification is required to improve surface morphology and adhesion, this is due to reduced adhesion in presence of excess zinc concentration. Moderate concentration of copper also helps for better film quality. The band gap of film reduces towards low zinc as well as high tin side.

4.6 References

[1] P. K.Sarswat, M.L.Free, Copper 2010, Electrowinning and electrorefining 4(2010) 1649.

[2] S. M. Pawar, B.S. Pawar, A.V. Moholkar, D. S. Choi, J. H. Yun, J.H. Moon, S.S. Kolekar, J. H. Kim, Electrochimica Acta 55 (2010) 4057

[3] M. Snure, A. Tiwari, Appl. Phys. Lett. 91(2007) 092123.

[4]F.Cardon, W. P. Gomes, J.Phys. D: Appl. Phys.,11(1978).

CHAPTER 5

A DEMONSTRATION OF SOL-GEL SYNTHESIZED BIFACIAL CZTS-PHOTOELECTROCHEMICAL CELL

5.1 Introduction

Bifacial solar cells are potential candidates to lower the costs of solar electricity relative to monofacial solar cell [1]. These cells can utilize front as well rear illumination of light for greater conversion of electrical power [2, 3]. The operation of bifacial solar cells at relatively lower temperatures and high power to weight ratios are other added advantages [1-3]. To meet the challenge of optimum light energy harvesting using inexpensive, widely available and nontoxic materials, CZTS can be categorized as one of the best potential photovoltaic absorbers and less expensive solar cell than silicon [4-7]. The requirement of thick ~ 200 μm silicon absorber layers, due to the low absorption coefficient of silicon, combined with the typical high temperature processing makes bifacial Si solar cell technology expensive [8].

Copper zinc tin sulfide (CZTS), a wide band gap p-type quaternary chalcogenide, has drawn significant interest due to utilization of inexpensive, efficient, and environment friendly materials for thin film solar cells [4-22]. While there has been

published literature regarding the CZTS preparation as mentioned above, most of the associated experiments utilized opaque substrates. Although conventional CZTS based monofacial devices are fabricated using molybdenum, which has its own benefits, use of a transparent conducting substrate offers potential for development of high efficiency semitransparent solar cells. In the case of a transparent back contact, CZTS absorber layer will be more useful for places where availability of albedo radiation is high. In addition, these devices will be more prone to electron – hole pair generation during simultaneous both side illumination. A possibility of semitransparent copper indium gallium diselenide (CIGS) based photovoltaic cells for top tandem and bifacial devices using transparent conducting substrates has already been explored [23]. It is reported that various transparent conducting oxide materials are used for back contacts, including FTO (which is an n-type TCO), for bifacial PV cell. In view of these aspects a primary examination of spin coated – diffusion annealed CZTS thin films on transparent SnO_2/F coated glass substrates for potential bifacial solar cell technology were conducted. A photoelectrochemical cell using CZTS (on TCO) and Eu^{3+}/Eu^{2+} is made to observe photocurrent response for front, rear and simultaneous dual illumination. This nondestructive way of photovoltaic properties assessment will provide additional information, which will be used for solid state bifacial photovoltaic device development using CZTS as the absorber. This idea can be extended to the use of CZTS for solar cell with double sided junctions, which can decrease resistive loss as well as yield extra output power.

5.2 Experimental details

Sol-gel coating was performed using a spin coater with variable speed at room temperature. Transparent conducting oxide (FTO) coated glass substrates (area utilized for spin coating = 1.5-2.0 cm^2) were used as a substrate base for CZTS growth. The stoichiometry of sol solution was optimized by variation of individual metallic species concentrations. The spin coating was carried out using a sol solution of 0.205 M copper (II) chloride, 0.102 M zinc acetate dihydrate and 0.102 M tin chloride dissolved in 3 ml of monoethanolamine and 7 ml of butanol. The sol solution was dropped on a FTO substrate and rotated for 30 sec at 2500 rpm. The spin coated film was dried in air at ~ 250 ^{o} C for 5 to 10 min. The spin coating and drying process was repeated multiple times to obtain the desired thickness (~ 1 micron) of film. The sulfurization of spin coated – air dried films was carried out by annealing in a heated sulfur environment at a substrate temperature range 450-475^{o}C for two hours with continuous argon flow. The resisitivity of FTO back contact was compared before and after sulfurization. The increase in resitivity was ~ 15%. This increment is not as high which encountered during sulfurization at 570^{o} C, which will result reduced device performance [6].

5.3 Results and discussion

Thin sulfurized films were examined by x-ray diffraction (XRD), scanning electron microscopy (SEM), EDS, Inductively coupled plasma mass spectroscopy, UV-Vis spectroscopy and Raman spectroscopy. XRD measurements were carried out over the 2θ range 20–80° using a Philips X'Pert XRD diffractometer equipped with Cu source (Kα radiation). The surface SEM imaging was performed using an FEI NanoNova scanning

electron microscope. Raman spectra were recorded using R 3000 QE portable Raman spectrometer (made by Raman Systems). Incident power measurements were carried out using Nova II ophir power meter. Photocurrent response was measured for front as well as back illuminated sample and in a dark environment. All photoelectrochemical measurements of CZTS thin films grown on FTO substrates were conducted using a 0.07 M $Eu(NO_3)_3.6H_2O$ aqueous solution. The europium nitrate acts as an electron scavenging redox electrolyte [19]. The photocurrent responses of the CZTS absorber layer were measured by a potentiostatically controlled 3-electrode system (platinum counter electrode, SCE reference electrode, and a CZTS on FTO film as the working electrode). Transient photocurrents were generated using alternating illumination from a high intensity white light optic illuminator.

A characteristic θ-2θ XRD pattern of a CZTS thin film is shown in Figure 5.1. This XRD pattern matches very well with the kesterite structure of CZTS (JCPDS card 26-0575). Figure 5.2 shows the Raman spectra of the film over the range 200 to 400 cm^{-1}. In the Raman spectrum an obvious major peak located at 338 cm^{-1}, and two minor peaks at 369 cm^{-1} and 287 cm^{-1} can clearly be seen. These strong peaks were observed for the sol prepared by using nearly stoichiometric amounts of copper salt, zinc salt and tin salt as required for a 2:1:1 ratio in the film. These spectral data are in good agreement with the reported Raman spectra of CZTS [4, 18]. However, modification of the sol stoichiometry results in various secondary phases. Lower than stoichiometric copper in the sol results in formation of various unwanted secondary phases such as tin sulfide. A peak corresponding to 313 cm^{-1} can clearly be seen in the Raman spectra for copper depleted films, which corresponds to tin sulfide [18]. Primary investigations of elemental

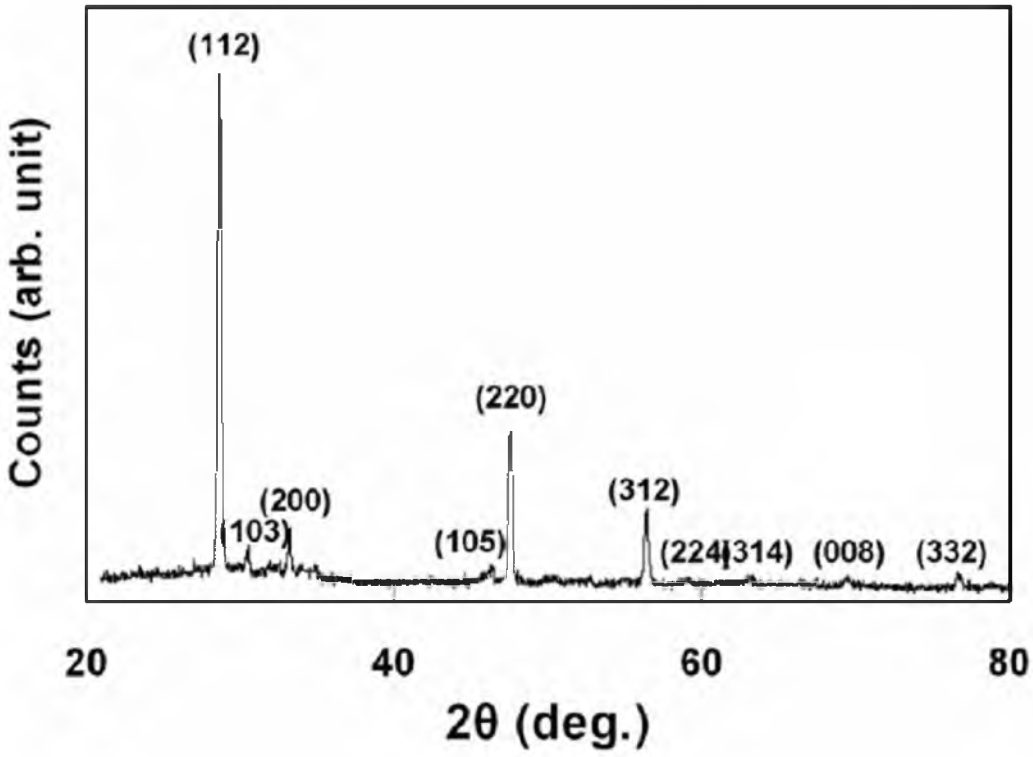

Figure 5.1: XRD pattern of sol-gel synthesized CZTS film.

characterization by EDS (EDAX^{TM}) reveal elemental ratio is close to ratio that required for stoichiometric CZTS formation. Inductively coupled plasma (ICP) spectroscopy of thin film was done by Spectro geneses optical spectrometer. The chemical composition of spin coated-sulfurized film was analyzed smart analyzer vision software. The results shows Zn : Cu : Sn ratio of 1 : 2 : 1 , which is desired for stoichiometric CZTS formation. Film morphology was analyzed using SEM. An SEM micrograph of a ~ 20x20 μm^2 area of an annealed CZTS film is shown in Figure 5.3. The surface is quite dense for most regions of the film with an average grain size of ~ 400 nm. A more magnified micrograph of a CZTS film on SnO_2/F coated glass is shown in the inset of Figure 5.3. Band gap measurements of CZTS thin films were done using transmittance data obtained

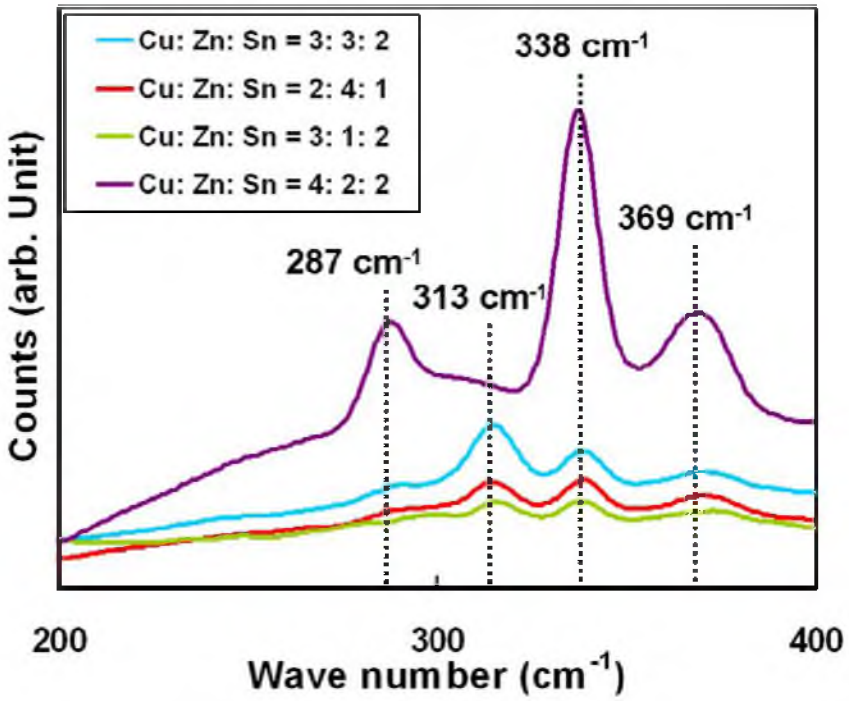

Figure 5.2: Raman spectra of stoichiometric CZTS film showing evidence of three distinct peaks, while copper depleted films show presence of tin sulfide.

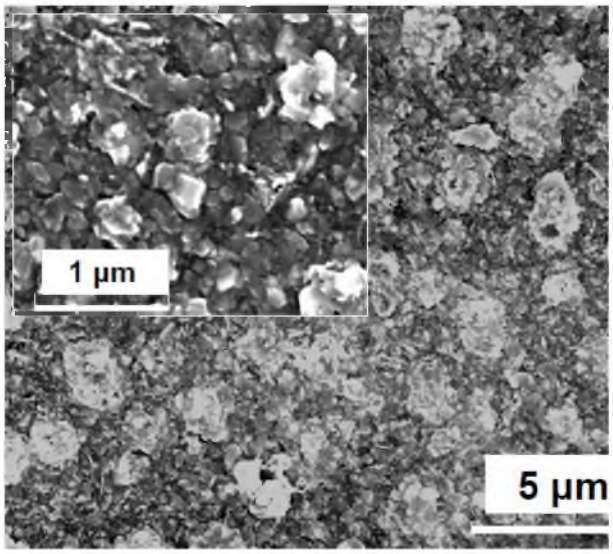

Figure 5.3: SEM image of surface of CZTS thin film.

from Ocean Optics spectrophotometer equipped with OOI Base 32 software. Using transmittance data from the absorption spectra the energy gap can be obtained [5]:

$$\alpha = A(h\nu - E_g)^{1/2} \qquad (5\text{-}1)$$

where α is the absorption coefficient, A is a constant, E_g is the energy gap and $h\nu$ is the incident photon energy. Figure 5.4 shows α^2 as a function of incident photon energy for CZTS films grown on FTO coated glass, the band gap obtained is ~ 1.47 eV, which is close to band gap of CZTS. Redox species whose redox potential lies in a range where no degradation of semiconductor occurs were selected for electrochemical characterization. A Eu^{3+}/ Eu^{2+} redox couple was chosen for photoelectrochemical characterization of annealed CZTS films [24]. Its redox potential vs. MSE (Mercury Sulfate Reference Electrode) is -1.08 V. An examination of energy band position for CZTS in electrolyte with Eu^{3+}/ Eu^{2+} redox species, based on information from sources reveals that the unoccupied level of the Eu^{3+}/ Eu^{2+} couple overlaps with the conduction band of CZTS [19,24]. Thus, easy transfer of electrons from the conduction band to the redox system

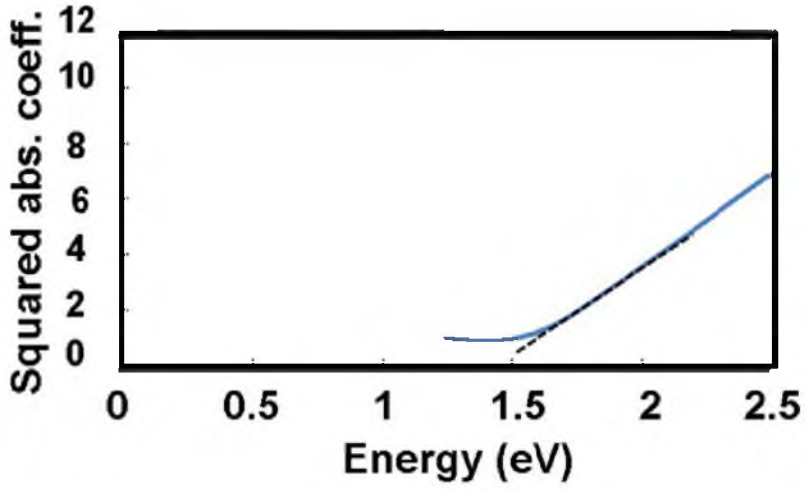

Figure 5.4: Squared absorption coefficient vs. Energy plot of CZTS thin film.

can be expected. When the CZTS surface is illuminated, created photoelectrons move towards the electrode/electrolyte interface and are transferred to reduce one of the redox species. The sudden change in current indicates a transfer of electrons from the electrode to the solution. Linear scan voltammograms were recorded (as shown in Figure 5.5-5.7) during flashing light illumination by the potentiostat using virtual front panel software. The cathodic photocurrent response validates p-type photoactivity of the annealed CZTS films (A conventional hot probe method was also utilized to identify the intrinsic p-type nature of our CZTS films) [19]. For front illumination (Figure 5.5), the photocurrent onset was found at ~ +0.05 V versus a saturated calomel electrode (SCE), and the photocurrent saturates at potentials more negative than -0.50 V. Similarly, for back illumination the photocurrent (Figure 5.6) saturates at a potential of ~ 0.45 V with respect to SCE. It can be seen that a change of ~ 0.050 mA was obtained at saturation for back illumination, which is two thirds of the front illumination photocurrent response (0.075 mA). The reduced back illumination photocurrent response was investigated by comparing incident power input. The incident power was ~ 0.22 mW/cm^2 for front illumination, while back illumination it was ~ 0.16 mW/cm^2. It can be seen that photocurrent responses are consistent with incident power. Using a similar configuration, in another set of experiments, the CZTS surface was simultaneously exposed to front and back illumination. The combined photocurrent response was more enhanced than front illumination as shown in Figure 5.7 by the dotted red line. These results convincingly indicate that front and back photoelectrochemical responses are comparable. The results also show increased photoelectrochemical response due to simultaneous dual illumination.

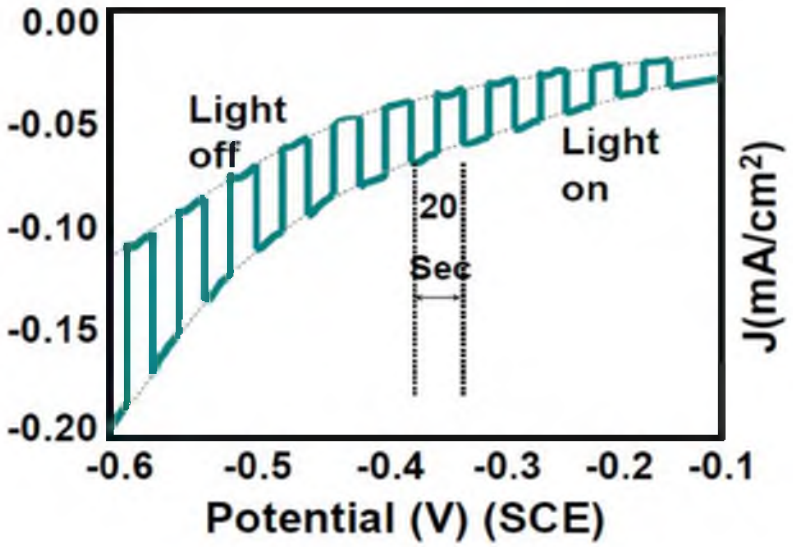

Figure 5.5 : Photoelectrochemical response of CZTS film for front illumination.

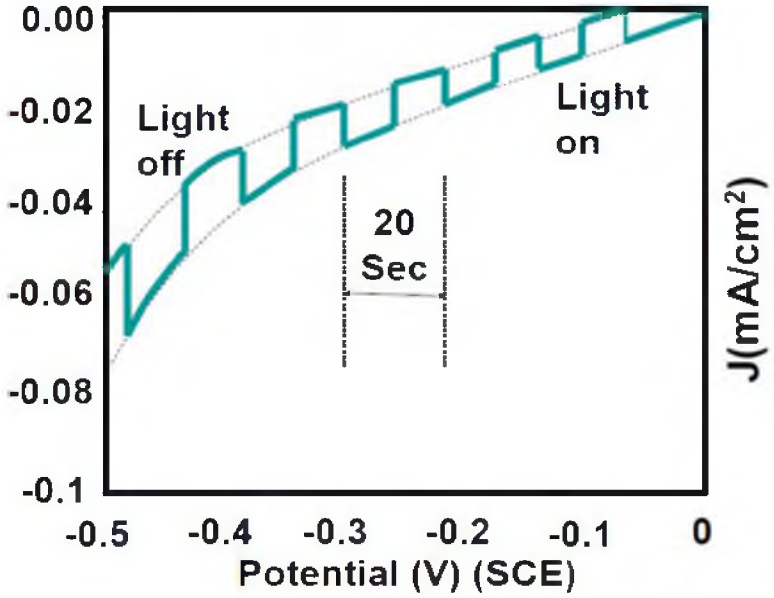

Figure 5.6: Photoelectrochemical response of CZTS film for back illumination.

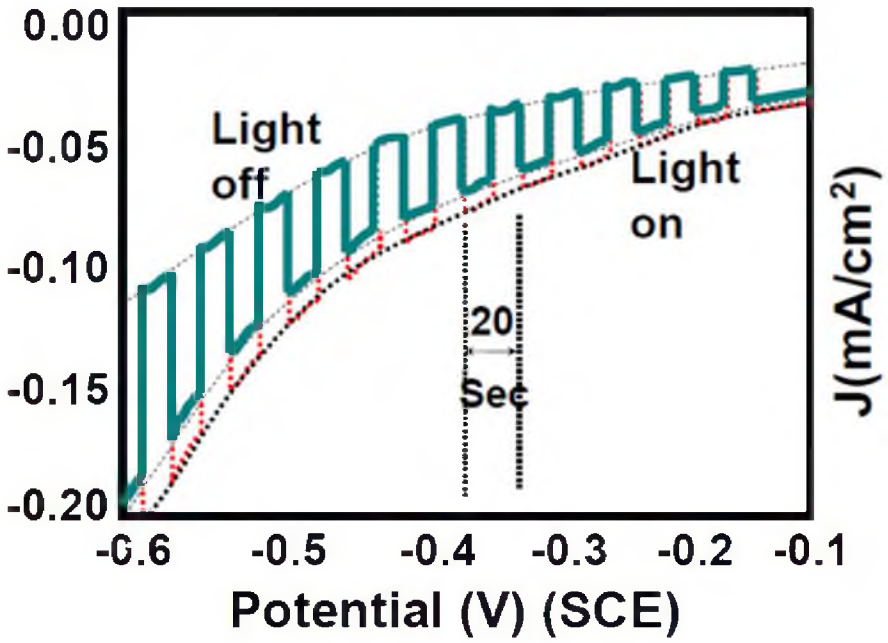

Figure 5.7: Photoelectrochemical response of CZTS film for dual illumination.

These observations suggest that a complete CZTS based solid state photovoltaic device, fabricated on TCO have sufficient potential for development as semitransparent or bifacial solar cell. However, care must be taken to reduce conductivity loss during sulfurization.

5.4 Conclusions

In summary, CZTS thin films grown on FTO coated glass, were examined for potential use in semitransparent solar cell applications. CZTS films were synthesized by spin coating of Zn-Cu-Sn metal precursors followed by heating and subsequent sulfurization at elevated temperature. The photocurrent response of CZTS film was

measured and compared for front and rear illumination. Results suggest spin coated grown CZTS films have significant potential for bifacial applications using transparent substrate.

5.5 References

[1]A Hubner, A.G. Aberle, and R. Hezel, Appl. Phys. Lett. 70 (1997) 1008.

[2]R. Hezel, W. Hoffmann, and K. Jaeger in Proceedings of the 10th European Photovoltaic Specialists Conference, Lisbon Kluwer Academic, Dordrecht, 1991, p. 511.

[3]A. Cuevas, A. Luque, J. Eguren, and J. Del Alamo, Sol. Energy 29 (1982) 419.

[4] P. K. Sarswat, M. L. Free, A. Tiwari, Phys. Status Solidi B, DOI 10.1002/pssb.201046477 (2011).

[5] P. K. Sarswat, M. L. Free, A. Tiwari, in: Mater. Res. Soc. Symp. Proc. Vol. 1288, Boston, USA, 2010.

[6] P. K. Sarswat, M. L. Free, A. Tiwari, in: Mater. Res. Soc. Symp. 2010, SESSION MM7: Transparent Conducting Oxides and Applications, Boston, USA, 2010.

[7] D. B. Mitzi, M. Yuan, W. Liu, A. J. Kellock, S. J. Chey, V. Deline and A. G. Schrott, Adv. Mater. **20,** 3657 (2008).

[8] A. Kränzl, R. Kopecek, B. Terheiden and P. Fath in Proceedings of 15th International Photovoltaic Science & Engineering Conference (PVSEC-15) Shanghai China 2005.

[9] L Schipper, S. Meyer, R. Howarth and R. Steiner in: Energy Efficiency and Human Activity: Past Trends, Future Prospects, (Cambridge University Press, Cambridge, 1997).

[10] Th.M. Friedlmeier, N. Wieser, Th. Walter, H. Dittrich and H.W. Schock in Proceeding of 14th European PVSEC and Exhibition (1997) P4B.10.

[11] K. Tanaka, N. Moritake, M. Oonuki, and H. Uchiki, Japanese Journal of Applied Physics 47 (2008) 598.

[12] Y. Miyamoto, K.Tanaka, M. Oonuki, N. Moritake, and H Uchiki, Jpn. J. Appl. Phys 47(2008) 596.

[13] S. Chen, X. G. Gong, A. Walsh and S. H. Wei, Appl. Phys. Lett. 94 (2009) 041903.

[14] H. Araki, A. Mikaduki, Y. Kubo, T. Sato, K. Jimbo, W.S. Maw, H. Katagiri, M. Yamazaki, K. Oishi, and A. Takeuchi, Thin Solid Films 517 (2008) 1457.

[15] J.J.Scragg, P.J. Dale, and L.M. Peter, Thin Solid Films 517 (2009) 2481.

[16] X. Zhang, X.Z. Shi, W.C. Ye, C.L. Ma, and C.M. Wang, Appl. Phys. A -Mater. 94 (2009) 381.

[17] C.P. Chan, H. Lam, K. Y. Wong, C. Surya, Mater, Res. Soc. Symp. Proc. 1123 (2009)06.

[18] PA Fernandese, PMP Salomé, and AF da Cunha, Thin Solid Films 517 (2009) 2519.

[19] J.J. Scragg, P.J. Dale, L.M. Peter, G. Zoppi, and I. Forbes, Phys. Status Solidi B 245 (2008) 1772.

[20] H. Katagiri, K. Jimbo, W.S. Maw, K. Oishi, M Yamazaki, H. Araki, and A.Takeuchi, Thin Solid Films 517(2009) 2455.

[21] Q.J. Guo, HW Hillhouse, and R Agrawal, J. Am. Chem. Soc. 131 (2009)11672.

[22] C Steinhagen, MG Panthani, V Akhavan, B Goodfellow, B Koo, and BA Korgel, J. Am. Chem. Soc. 131 (2009) 12554.

[23] T. Nakada, Thin Solid Films 480-481 (2005) 419.

[24] R. Memming, J. Electrochem. Soc. 125 (1978) 117.

CHAPTER 6

A COMPARATIVE STUDY OF CO-ELECTRODEPOSITED Cu_2ZnSnS_4 ABSORBER MATERIAL ON FTO AND MOLYBDENUM SUBSTRATE

6.1 Introduction

Most of the CZTS based solar cells [1-10] have been fabricated on Mo coated substrate by evaporation or sputtering, followed by annealing and sulfurization at elevated temperatures (250-550 ^{o}C). Earlier, various metal back contacts including Ni, Ag, Cu, Au, Pt, and Al have also been investigated for CIS (copper indium selenide) absorber material [11]. Some investigations have been carried out to compare properties of back contacts. These studies reveal that molybdenum is resistant to alloying with copper and indium, and it has a as low contact resistance with CIS, therefore, it is being used as a back contact. Despite many potential advantages of molybdenum back contact, it becomes difficult to fabricate semitransparent or bifacial solar cell because of its opaque nature. The possible fabrication of semitransparent $Cu(In_{1-x}Ga_x)Se_2$ (CIGS) photovoltaic device was suggested by Nakada *et al.* [12] for tandem and bifacial solar cell using FTO (Fluorinated tin oxide : SnO_2/F) as back contact. Nakada *et al.* [12] reported that the performance obtained from a device fabricated on Mo- coated substrate is

comparable to CIGS photovoltaic device fabricated on CIGS photovoltaic device fabricated directly on FTO coated glass substrates. Recently, Sarswat *et al.*[7] demonstrated the use of sol-gel synthesized CZTS (on FTO substrate) for bifacial solar cell applications. Another report by Sarswat *et al.* [9] discusses various back contacts on FTO, which were further utilized for growth of CZTS. These reports [7-12] suggest that CZTS device fabrication on alternative back contacts is viable and productive. A recent report discusses increases in already high molybdenum prices, which in turn will increase the expense of sputtered molybdenum coated glass [13]. An assessment of these points suggests that there is a need of alternate back contact materials such as FTO which can be utilized for CZTS based solar cell fabrications. In the view of these aspects, we report detailed comparisons of morphological, structural, optical and photoelectrochemical properties of co-electrodeposited CZTS thin films on transparent FTO and molybdenum coated glass substrates.

6.2 Experimental procedure

Electroplating was performed using an electrowinning cell in an isothermal water bath at 58°C. FTO and molybdenum coated glass substrates (area exposed to electrolyte = 0.25-0.50 cm^2) were used as working electrodes. Quantity of electrolyte used was 50 ml. Stochiometry of electrolyte solution was optimized by varying individual ionic species concentrations and monitoring response using factorial design of experiments approach [10,14]. The co-deposition of zinc-copper-tin was carried out using an electrolyte containing 0.004 M copper (II) sulfate pentahydrate, 0.15 M zinc chloride and 0.018 M sodium stannate. To determine the potential at which electrodeposition of all

constituent elements (Cu, Zn, Sn) can be done, linear sweep scans was conducted for electrolyte mentioned above (using SnO_2/F and molybdenum coated glass as the working electrodes). The V-I scans suggest that all equilibrium potentials for dissolved ions (Cu^{2+}, Zn^{2+}, Sn^{2+}) are greater than ~ -1.2 V. Hence co-electrodepositions were carried out in potentiostatic mode at a potential of ~ -1.6 V. Potassium sodium tartrate was used as a complexing agent. All electrochemical tests and electrodeposition were performed using EG&G 273 and Gamry PCI4/750 Potentiostats. Time of electrodeposition was precisely controlled to obtain a 1-2 μm thick as-deposited film. As-deposited films were soaked in deionized water and dried with nitrogen. A controlled sulfurization [9] (to reduce loss of conductivity) of cleaned films was carried out for 2 h in an argon environment with evaporated elemental sulfur. The annealing tube (alumina) was purged with argon for 25 min to displace air, prior to sulfurization. Elemental sulfur (99.9%), placed in a quartz boat, was held at a temperature of 150^{o} C as a sulfur source.

Thin films were characterized by scanning electron microscopy (SEM), atomic force microscopy (AFM), x-ray diffraction (XRD), Raman spectroscopy, Inductive Coupled Plasma – optical emission spectroscopy (ICP-OES), electrochemical impedance spectroscopy (EIS) and ultraviolet–visible (UV-Vis) spectroscopy. The surface SEM imaging was performed using an FEI NanoNova scanning electron microscope. Inductive coupled plasma spectroscopy was done using a Spectro geneses optical spectrometer. AFM (made by Veeco Instruments) measurements were carried out using Si_3N_4 cantilever in contact mode. Raman spectroscopy was carried out by using an R 3000 QE portable Raman spectrometer (made by Raman Systems). Wavelength of laser excitation for Raman measurements was 785 nm and the laser power was ~ 100 mW. The Raman

spectrometer provides good wavelength stability (less than 1cm^{-1} drift for over a 12 h period). Mott- Schottky analysis and photoelectrochemical measurements were carried out using a Gamry PCI4/750 Potentiostat. The CZTS electrodes were immersed in an aqueous solution of 0.07 M $Eu(NO_3)_3.6H_2O$, together with a saturated calomel reference electrode (SCE) and a platinum counter electrode for measurements. The advantages of europium nitrate have been discussed elsewhere [7]. To compare the photocurrent responses of the CZTS films, change in transient photocurrents were monitored, which were generated during alternating illumination from a high intensity white light optic illuminator. A DU 730 UV/Visible scanning spectrophotometer was used in wavelength scanning mode for optical transmittance measurements.

6.3 Results and discussion

Figure 6.1 shows a characteristic θ-2θ XRD pattern of CZTS thin films grown on FTO and molybdenum substrates. This pattern matches very well with the kesterite structure of CZTS (JCPDS card 26-0575). However, to confirm absence of phases whose characteristic XRD pattern is very similar to XRD pattern of CZTS, additional characterization was carried out. Figure 6.2 shows the Raman spectrum of the films over the range 275 to 400 cm^{-1}. In the Raman spectrum a major peak located at 338 cm^{-1}, and two minor peaks at 369 cm^{-1} and 287 cm^{-1} can be seen. This spectral data is in good agreement with the reported Raman spectra of CZTS [7, 8, 10]. No distinct peak corresponding to zinc sulfide, copper sulfide and tin sulfide is observed. It can also be seen that there is a lack of peaks or shoulders corresponding to CTS (copper tin sulfide) at 355, 348, 351, and 295 cm^{-1} [15]. This suggests that CZTS films grown on both

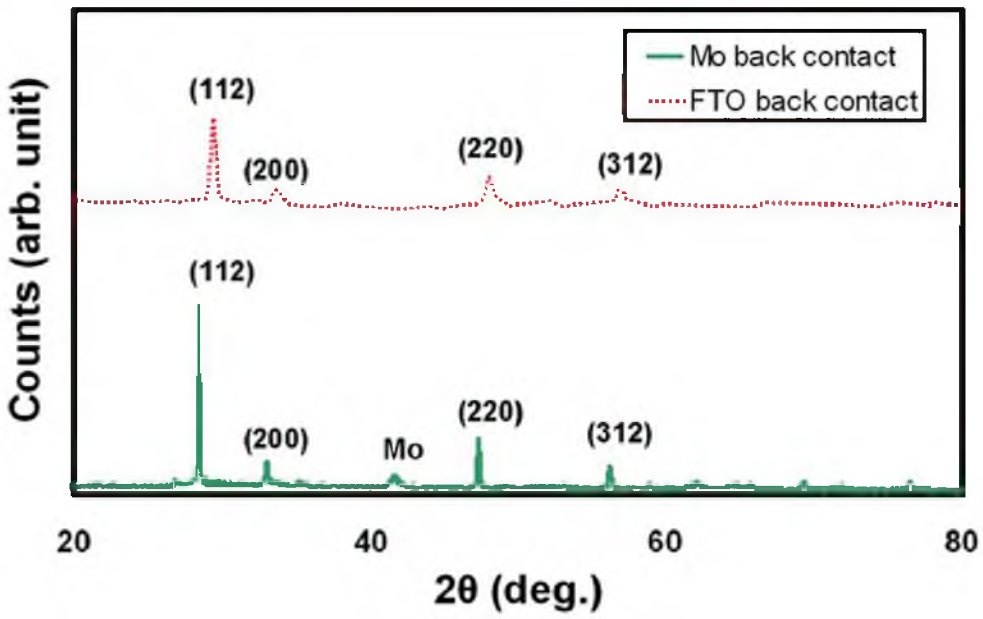

Figure 6.1: XRD pattern of CZTS films grown on FTO and molybdenum substrates.

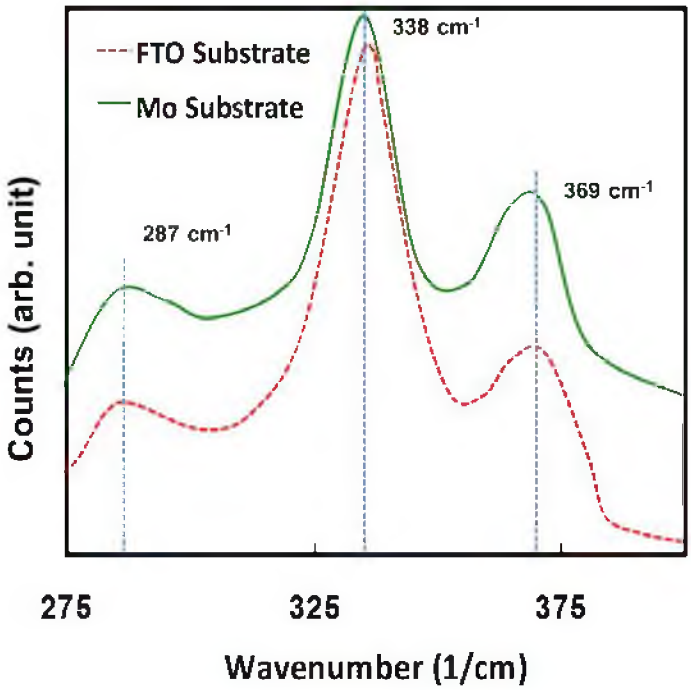

Figure 6.2: Raman spectra of CZTS films grown on FTO and Mo substrates.

substrate (FTO and Mo) are relatively pure. Additional examination of purity was conducted by monitoring melting behavior of CZTS film which shows that film melts far above the melting point of CTS (~ 734°C) and very close to melting of CZTS (~ 815°C) [16,17]. The chemical composition analysis of co-deposited film was done by ICP-OES using smart analyzer vision software. The results shows Cu : Zn : Sn ratio of 2 : 1 : 1 , which is desired for stoichiometric CZTS formation.

Films morphology and thickness were analyzed and compared using SEM and AFM. SEM micrographs of a 40×30 μm^2 area of as-deposited Cu-Zn-Sn films and sulfurized films are shown in Figure 6.3-6.6. It can be seen that for FTO back contact, as deposited film (Figure 6.3) appears to be uniform with fewer pores and a grain size of ~ 1.0 μm. On the other hand for Mo back contact (Figure 6.4) granules are large (size ~3-5 μm) and they consists of agglomerated small grains. It also can be seen that the surface is porous with a uniform grain distribution. For FTO back contact, after sulfurization, many grains are flat (Figure 6.5) and large sized ~ 3 μm. For Mo back contact, after sulfurization it is observed that in most of the region the surface is denser (average grain size ~ 1.5 μm) compared to as deposited film. It can be seen that grains are fused together in most regions of the surface (Figure 6.6). It is also observed that adhesion of the CZTS film on FTO-coated substrate is better than on Mo-coated substrate. Cross sectional SEM images (Figure 6.7-6.8) are shown for CZTS grown on FTO and Mo back contacts. For FTO, CZTS film appears to be grown uniformly. However, for Mo, CZTS film is rougher as compare to CZTS on FTO. For high performance photovoltaic devices grains with good interconnection is required, which was observed for CZTS film grown on the Mo-coated back contact. Large grains with good adhesion, which is also desirable,

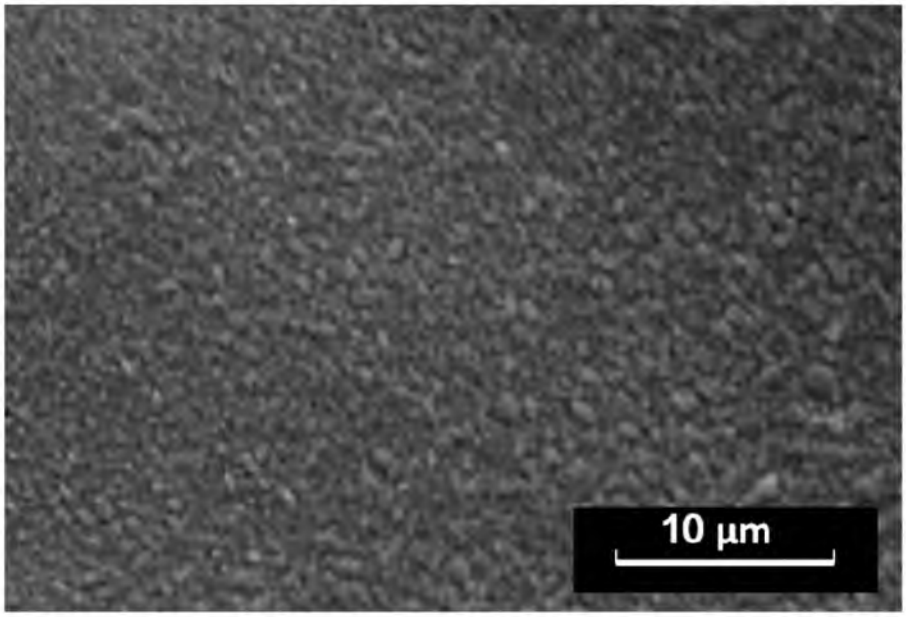

Figure 6.3: SEM image of surface of as deposited Cu-Zn-Sn thin film on FTO substrate.

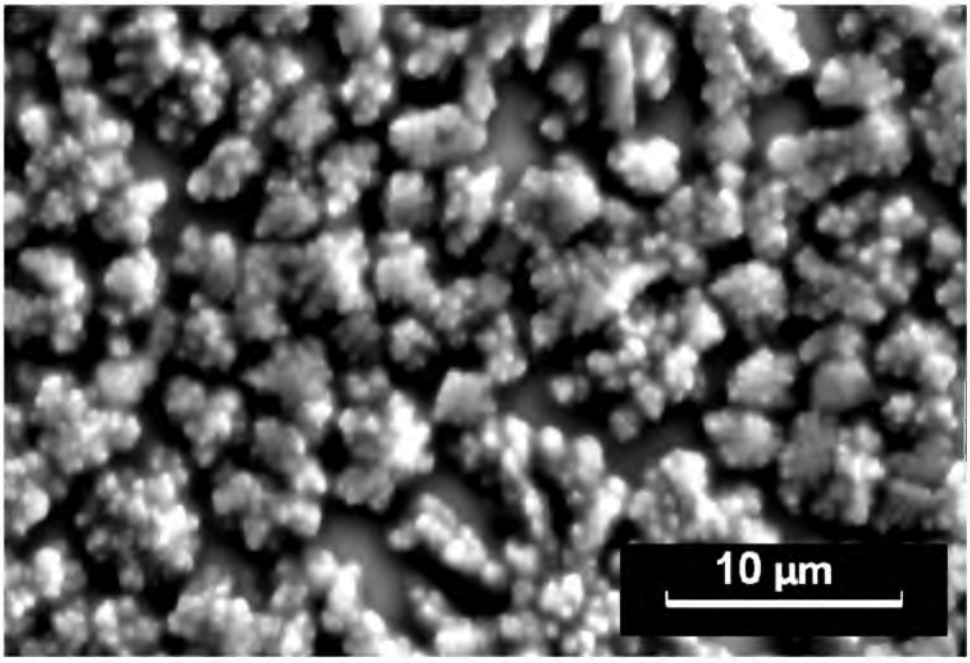

Figure 6.4: SEM image of surface of as deposited Cu-Zn-Sn thin film on Mo substrate.

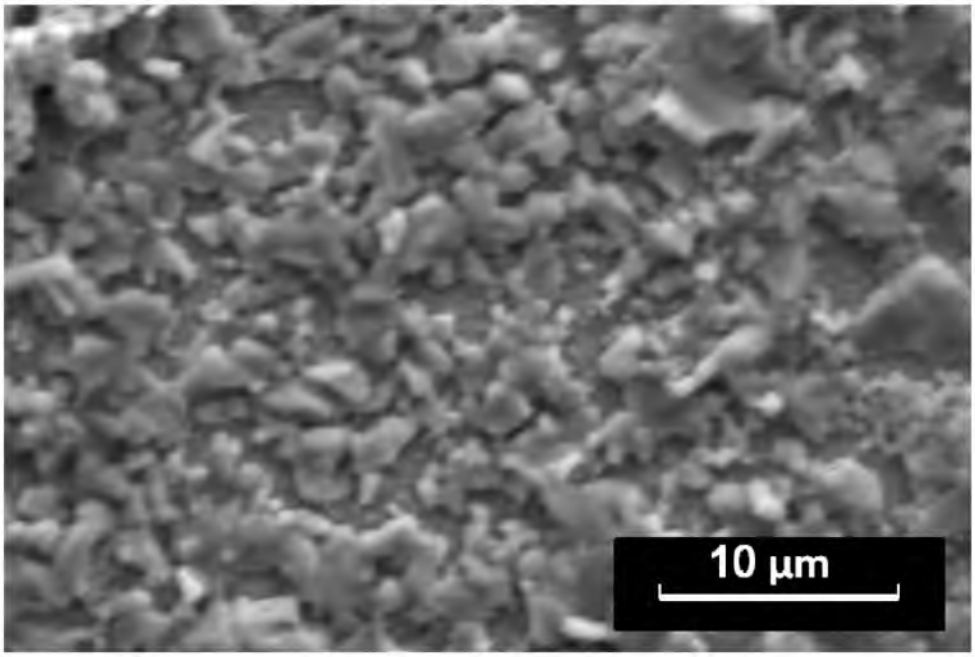

Figure 6.5: SEM image of surface of sulfurized CZTS thin film on FTO substrate.

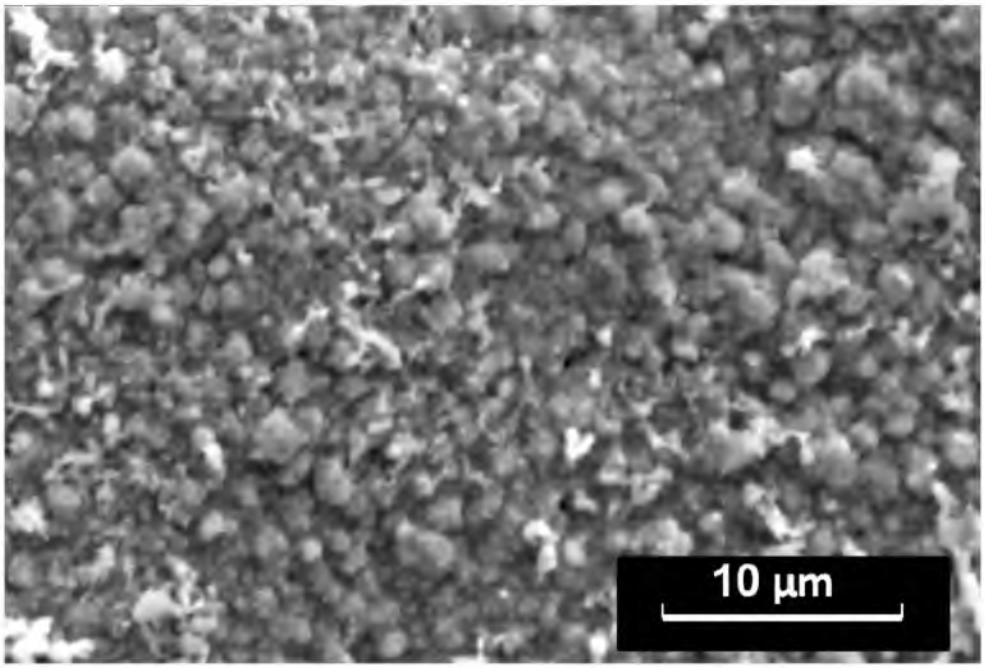

Figure 6.6: SEM image of surface of sulfurized CZTS thin film on Mo substrate.

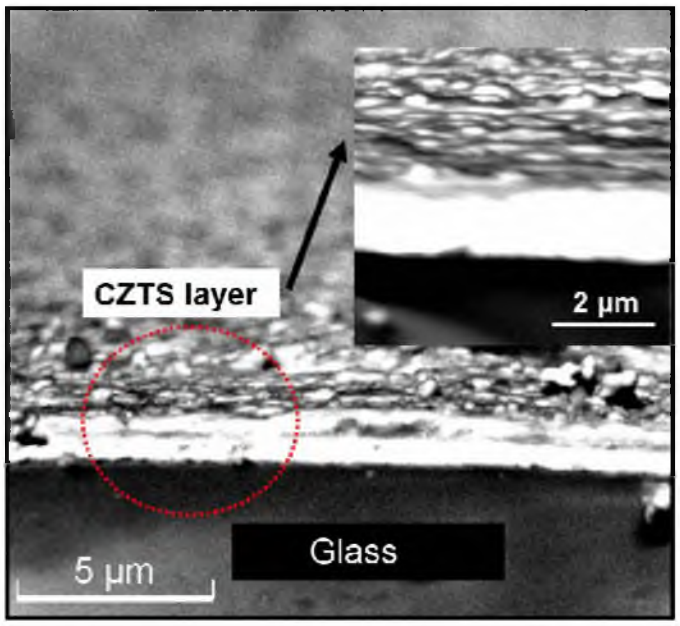

Figure 6.7: Cross sectional SEM image of CZTS thin film on FTO substrate. A magnified image is shown in inset.

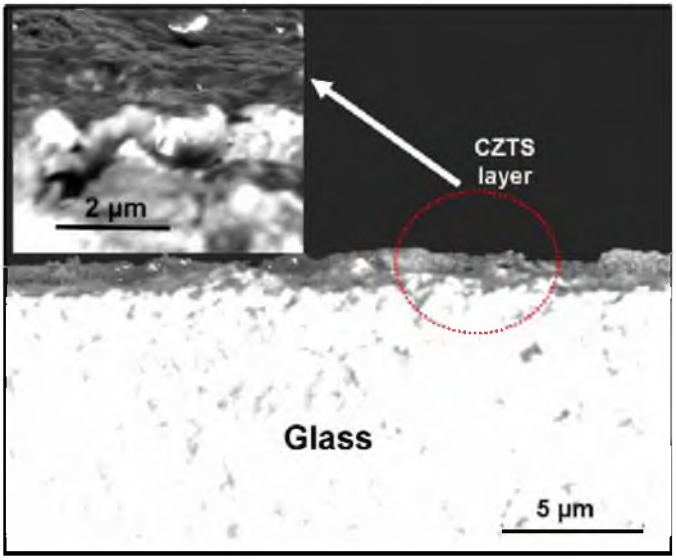

Figure 6.8: Cross sectional SEM image of CZTS thin film on Mo substrate. A magnified image is shown in inset.

were observed for FTO-coated back contact. An AFM 3D micrograph of 100 μm^2 area of an annealed CZTS film on FTO and Mo back contact is shown in Figure 6.9-6.10. Vertical height between the lowest feature and the highest feature of film was ~ 644nm (for FTO back contact) and ~ 826 nm for Mo back contact. Several large and distinct grains can be seen in CZTS film grown on FTO back contact. However, fused grains can be seen in most regions of the CZTS film surface grown on the Mo-coated substrate. This observation is consistent with SEM images obtained for sulfurized CZTS films. Difference in microstructure of CZTS film can be attributed to different alloying behavior, different interface defect density, and different diffusion properties of Mo and FTO for CZTS /constituent elements [11, 12].

The Doping density of absorber layers were determined by measuring the apparent capacitance (unit area) as a function of potential and is based on the Mott- Schottky relationship [18]:

$$\frac{1}{C_{sc}^2} = \frac{2}{e\varepsilon\varepsilon_0 N}\left[E - E_{FB} - \frac{K_B T}{e}\right] \qquad (6\text{-}1)$$

where C_{sc} is capacitance of the space charge region, ε_0 is dielectric constant of the semiconductor (10 for CZTS), ε_o is permittivity of free space, N is the acceptor concentration for a p-type semiconductor, E is the applied potential (biased voltage), K_B is Boltzmann's constant, e is the electronic charge and E_{FB} is flat band potential of film [18,19].

Mott-Schottky plots ($1/C^2$ vs. E) using Gamry Echem Analyst^{TM}, are shown in Figure 6.11- 6.12 for a CZTS thin film deposited on FTO and Mo coated glass surface. The donor density can be calculated from the slope, and the flat band potential can be

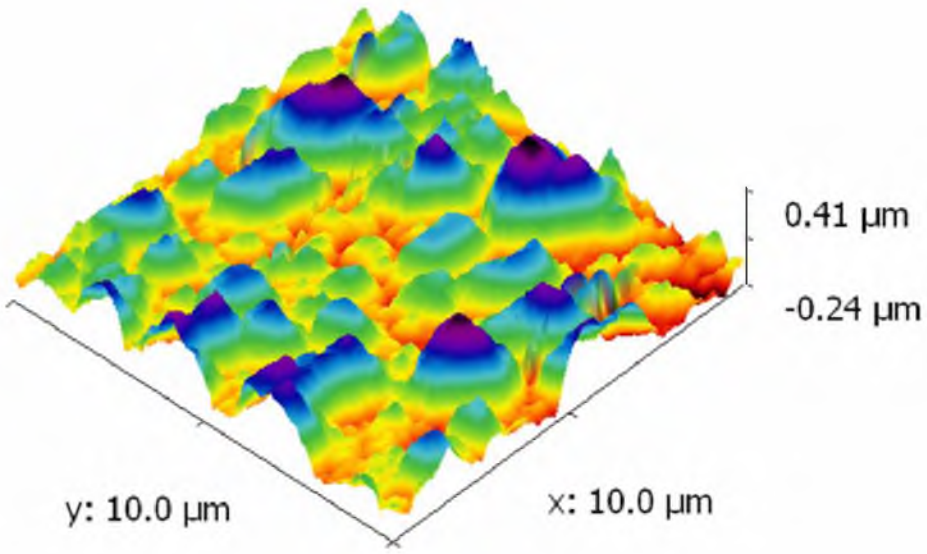

Figure 6.9: AFM 3D rendering of CZTS thin film grown on FTO substrate.

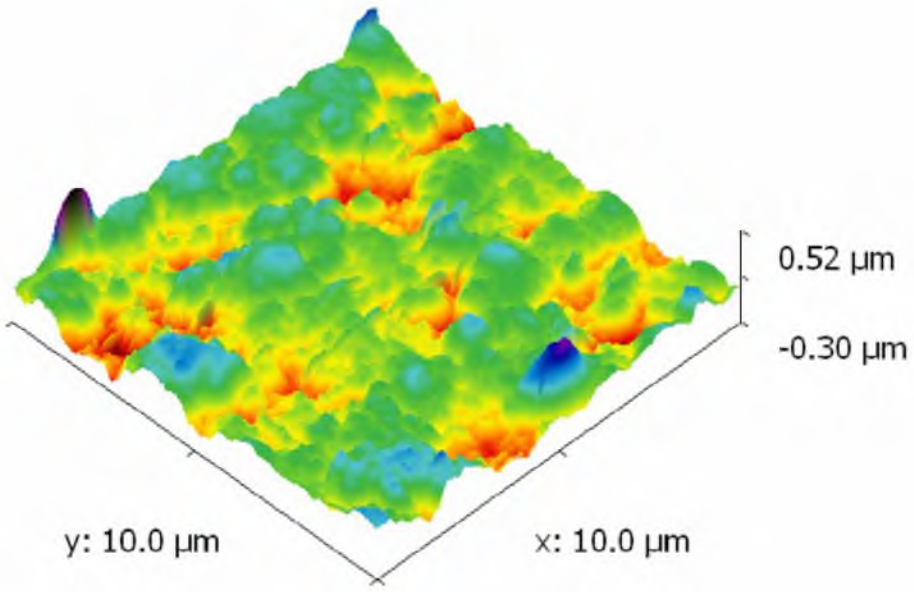

Figure 6.10: AFM 3D rendering of CZTS thin film grown on Mo substrate.

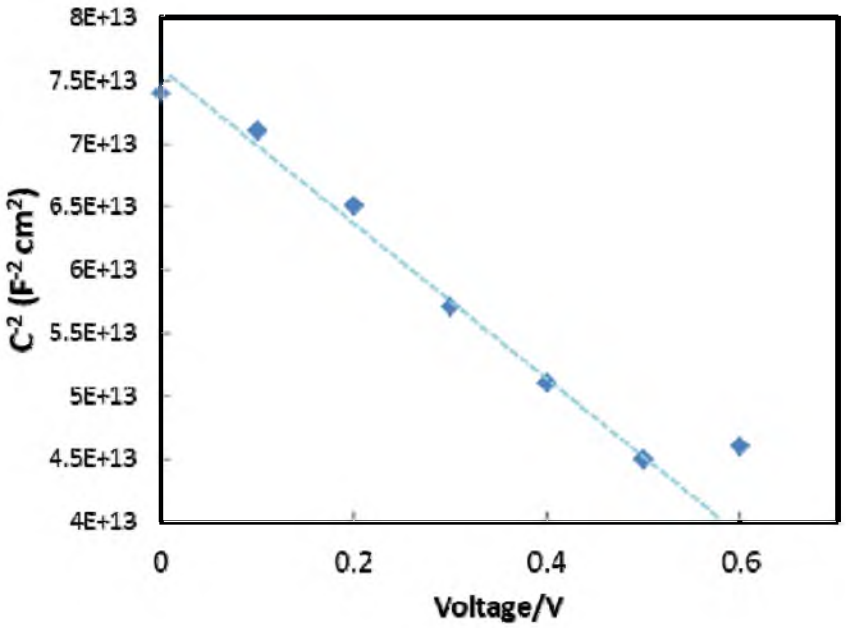

Figure 6.11: Mott-Schottky plot for CZTS thin film grown on FTO coated glass substrate. An electrochemical test was conducted using europium redox couple at room temperature [7].

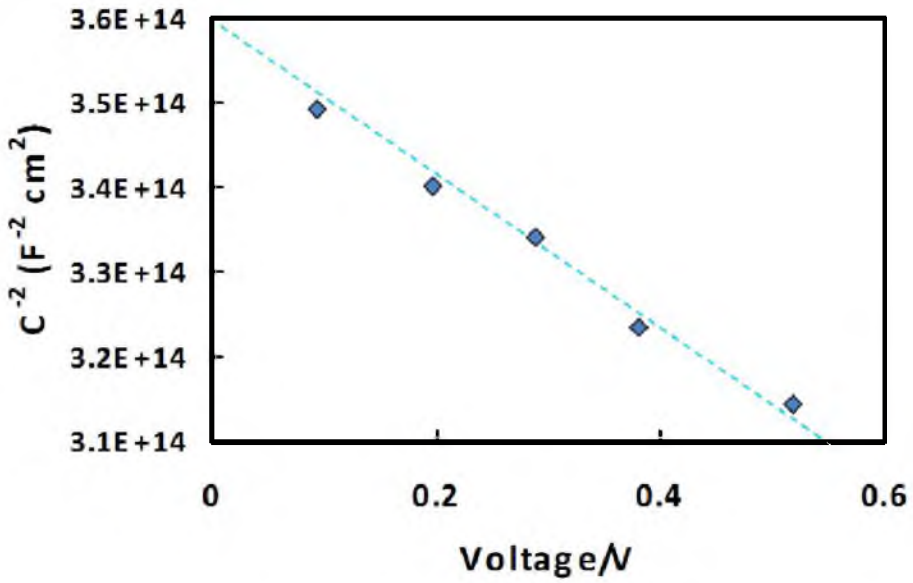

Figure 6.12: Mott-Schottky plot for CZTS thin film grown on Mo- coated glass substrate. An electrochemical test was conducted using europium redox couple at room temperature [7].

determined by extrapolation to $1/C^2 = 0$. The obtained value of the charge carrier concentration for FTO back contact is ~ $2.35 \times 10^{15}/cm^3$ while for Mo back contact its value is ~ $1.75 \times 10^{15}/cm^3$. These values of doping density are close to the doping density ~ $(0.5\text{-}5) \times 10^{15}/cm^3$, reported by Scragg *et al.* (which was obtained by extrapolation of external quantum efficiency data) [20]. It can also be seen that gradient of curve did not change very significantly in the potential range 0-0.5 V, which indicates that the material composition of absorber layer is relatively uniform across its depth [20].

The optical characterizations of annealed films were performed using UV-VIS optical transmission spectroscopy. Using transmittance data from absorption spectra the band gap can be evaluated:

$$\alpha = A(h\nu - E_g)^{1/2} \qquad (6\text{-}2)$$

where α is the absorption coefficient, A is a constant, E_g is the band gap and $h\nu$ is the incident photon energy [7]. Figure 6.13 shows α^2 as a function of incident photon energy for CZTS films deposited on FTO coated glass. By extrapolating the α^2 vs. photon energy curve to zero, the band gap was evaluated to be ~1.45 eV, which is consistent with reported literature values [3-10].

A comparison of photocurrent response for both films was done by recording linear scan voltammograms (shown in Figure 6.14) during flashing light illumination (incident power on substrate ~0.20 mW/cm^2) by the potentiostat using Gamry Instruements virtual front panel software. Both annealed films exhibit p-type photoactivity, which was revealed by cathodic photocurrent response and Mott- Schottky behavior. The hot probe method was implemented, which also confirms that majority carriers in these films are

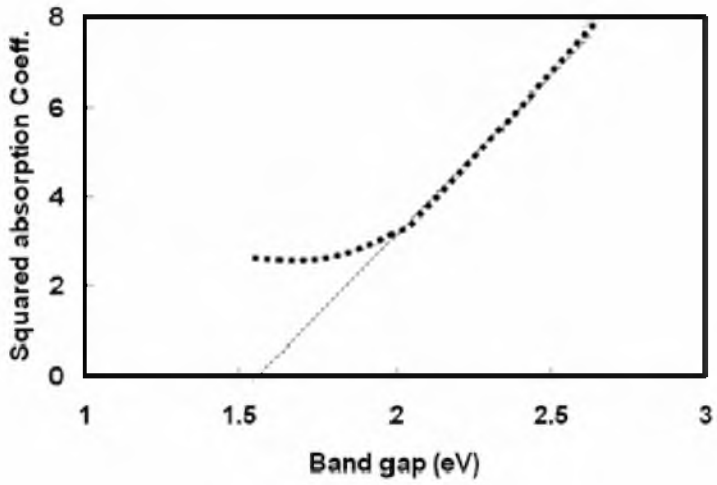

Figure 6.13: Squared absorption coefficient (α^2) versus photon energy ($h\nu$) for CZTS film grown on FTO substrate.

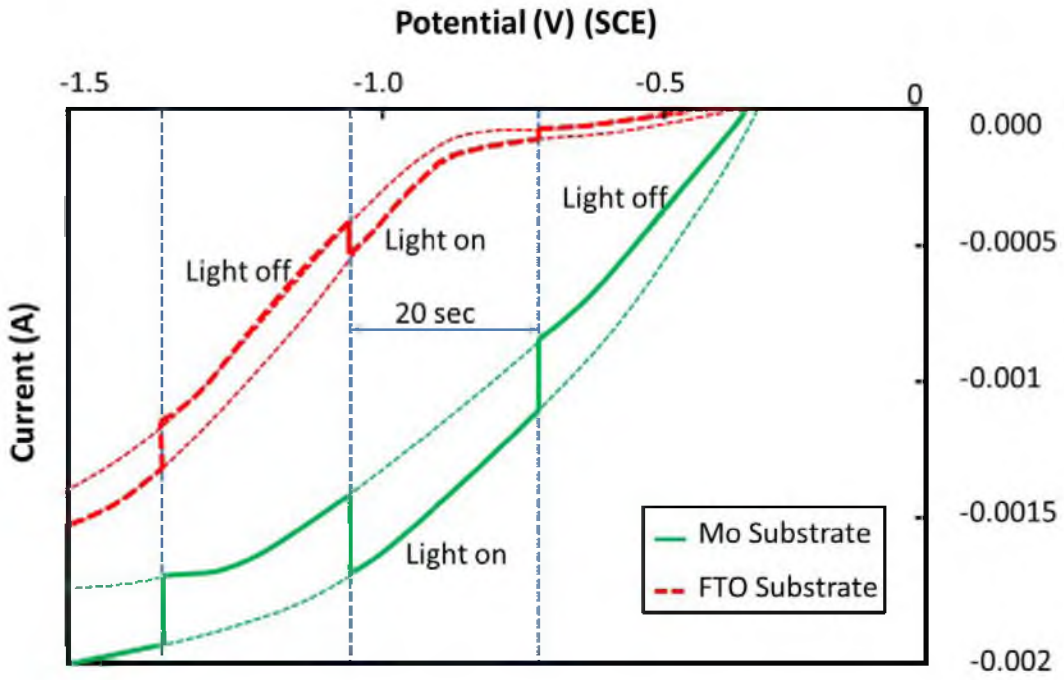

Figure 6.14: A comparison of photoelectrochemical response of CZTS films grown on FTO and Mo back contact.

holes. A portion of the I-V curve in potential range (-1.5 V to 0.0 V) versus a SCE is shown for both films. The change in cathodic photocurrent was ~ 0.0003A at saturation (for Mo back contact), while photocurrent change was ~ 0.00018 A for FTO back contact. It can be seen that measured photoelectrochemical response for CZTS films grown on FTO is ~ $2/3^{rd}$ of that obtained for CZTS films grown on Mo back contact. It is well known that use of Mo back contact promotes ohmic contact due to formation of molybdenum sulfide at Mo-CZTS interface [21, 22]. However, there is lack of significant information regarding band gap engineering of FTO-CZTS contact. It is anticipated that reduced photocurrent response in case of FTO back contact is due to quasi-ohmic behavi -or of FTO-CZTS contact. Increased resistivity of FTO back contact after elevated temperature sulfurization is also a factor responsible for reduced photocurrent performance [9].

6.4 Summary

In summary, a comparison of a low cost, highly scalable co-electrodeposition method for production of CZTS thin films on FTO and molybdenum coated glass surfaces is demonstrated. CZTS films were synthesized by co-electrodeposition of Zn-Cu-Sn metal films followed by elevated temperature sulfurization. Films were found to be kesterite CZTS with holes as dominant charge carriers. Structural and morphological characterization of films suggests that doping density of both films are ~ $10^{15}/cm^3$. Photoelectrochemical response exhibited by the films grown on molybdenum substrate is greater than that obtained for film grown on FTO substrate.

6.5 References

[1] D. B. Mitzi, M. Yuan, W. Liu, A. J. Kellock, S. J. Chey, V. Deline, and A. G. Schrott, Adv. Mater. 20 (2008) 3657.

[2] L Schipper, S. Meyer, R. Howarth, and R. Steiner, *Energy Efficiency and Human Activity: Past Trends, Future Prospects*, (Cambridge University Press, Cambridge, 1997).

[3] H. Araki, Y. Kubo, A. Mikaduki, K. Jimbo, W. S. Maw, H. Katagiri, M. Yamazaki, K.Oishi, and A. Takeuchi, Sol. Energy Mater. Sol. Cells 93(2009) 996.

[4] H. Araki, A. Mikaduki, Y. Kubo, T. Sato, K. Jimbo, W. S. Maw, H. Katagiri, M. Yamazaki, K.Oishi, and A. Takeuchi, Thin Solid Films 517 (2008) 1457.

[5] H. Araki, Y. Kubo, K. Jimbo, W. S. Maw, H. Katagiri, M. Yamazaki, K.Oishi, A. Takeuchi, Phys. Status Solidi C 6 (2009) 1266.

[6] P. K. Sarswat, M. L. Free, and A. Tiwari, Phys. Status Solidi B 248 (2011) 2170.

[7] P. K. Sarswat and M. L. Free, Phys. Status Solidi A 208(2011) 2861.

[8] P. K. Sarswat, M. L Free, A. Tiwari, and Michael Snure, Thin Solid Films 520(2012) 1694.

[9] P. K. Sarswat, M. L. Free, and A. Tiwari, Mater. Res. Soc. Symp. Proc. 1315 (2011) mm07.

[10] P. K. Sarswat, M. L. Free, and A. Tiwari, Mater. Res. Soc. Symp. Proc. 1288 (2011) g06.

[11] J. H. Scofield, A. Duda, D. Albin B. L. Ballard, P. K. Predecki, Thin Solid Films 260 (1995)26.

[12]T. Nakada, Thin Solid Films 480-481(2005) 419.

[13].http://www.marketwatch.com/story/molybdenum-prices-to-rise-55-in-two-years-jpm-2010-01-14

[14] P. K.Sarswat, M.L.Free, *Copper 2010,* Electrowinning and electrorefining 4 (2010)1649.

[15] P.A. Fernandese, P.M.P Salomé, and A.F.da Cunha, Thin Solid Films 517 (2009) 2519.

[16] G H Moh, Chem. Erde 34 (1975)1.

[17] S. Fiechter S, M. Martinez, G. Schmidt, W. Henrion ,Y. Tomm, J. Phys. Chem. Solids 64 (2003)1859.

[18] F.Cardon, W. P. Gomes, J.Phys. D: Appl. Phys. 11 (1978) L63.

[19] J.J. Scragg, P.J. Dale, L.M. Peter, G. Zoppi, and I. Forbes, Phys. Status Solidi B 245, (2008)1772.

[20] P. J. Dale, K. Hoenes, J. J. Scragg, S. Siebentritt, 34th IEEE Photovoltaic Specialists Conference PVSC 265 (2009) 02085.

[21] K. Wang, O. Gunawan, T. Todorov, B. Shin, S. Chey, N. Bojarczuk, D. Mitzi, S. Guha, Appl. Phys. Lett 97 (2010)143508.

[22] J. Spies, R. Schafer, J. F. Wager, P. Hersh, H. Platt, D. Keszler, G. Schneider, R. Kykyneshi, J. Tate, X. Liu, A. D. Compann, W. N. Shafarman, Sol. Energy. Mat. Sol.Cells. 93 (2009)1296.

CHAPTER 7

A STUDY OF INCREASED RESITIVITY OF FTO BACK CONTACT FOR CZTS BASED ABSORBER MATERIAL GROWN BY ELECTRODEPOSITION-ANNEALING ROUTE

7.1 Introduction

CZTS (Copper zinc tin sulfide) thin films have been synthesized on transparent conducting oxide (TCO) back contacts on a glass substrate, allowing sun light to pass through the entire solar cell. Aqueous solution based co-electrodeposition followed by elevated temperature sulfurization, was used to grow CZTS on transparent fluorinated tin oxide. Loss in conductivity of FTO is observed after sulfurization, causing reduced device efficiency. Increased resistivity of the FTO is likely due to out-diffusion process. A systematic study of resistivity of back contact at various sulfurization temperatures and times is discussed in this chapter. Various remedial measures for improved conductivity of back contact were proposed and conducted.

A device using FTO as a back contact and CZTS as an absorber material can be fabricated, so that semitransparent as well as bifacial solar cells can be made. Though the proposed TCO backed structure has also been reported for CIGS based cells, it can also be used for CZTS based solar cells [1]. However, despite several advantages of the

proposed TCO/CZTS solar cell, elevated temperature sulfurization causes enormous loss of conductivity of the FTO back contact, which results in reduced performance [1]. The loss of conductivity was systematically studied, and processing parameters were optimized in this study. The optimization includes temperature, time of sulfurization, and geometry of sulfurization. Remedial measures to enhance conductivity included indirect and slow sulfurization, and incorporation of a thin layer of Pd, Pt or other element, which eliminates the formation of a double junction across the cell.

7.2. Experimental details

Cu_2ZnSnS_4 films were successfully fabricated using a specially designed electrochemical method followed by sulfurization. Electrodepositon of constituent metal alloy film was carried out on conducting substrates using a platinum counter electrode and a saturated calomel reference electrode. A unique single bath composition was formulated to grow Cu_2ZnSn (CZT) films. Electrowinning cells surrounded by a water jacket were used to perform the electrodeposition at the controlled temperature of 55°C. All electrochemical tests and electrodeposition were performed using EG&G 273 and Gamry PCI4/750 Potentiostats. After electrodeposition, films were rinsed in deionized water and dried with nitrogen gas. Cleaned films were sulfurized by annealing in a sulfur environment. Annealing was performed in an argon environment with evaporated elemental sulfur (99.99%) in a tube furnace. Figure 7.1 shows a schematic diagram of the synthesis process. All as deposited films were prepared in such a manner that half of the film area remains uncoated with CZT. The FTO exposed area was simultaneously annealed along with CZT coated FTO film. The sulfurization is carried out at different

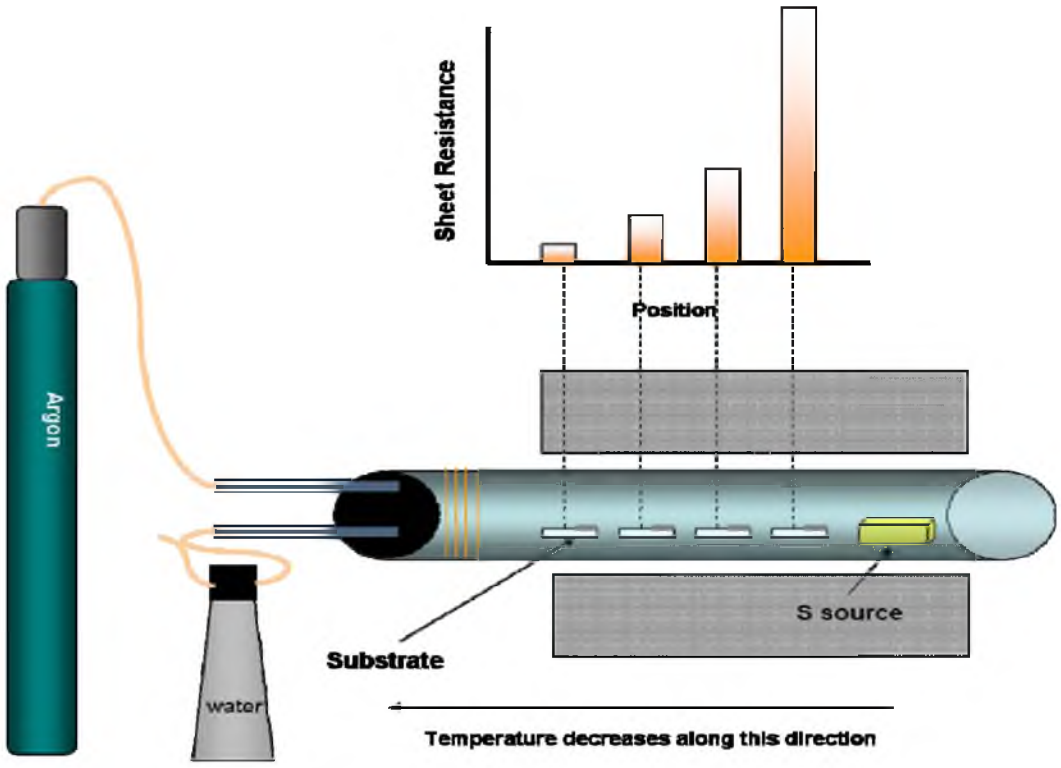

Figure 7.1: A schematic diagram showing sulfurization and increased sheet resistance of FTO film.

exposure times for time dependent conductivity degradation. Annealing was performed at different substrate temperatures (400°C to 600° C) for evaluation of temperature effects. An additional set of annealing experiments were also conducted in argon environment without sulfur. Sheet resistance was measured with and without sulfur for comparison. A high extent of sulfurization is expected when the substrate is near the sulfur source. Substrates half-coated with CZT were kept inside the furnace at different places relative to the sulfur source as shown in Figure 7.1. A separate set of experiments was also conducted, where some FTO coated samples were kept directly exposed to a heated sulfur environment while some samples were kept in such a manner so that FTO area is protected from direct exposure to the heated sulfur environment.

7.2.1 Measurement of sheet resistance

A Four – point probe method was used to measure sheet resistance of sulfurized FTO film [2]. A small galvanostatic current from a potentiostat is passed through two outer probes and the voltage is monitored between two inner probes. Sheet resistance is given by [2]:

$$R_s = \frac{V}{I} CF \quad \Omega/square \qquad \text{(here 'CF' is the correction factor)} \qquad (7\text{-}1)$$

Sheet resistance is measured for sulfurized FTO film at different places. Sheet resistance of CZTS back contact is also measured after removing CZTS.

7.2.2 Inner thin layer coating

Small thin layers~ 25-70 nm of different metals including palladium, platinum, copper, cobalt, nickel and gold were individually electrodeposited prior to growth of CZTS. CZTS was grown on half of the area so that sheet resistance of film with a Pt, Pd, Cu, Ni, Co, Ag or Au base layer can be measured. A schematic diagram of CZTS on the thin metal layer (Pt, Pd, Cu, Ni, Co, Ag, or Au) is shown in Figure 7.2.

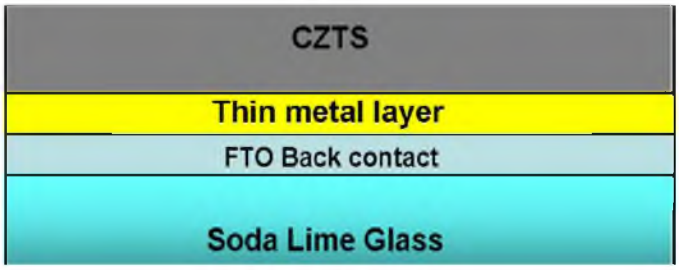

Figure 7.2: A schematic diagram showing cross section of various layers.

7.3. Discussion

The sheet resistance of exposed FTO film is measured and shown in Figure 7.3 using samples placed at various locations inside the annealing tube as shown in Figure 1. The FTO film was kept near the sulfurization source (1 cm) shows very high sheet resistance while the film located far away from the source shows less sheet resistance. A regular trend is observed, which can be manifested as a lowering of sheet resistance as distance from the sulfur source of exposed FTO film increases. The sheet resistance of film 18 cm from the sulfurization source is of order of few ohms but this value is very high (~ megaohm), adjacent 1cm to the source. Another set of experiments where sheet resistance was measured inside the grown CZTS film reveals that sheet resistance also increased tremendously after sulfurization. Though this trend is not very similar to that of exposed FTO film, a five order of magnitude change in sheet resistance can be seen (Figure 7.3) over the 16 cm spread in sulfurization position.

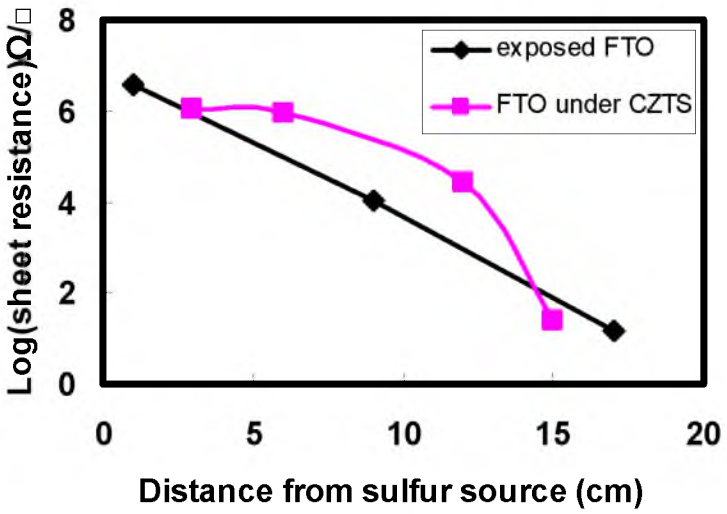

Figure 7.3: Sheet resistance of FTO thin film after sulfurization at 560° C (black); Sheet resistance of FTO thin film that was under a layer of CZTS during the sulfurization process (560° C) after removing the CZTS layer (pink).

The result of experiments, where sulfurization is carried out at different temperatures, is shown in Figure 7.4. The sheet resistance increases at a very slow rate up to 450° C, after that, a very large change is observed. Once the temperature increases to 500° C, the change in sheet resistance reduces at a specific location from the sulfur source. The sheet resistance dependence with temperature is also shown in Figure 7.4, when annealing is carried out in an argon environment. The trend of increment is very similar to that observed for sheet resistance measured for annealing in a sulfur environment. However, the sheet resistance value for the annealing in a sulfur environment is much higher than that observed for heating in an argon environment for temperatures greater than 450° C.

The sheet resistance comparison performed at different orientations is shown in Fig. 7.5. The film which is directly exposed to sulfur environment shows very high sheet resistance while film protected from direct exposure shows lower value. The Figure 7.6

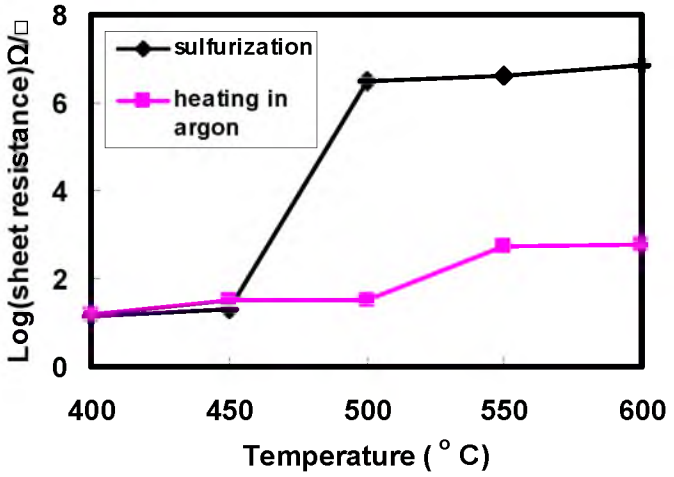

Figure 7.4: Sheet resistance of exposed FTO thin film, sulfurized at different temperature (black) ; Sheet resistance of FTO thin film, heated in argon environment (pink).

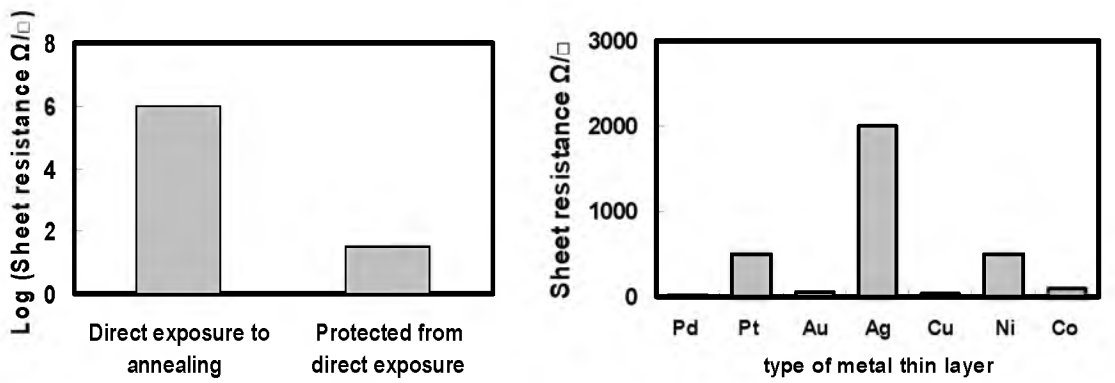

Figure 7.5: Sheet resistance of FTO thin film, heated in sulfur environment (left); Figure 7.6: Sheet resistance of metal thin films coated on FTO, annealed in sulfur environment (right).

represents the results of sheet resistance measurements after sulfurization for different metal layers coated on FTO. The sheet resistance value is very high for the Ag layer, and lowest for the Pd layer. The possible explanation of higher sheet resistance in the case of the Ag layer is formation of Ag_2S and sulfur diffusion across the film. On the other hand, palladium reduces the effect of sulfiding on sheet resistance. Although incorporation of thin Pd layer improves conductivity of the back contact, there is some trade-off due to a loss of film transparency. The result of most of the measurements shows very high sheet resistance values at high temperatures (>500^{o} C) and direct excess sulfurization. These measurements values are consistent with those obtained for FTO thin layers that were under a layer of CZTS. However when the substrate is kept far away (>10 cm) from the sulfurization source, sheet resistance increment is not large. Indirect exposure and annealing at lower temperature (< 450^{o} C) also results in increased resistance value, but the value is low. The possible explanation of sheet resistance change is related to diffusion. When fluorine is doped in tin oxide films, each F^{-} anion replaces an O^{2-} anion in the lattice and the substituted anion introduces more free electrons [3]. This results in

an increase in free electrons and decreases the value of sheet resistance. On the other hand when F^- leaves the lattice, a deficiency of free electrons is created, which results in an increase of resistance. When removal of F^- dominates, sheet resistance increases with an increase of temperature [1]. Another post deposition annealing effect is the creation of oxygen vacancies which may result in reduced resistivity, but this result suggests that this phenomenon is not dominant. A comparative analysis carried out in this report (annealing in sulfur environment and annealing in argon environment) indicates sheet resistance value is very high at higher temperatures (> 500 ^{o} C) when annealed in a sulfur environment. The possible explanation is the formation of a bad conducting layer (of sulfur and other secondary phases), observed for samples which are sulfurized at temperatures greater than 450^{o} C. It is believed that low conductivity of sulfur also assists to enhance sheet resistance of film. No such layer is observed for lower temperature annealing. Similarly the layer formation is less for samples that are kept far away from sulfur source.

The loss of conductivity is reduced when annealing is carried out at low temperatures (400-450^{o}C) as well as indirect exposure of film to sulfur. Raman spectroscopy of annealed samples at different temperature was conducted and the results of Raman spectroscopy of sample annealed at 440^{o} C is shown in Figure 7.7. In the Raman spectrum peaks located at 338 cm^{-1} and 370 cm^{-1} can clearly be seen, which are in good agreement with previously reported Raman spectra of CZTS [4]. The above results are also consistent with Raman peaks observed for samples kept at far away and for indirect exposed samples. Hence, it can be concluded that CZTS thin films can be grown on FTO even at low temperatures with less loss of FTO conductivity. Similarly, CZTS

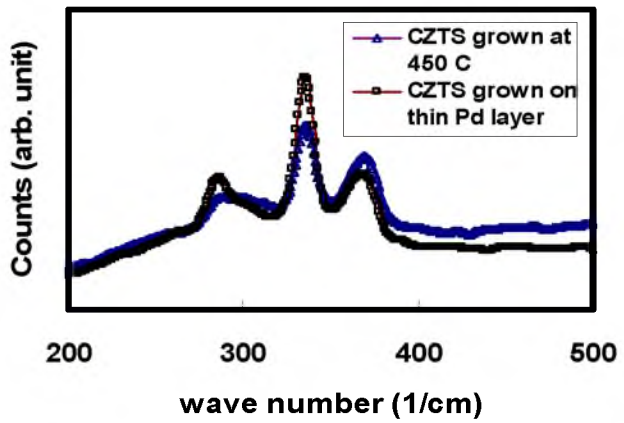

Figure 7.7: Raman spectra of CZTS thin film: (i) grown at temperature 440^{o} C, shown by blue triangle; (ii) grown on Pd inner layer at temperature 550^{o} C (shown by square).

grown on thin Pd base coating on FTO (see Figure 7.2) also shows a clean spectrum suggesting phase purity as revealed by Raman analysis (Fig. 7.7). In the Raman spectrum, peaks located at 289 cm^{-1}, 338 cm^{-1} and 370 cm^{-1} can clearly be seen, which are in good agreement with previously reported Raman spectra of CZTS [4]. This result is consistent with that obtained for Cu and Au base coating.

7.4. Conclusions

The analysis of sheet resistance measurements implies sheet resistance increases dramatically in the case of elevated temperature sulfurization (greater than 500^{o}C). The results also indicate that direct sulfurization results in very high sheet resistance value. These results suggest that low temperature annealing ~ 440^{o}C can result in the formation of CZTS phase with less loss of conductivity than at higher temperatures. Another remedy to reduce resistance is use of thin Pd layer.

7.5 References

[1] T. Nakada, Thin Solid Films 480-481(2005) 419.

[2] F.M. Smits, Measurement of sheet resistivities with four-point probe, Bell Syst. Tech. J. 37 (1958)711.

[3] E. Elangovan, K. Ramamurthi, Applied surface science 249 (2005) 183.

[4] P. A. Fernandese, P. M. P. Salomé, A. F.da Cunha, Thin Solid Films 517 (2009)2519.

CHAPTER 8

AN EVALUATION OF DEPLETION LAYER PHOTOACTIVITY IN Cu_2ZnSnS_4 THIN FILM

8.1 Introduction

Alternative classical solid state devices and their analogs are being promoted and examined for various important applications including photoelectrochemical cells [1]. One example of this is the use of the semiconductor-electrolyte interface as a testing analog for a photovoltaic cell. A major advantage of the semiconductor-electrolyte interface is easy formation of Schottky barriers using hetro-junctions [2]. A nondestructive way of photovoltaic property evaluation is an additional benefit. Although many theoretical models have been proposed to obtain current-voltage (J-V) behavior of semiconductor-electrolyte interfaces, a detailed analysis of photo-electrochemical kinetics has been carried out by Butler [2] based on the Gärtner [3] model. In the analysis by Butler [2], charge transport within a semiconductor was assumed as the rate determining step. However, in further studies treatment of transport and recombination of carriers within semiconductors was included to produce an improved model. Some studies also show the importance of interfacial transfer of the photoelectron. Most of these modified models were utilized to discuss electron transfer kinetics at an illuminated

semiconductor-solution interface. These models have also been used to simulate photocurrent – potential for a variety of semiconductors including GaP, $CuInSe_2$, WO_3 and GaAs [2-6]. These models predict J-V behavior within a range of applied potential.

Cu_2ZnSnS_4 (CZTS), a p-type absorber material, has recently received considerable attention due to its desirable fundamental energy band gap ~ 1.5 eV and high absorption coefficient ~10^4 cm^{-1} [7-11]. Power conversion efficiency of ~ 9.3% reported by Mitzi et al. [12] indicates that CZTS has sufficient potential as a photovoltaic absorber for next generation environmentally friendly solar cells. Although significant research has been done for CZTS absorber material synthesis and optoelectronic properties, we are not aware of literature that discusses simplistic modeling and evaluation within a wide range of J-V behavior for CZTS based absorber material under illumination in a solution environment. In view of these research literature needs, aspects of photostimulated interfacial charge transfer phenomena have been investigated for CZTS based photovoltaic materials.

8.2. Experimental details

Thin CZTS precursor films were electrochemically grown on a conducting substrate using a bath containing ions of interest (Cu^{2+}, Zn^{2+}, and Sn^{2+}). Sequential electroplating was done by using 3-electrode cell connected to Gamry Instruments Reference 600 potentiostat operated by virtual front panel software. The electrodepositions were carried out at ~ -1.6 V for all the elements. Precursor's film was annealed in evaporated sulfur environment to get CZTS thin film. Sulfurization was carried out in a tube furnace, in an argon environment. CZTS films were evaluated by X-ray diffraction, Raman and

inductively coupled plasma optical emission spectroscopy to verify the phase and purity. More details about experiments and characterization results can be found in earlier reports [7-11]. The thickness of film was ~ 1.5 μm after sulfurization. Accurate photoelectrochemical characterization requires that the redox potential (of electrolyte) should be such that no degradation of semiconductor occurs during J-V measurements and that the potential should be within the band gap. A Eu^{3+}/ Eu^{2+} redox couple meets these criteria, and hence it was chosen for photoelectrochemical characterization of annealed CZTS films [10, 14]. The Eu^{3+}/ Eu^{2+} redox potential vs. Ag/AgCl is -0.58 V [15]. A three electrode system containing Platinum counter, saturated calomel (reference), and CZTS coated on fluorinated tin oxide substrate was used. The area of working electrode (exposed to electrolyte/area illuminated) was ~ 1 cm^2. A schematic diagram of experimental setup is shown in Figure 8.1. J-V curves were recorded (during LED illumination (λ~ 600 nm)) by a Gamry Instruments Reference 600 potentiostat using virtual front panel software. The scan rate was ~ 10 mV/second. The cathodic photocurrent response validates p-type photo-activity of the annealed CZTS films. In the present study only the first half sweep of the voltammogram was considered for modeling. Intensity measurements were carried out by Nova Ophir power meter. All experiments were run at three different incident light intensity levels. Intensity variation was done by changing distance between light source and working electrode.

8.3. Theory

When a semiconductor is kept in an electrolyte solution, the main regions of interest are the field free region, the depletion region (in semiconductor side), regions of

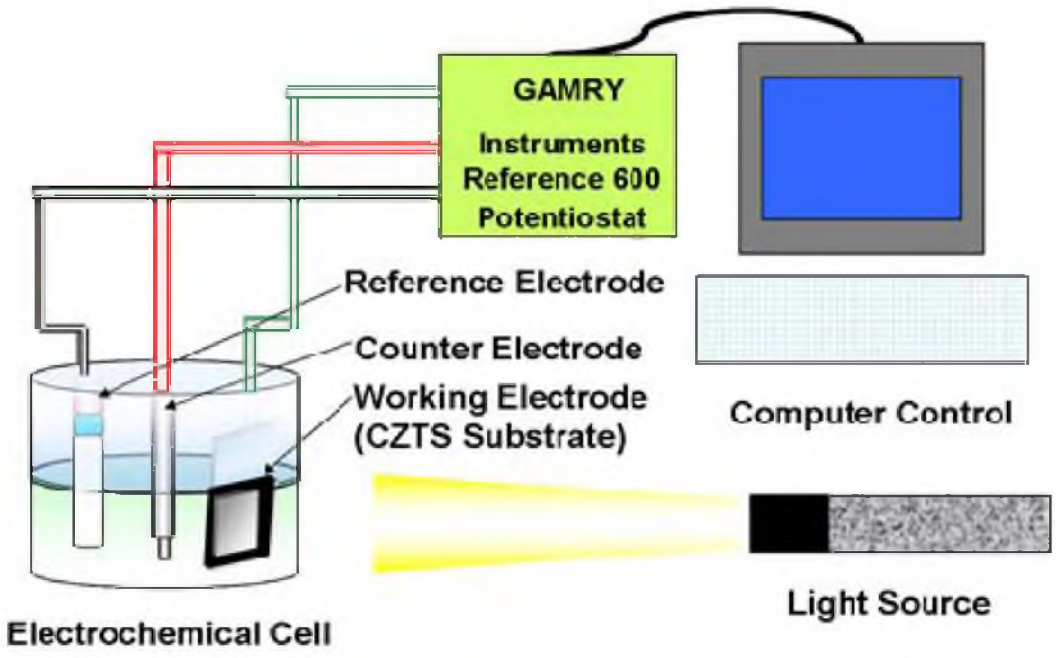

Fig 8.1: A schematic diagram showing photoelectrochemical current measurement setup.

specifically absorbed ions, and the acceptor ions in the outer Helmoltz plane of the double layer [1-6]. During illumination, the absorption of photons results in formation of electron-hole pairs [4]. The resulting increase of majority carriers is negligibly small in comparison with the number of carriers present due to doping. In contrast, the minority carrier's density is generally higher during illumination than that without illumination [4]. Illumination generated minority carriers, within the space charge region are electric field driven. These carriers move toward the interface and are transferred across the interface. This phenomenon accounts for photocurrent generation. It is important to note that photo-electrochemical transfer of electrons at the p-type semiconductor solution interface involves transition through interfacial barriers to accepter states in solution [4, 5]. The

model described by Khan *et al.* explains photoelectrochemical kinetics of p-type semiconducting material under certain assumptions, such as sufficiently large surface state concentration, uniform doping concentration, and classical depletion [4]. The thermal population of electrons was negligible compared to photo-excited electrons. The transport equation at any position '*x*' in the field free region can be written as [2-6]:

$$D_{(e)}\frac{d^2n}{dx^2} + I_a \exp(-\alpha x) - \frac{n_2(x)}{\tau} = 0 \tag{8-1}$$

where $D_{(e)}$ is the diffusion coefficient of electrons, $n_2(x)$ is concentration of electrons in the field free region, I_a is intensity of incident photons, α is the photon absorption coefficient, and τ is the life time of the electron. The first term is related to partial derivative of charge carrier diffusion flux while second term and third term in equation represents photogeneration rate and recombination rate of minority carriers, respectively.

The solution of this equation (1) for *n* under appropriate boundary conditions can be written as [4]:

$$n_1(0) = \frac{1}{(k_{ct} + k_{sr} + k_{br})} \times \left(1 - \frac{e^{-\alpha W}}{(1+\alpha L_D)(1+L_D^{-1}G_1(W))} - \frac{G_2(W)}{L_D + G_1(W)}\right) \tag{8-2}$$

The photocurrent can be expressed as [4]:

$$i_P = AIk_{ct}n_1(0) \tag{8-3}$$

where $n_1(0)$ is the concentration of photoelectrons in the surface region of the semiconductor (under condition of unit incident intensity and without reflection loss), I is incident light intensity in W/cm^2, k_{br} is the recombination rate constant (cm s^{-1}), k_{ct} is the heterogeneous charge transfer rate constant (cm s^{-1}), k_{sr} is the surface recombination rate constant (cm s^{-1}). L_D is the diffusion length for electrons in cm. 'A' is a constant, which is related to normalized incident power input, electronic charge, and reflection and intensity loss of photons during travel inside the solution. For working illuminated electrode of unit area, photocurrent (i) = photocurrent density (j). The other constants in equation (2) are:

$$G_1(W) = (\pi K_B T / 4e_0 V_s)^{1/2} W \tag{8-4}$$

$$G_2(W) = G_1(W) e^{-\alpha W} \tag{8-5}$$

$$k_{br} = D_e e^{-e_0 Vs/kT} / \left(L_D + G_1(w)\right) \tag{8-6}$$

where 'W' is width of the depletion region; V_s is the potential drop inside the semiconductor ($V_s = V\text{-}V_{fb}$); V_{fb} is the flat band potential of the semiconductor. The width of the depletion region was calculated from the relation [4-15]:

$$W = \sqrt{2\varepsilon_s \varepsilon_0 \, |V_S| / e_0 N} \tag{8-7}$$

N is the carrier concentration for a p-type semiconductor; V is the applied potential (biased voltage), ε_s is the dielectric constant of the semiconductor, ε_o is the permittivity of free space, and e_0 is the electronic charge.

8.4. Results and discussion

Various constants and parameters are either calculated or obtained from appropriate literature to simulate the J-V relationship. The value of N was calculated from Mott-Schottky analysis. The flat band potential, which is related to the position of the valence and the conduction band edges of a semiconductor (CZTS in this case), was obtained by measuring the current capacity of the CZTS-electrolyte junction as a function of applied potential.

The CZTS substrate is subjected to a reverse bias and dipped in a solution of Eu^{3+}/ Eu^{2+} during measurements. A Mott-Schottky plot ($1/C^2$ vs. E) was obtained using a Gamry EIS300 with Echem Analyst™. The following relationship was used to obtain N and V_{fb} [8]:

$$\frac{1}{C_{sc}^2} = \frac{2}{e\varepsilon_s\varepsilon_0 N}\left[(V - V_{fb}) - \frac{K_B T}{e}\right] \tag{8-8}$$

where C_{sc} is capacitance of the space charge region, and K_B is Boltzmann's constant. The carrier concentration was calculated from the slope, and the flat band potential was determined by extrapolation to $1/C^2 = 0$ in the Mott-Schottky plot.

The value of 6.7 for ε_s was chosen for CZTS film [16]. All experiments were conducted at room temperature (T = 298 K). The obtained carrier concentration was ~ 10^{17} cm^{-3}. A sensitivity analysis was also carried out during fitting, which reveals that the obtained value N, and the value from literature [17] (V_s = 0.50 V), give a very good fit to experimental data. A fitting using literature values ($N = 2.8\times10^{16}$ cm^{-3} in literature [15]

and using equation (15)) also gives good results (R^2 value ~ 0.99), but with some change in a fitting parameter ($k_{sr} = 4.9\times10^3$ cm s^{-1}) needed.

Another important quantity, which is required to determine photocurrent, is absorption coefficient. It can be calculated using the following equation [8]:

$$\alpha = P(h\nu - E_g)^{1/2} \tag{8-9}$$

where 'P' is constant, E_g is energy band gap, and $h\nu$ is the incident photon energy. The average absorption coefficient of CZTS film from 400 to 700 nm was ~ 3×10^4 cm^{-1}, which is close to the reported value of ~ 10^4 [9,13].

The following equation was used to calculate the electron diffusion length:

$$L_D = (D_e \tau)^{1/2} \tag{8-10}$$

The value of electron diffusion coefficient depends on mobility and is determined based on the Einstein relationship:

$$\mu = \frac{eD_e}{K_B T} \tag{8-11}$$

The resulting value of diffusion length was ~ 0.0000519 cm (for μ = 100 $cm^2s^{-1}V^{-1}$). The value of the electron diffusion coefficient was calculated using the electron mobility value for structurally similar photovoltaic materials such as copper indium gallium selenide (CIGS). The chosen value of electron life time in CIGS was 10^{-9} sec [18]. The recombination rate constant was calculated from the previous information. The chosen value of surface recombination rate constant was ~ 5×10^3 cm s^{-1}, which is close to the

reported value by Khan *et al.* for GaAs [4]. The value of charge transfer rate constant k_{ct} depends on electrode potential and other parameters including electron affinity of the semiconductor, and ground state energy of acceptor ion [4]. However, for this study and simplicity the relation used by Khan *et al.* [4] was adopted. The logarithmic relationship between k_{ct} and electrode potential can be expressed as [4]:

$$k_{ct} = 10^{(-3.3198\times(\text{Electrode potential in Volts})-1.555)} \tag{8-12}$$

After knowing all terms in equations 1 and 2 (expressed in equations 3-12), photocurrent was calculated as a function of electrode potential. Figure 8.2 shows theoretical and experimental plots of photocurrent as a function of electrode potential. A very good fit can be seen in the 3rd quadrant of the J-V region (Potential < 0.2 V). The values of fitting parameters and constants are summarized in Table 8.1. However, when the measured electrode potential exceeds 0.15 V the fit of data is not as good. It can be seen that in equation (2) the dark current due to charge carriers, opposite to the direction of photocurrent, was not considered [6]. An analysis was done using equation (3) with additional contribution from the dark current. The dark current can be expressed as [6]:

$$J_{dark} = J^0(e^{e_0V/K_BTA_0} - 1) \tag{8-13}$$

$$j_P(withdark) = j_P + J_{dark} \tag{8-14}$$

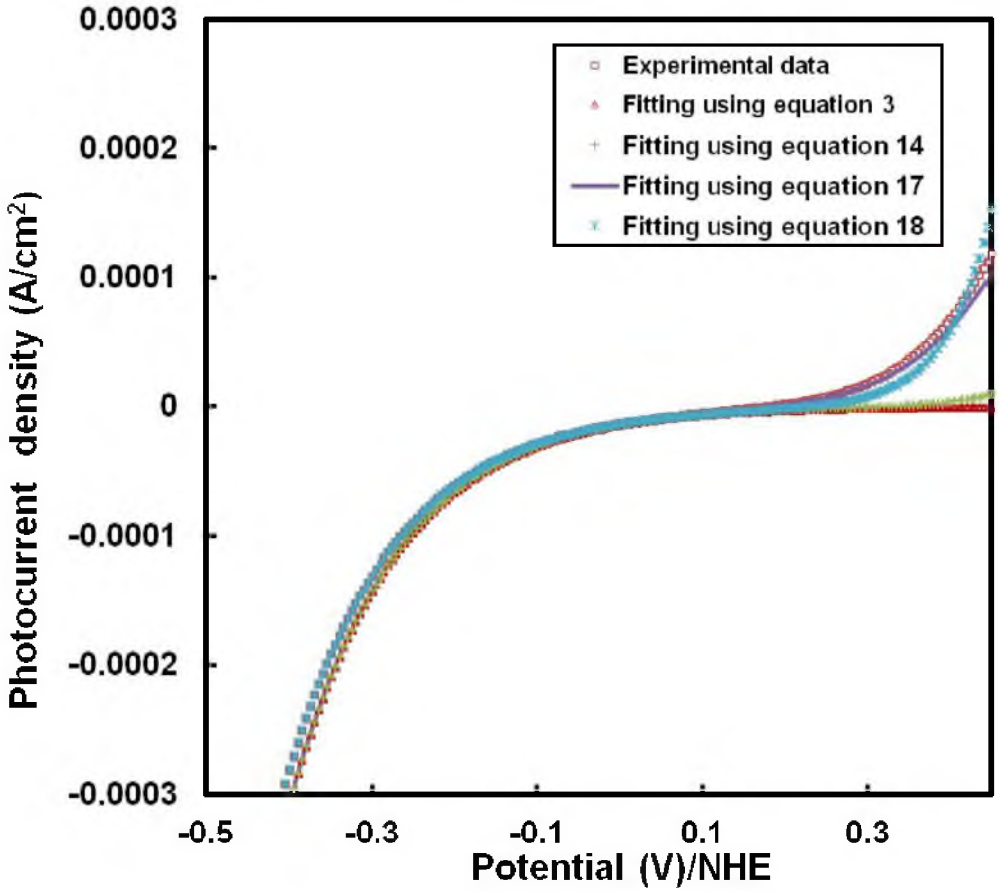

Figure 8.2: Experimental and simulated J-V curves (using equation 3, 14, 17, and 18).

Table 8.1 List of various constants and fitting parameters

Parameter	Value	Value from literature	Reference
α	3×10^{4} cm^{-1}	10^{4}	[9], [10]
L_D	8.89×10^{-5} cm	2.8×10^{-4} cm	[4]
K_{sr}	5×10^{3}cm s^{-1}	10^{4}cm s^{-1}	[4]
A_0	2	2.43	[6]
J_0	1×10^{-5} mA/cm^2	1.33×10^{-5} mA/cm^2	[6]
B	3.51×10^{-7}	10.38×10^{-5}	
m	2	1-2	[21]
A	1120		
J_S^*	3.6542×10^{-8} A/cm^2		
V_s	0.5 V	0.5 V	[13], [15]
εs	6.7	6.7	[16]
V_{fb}	0.2 V	0.2 V	[13], [15]

where J^0 is majority carrier dark saturation current (depends on temperature, energy gap and carrier concentration), and A_0 is the junction perfection factor. The equation and concept, closely matches with the discussion by Memming *et al.* [19, 20]. According to their assumption, transient behavior of n –type GaAs is comparable with p-type GaAs under specific condition. Analogous to the n-type electrode behavior, J-V behavior of p-type electrode in dark environment was examined, which is related to the quasi-Fermi level of charge carriers. The value of A_0 was chosen to be 2.42 and J^0 was selected as 1×10^{-5} mA/cm^2 for fitting purposes. The values of fitting parameters (at constant temperature) are close to the values (A_0 =2, J^0=1.33×10^{-5} mA/cm^2) chosen by Chandra *et al.* for n-GaAs [6]. After considering the dark current contribution to the total photocurrent, it can be seen (Figure 8.2) that fitting improves (R^2 (without dark current) = 0.968; R^2 (with dark current) = 0.974); however, the actual J-V curve differs from the theoretical fit based on equation (14).

Another contribution, space – charge recombination, was not considered in equation (14). This contribution is considered to be important and was included by the authors to improve fitting relative to traditional modeling that neglects this contribution for p-type material. This contribution can be obtained from the Shockley-Sah-Noyce method [21]. The expression for space charge recombination is [6]:

$$J_{SCR} = B\sqrt{|(V_{fb}-V)|}e^{qV/2K_BT} \qquad (8\text{-}15)$$

where B is a recombination constant. The value of 'B' depends on various factors including carrier thermal velocity, density of traps and capture cross section [6]. The best value of 'B' obtained from fitting is ~ 3.5×10^{-7}. The resulting photocurrent equation

proposed in this study, which considers dark current and space charge recombination current, is:

$$j_P(effective) = Ae_0 k_{ct} n_1(0) + J_{dark} + J_{SCR} \tag{8-16}$$

Or, after additional substitution of equation (13) and (15), is:

$$j_P(effective) = Ae_0 k_{ct} n_1(0) + J^0(e^{qV/K_B T A_0} - 1) + B\sqrt{|(V_{fb} - V)|}e^{qV/2K_B T} \tag{8-17}$$

A more simplified version of this equation can be written as:

$$j_P(effective) = Ae_0 k_{ct} n_1(0) + J_S^*(e^{qV/mK_B T}) \tag{8-18}$$

where J_s^* is saturated current derived from the Shockley equation [21-23], and *m* is a factor whose value depends on effective contribution of diffusion or recombination current to the total forward current. It can be seen (Figure 8.2) that fitting using equation (17) and (18) matches with experimental data (obtained at incident intensity ~ 0.22 mW/cm^2) reasonably well, over the entire potential range evaluated. The R^2 value for fitting using equation (17) is ~ 0.99 whereas fitting using equation (18) gives R^2 ~ 0.987. A regression analysis was also done using data of positive photocurrent and experimental value (excluding rest of data point), which reveals that no significant correlation in case of equation 3 while good fit (R^2 ~ 0.978) was observed using equation 17. Other details of fitting parameters are listed in Table 8.1. Further analysis was carried out by plotting a graph of equation (17) at different incident intensity levels as shown in Figure 8.3. It can be seen in Figure 8.3 that a theoretical J-V curves show increased photocurrent response

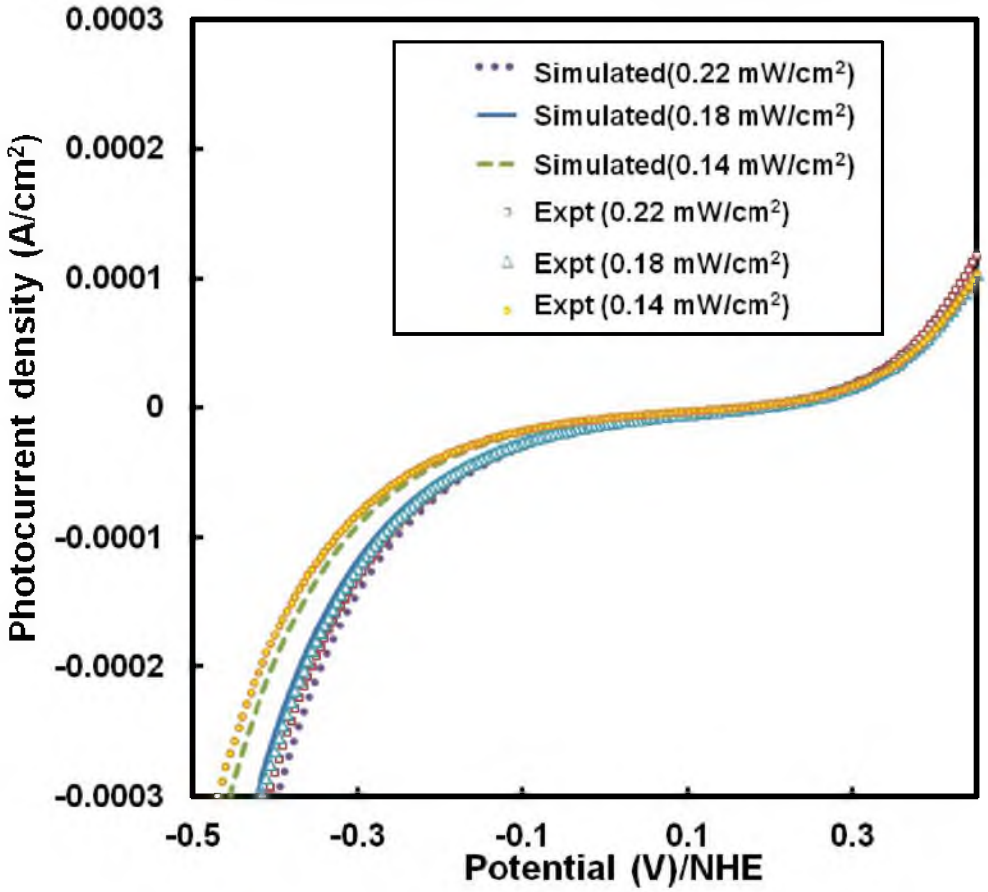

Figure 8.3: Experimental and simulated J-V curves drawn using equation 17 at different intensity levels.

when incident light intensity increases in negative biased regions. However, in positive biased regions ($V>V_{cutoff}$) no significant change in photocurrent was observed as predicted by equation (17). This trend is also followed by an experimental J-V curve, (Figure 8.3) where it can be seen that the experimental J-V curve matches well with the simulated J-V curve.

Other important parameters in this modeling are the diffusion coefficient (D_e), surface recombination rate constant (k_{sr}) and absorption coefficient (α). The theoretical current versus diffusion length curve (Fig. 8.4) has been drawn using equation (17) at different biased potentials. If mobility is assumed constant, diffusion length will be proportional to temperature. From equation 11, it is obvious that diffusion length increases with increase of D_e. It can be seen that increased photocurrent response is observed with increase of diffusion length and saturates at a certain value of diffusion length. This observation closely matches with results of Khan *et al.* [4], which showed that photocurrent exhibits a limiting behavior after a certain diffusion length is reached. Simulated photoactivity at different absorption coefficients is shown in Fig. 8.5. Reduced photocurrent response is shown when the absorption coefficient value is reduced. No significant effect of a variable absorption coefficient is observed with biased potentials where dark current is dominant. This observation can be useful for modeling J-V relationships of other photovoltaic materials with different absorption coefficients.

A very sensitive parameter, surface recombination rate constant (k_{sr}) is also examined. As can be seen in Figure 8.6, significant reduction in photocurrent is observed when the value is replaced with half of its original value. In other words, the surface

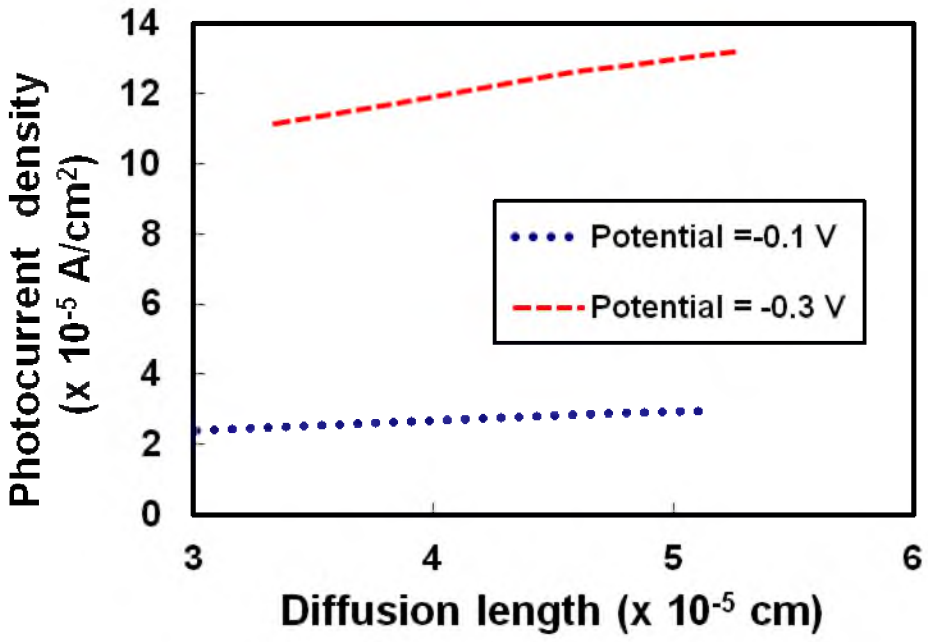

Figure 8.4: Diffusion length vs. Photocurrent.

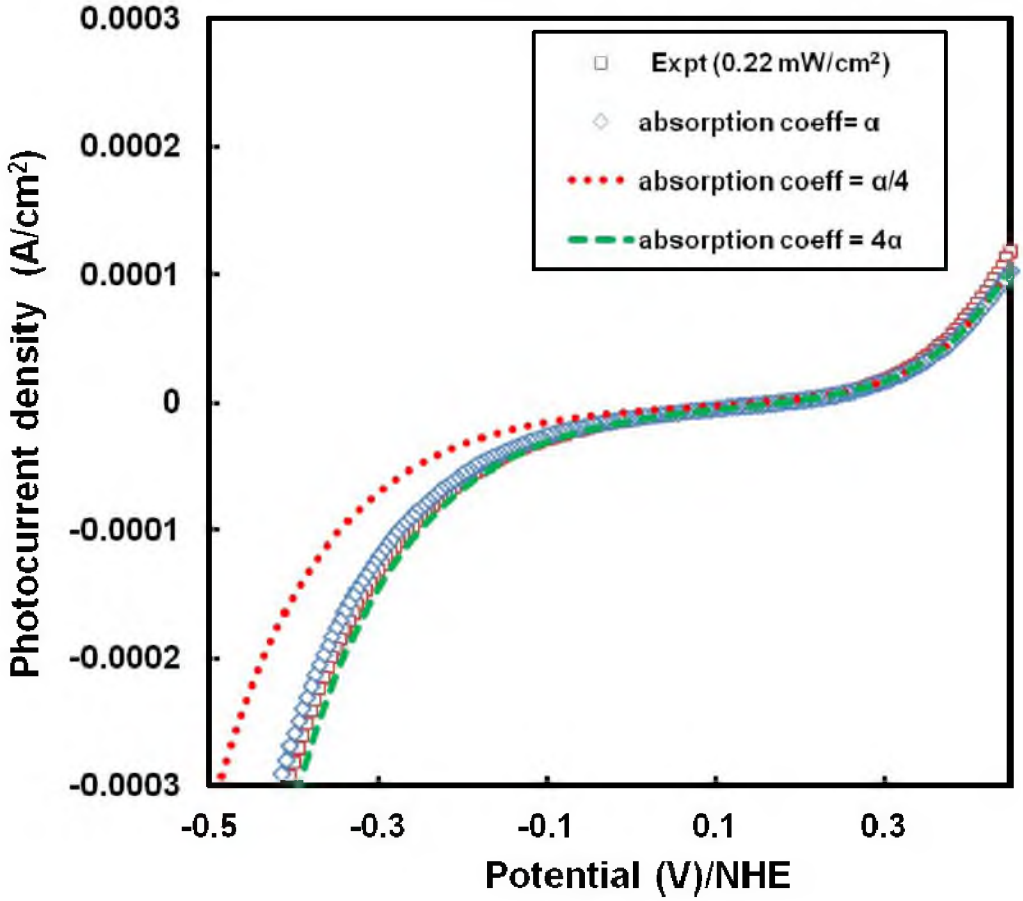

Figure 8.5: Experimental and simulated J-V curves drawn using equation 17 at different absorption coefficient.

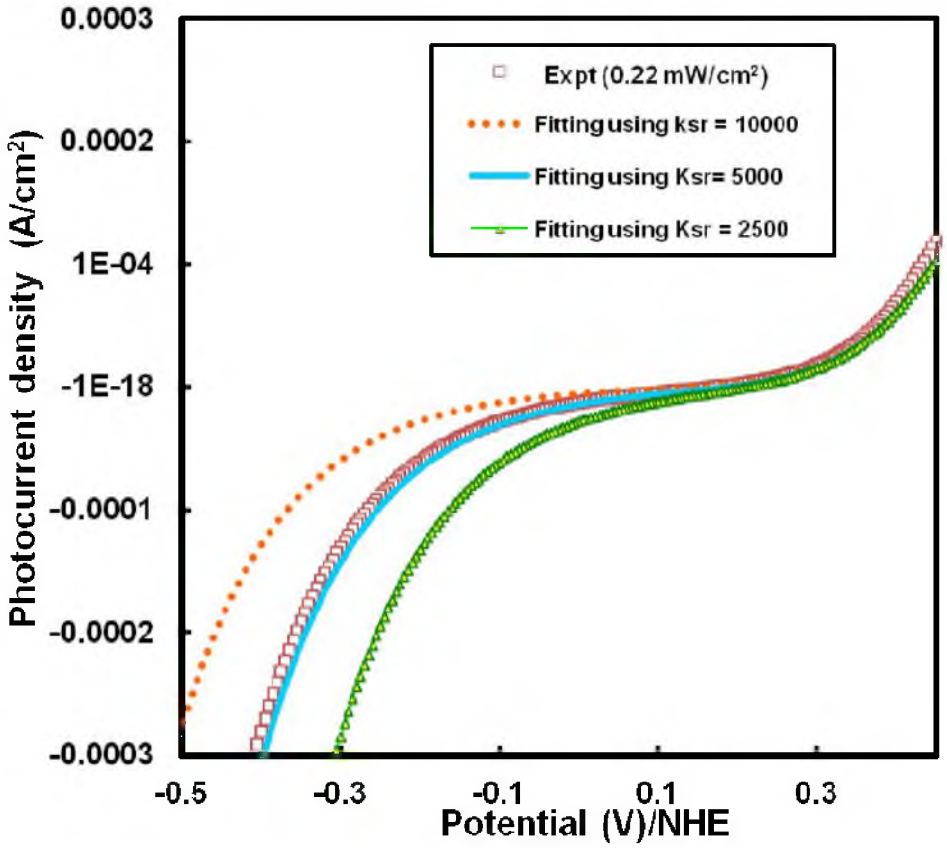

Figure 8.6: Experimental and simulated J-V curves drawn using equation 17 at different value of ksr.

recombination phenomenon is a very important property which also governs photoactivity of CZTS absorbers along with other important factors.

Overall, these analyses validate the contribution of distributed electronic states in electrolyte for CZTS absorbers. This model also indicates the presence of surface states at CZTS-electrolyte interface, which is related with the charge transfer process of ions from electrolyte. It can also be anticipated that identical J-V behavior will be observed when other electrolytes whose redox potential is close to Eu^{3+}, such as Cr^{3+} (E^0_{redox} = -0.67 V(SCE)), are used. It is also important to note that various fitting parameters and constants (listed in Table 1) utilized in this analysis are close to the known value for other absorber materials obtained from existing theories and research.

Although the proposed model explains photovoltaic activity for CZTS absorber material for a broad range of potential, certain phenomena such as inelastic charge transfer via surface states, Fermi level pinning, and wavelength dependence of photocurrent were not examined in this study. The proposed modified Gärtner model explains photoactivity for the first half sweep of a voltammogram. Multiple cathodic and anodic sweeps cause some hysteresis, which is possibly due to oxidation/reduction of some species and band edge shift at the electrolyte-semiconductor junction. Treatment of p-type electrode, which is related to surface condition and film quality, is also very important [19, 20]. An epitaxially grown film J-V behavior may differ from film grown by solution based method used in this study.

8.5. Conclusions

The experimental investigation of the J-V characteristics of illuminated CZTS-electrolyte junctions was carried out at different illumination levels. A modified theoretical model to explain J-V characteristics for CZTS-Electrolyte solution has been proposed. The proposed model, which is modified form of Gärtner model, considers that the photo-electrochemical transfer of electron at CZTS-electrolyte solution interface is mainly due to a transition through interfacial barriers to acceptor states in solution. Consideration of dark current in the positive bias region and the space charge recombination phenomenon improves fitting. Simulated J-V behavior at different intensity levels also matches well with experimental observation.

8.6 References

[1] M. Grätzel, Nature 414 (2001) 338.

[2] M. A. Butler, J. Appl. Phys. 48 (1977)1914.

[3] W. W. Gärtner, Phys. Rev. 116 (1959)84.

[4] S. Khan and J. Bockris, J. Phys. Chem 88 (1984) 2504.

[5] C. Guillen, J. Herrero, and D. Lincot, J. Appl. Phys. 76 (1994)359.

[6] S. Chandra, S. L. Singh, and N Khare, J. Appl. Phys. 59 (1985) 1570.

[7] P. K. Sarswat, M. L. Free, A. Tiwari, in: Joseph J. Berry, Elvira Fortunato, Julia E. Medvedeva, Yuzo Shigesato (Eds.), Transparent Conducting Oxides and Applications, Boston, U.S.A., November 28-December 02, 2010, Materials Research Society Symposium Proceedings 1315 (2011) mm 07.

[8] P. K. Sarswat, M. L. Free, A. Tiwari, in: Lukas Schmidt-Mende, Henry J. Snaith, Gregory L. Whiting, David S. Ginger (Eds.), Novel Fabrication Methods for Electronic Devices, Boston, U.S.A., November 28-December 02, 2010, Materials Research Society Symposium Proceedings 1288 (2011) g06.

[9] P.K. Sarswat, M.L. Free, and A. Tiwari, Phys. Status Solidi B 248 (2011) 2170.

[10] P. K. Sarswat and M L Free, Phys. Status Solidi A 208 (2011) 2861.

[11] P. K. Sarswat, M. L. Free, A.Tiwari, M. Snure, CZTS thin films on transparent conducting electrodes by electrochemical technique, Thin Solid Films 2011, doi: 10.1016/j.tsf.2011.07.052

[12] T. K. Todorov, K. B. Reuter, and D. B. Mitzi, Adv. Mater. 22 (2010) E156.

[13] H. Araki, Y. Kubo, A. Mikaduki, K. Jimbo, W. S. Maw, H. Katagiri, M. Yamazaki, K.Oishi, and A. Takeuchi, Sol. Energy Mater. Sol. Cells 93 (2009) 996.

[14] R. Memming, J. Electrochem. Soc. 125 (1978) 117.

[15] J. J. Scragg, P. J. Dale, L. M. Peter, G. Zoppi, and I. Forbes, Phys. Status Solidi B 245 (2008) 1772.

[16] Clas Persson, J. Appl. Phys. 107 (2010) 053710.

[17] J. J. Scragg, P. J. Dale, and L. M. Peter, Electrochem. Commun. 10 (2008) 639.

[18] I.L. Repins, W.K. Metzger, C.L. Perkins, J.V. Li, and M.A. Contreras, "Measured Minority-Carrier Lifetime and CIGS Device Performance," IEEE Photovoltaics Specialists Conference, 34, 2009.

[19] R. Reineke and R. Memming, J. Phys. Chem.96 (1992)1317.

[20] R. Memming, Semiconductor Electrochemistry, 1st ed., (Wiley, Weinheim, 2001).

[21] C. Sah, R. Noyce, and W. Shockley, Proc. Institute of Radio Engineers 45 (1957) 1228.

[22] W. Shockley, Bell Syst. Tech. J. 28 (1949) 435.

[23] S. M. Sze, Physics of Semiconductor Devices, 3rd ed., (Wiley, New York 2006). pp-63-129.

CHAPTER 9

TEMPERATURE-DEPENDENT STUDY OF RAMAN A MODE OF Cu_2ZnSnS_4 THIN FILMS

9.1 Introduction

This temperature-dependent Raman study of kesterite phase Cu_2ZnSnS_4 (CZTS) thin film was performed over the temperature range 98–378 K. A detailed qualitative analysis showed that the Raman data for the "A" mode of vibration, the strongest peak for kesterite CZTS films, fit very well to a damped harmonic oscillator (DHO) model. This investigation of temperature-dependent Raman data shows that the observed frequency shift is due to the cumulative effect of thermal expansion and anharmonicity resulting from a 4-phonon damping process. The temperature dependence of linewidth is also consistent with the above analysis.

CZTS crystallizes mainly in kesterite and stannite-type structures, in which kesterite is thermodynamically the most favorable phase [1-5]. However, it is very difficult to distinguish between kesterite and stannite phases as their X-ray diffraction (XRD) patterns are similar. The only difference in their XRD diffractogram is a slight difference in peak intensity ratio I (211)/I (202), which is slightly larger for kesterite [3–5].

Although there are different opinions about CZTS crystal structure, some of the recent literature suggests that "CZTS as kesterite" is an appropriate assumption [2–8]. In this work, analyses are done assuming CZTS as kesterite.

Raman spectroscopy is a potential technique that can distinguish the stannite or kesterite phases from other secondary phases with similar crystal structures that are formed during CZTS synthesis [9–12]. The technique provides information regarding optical modes of vibrations due to inelastic scattering of light. The change of frequency and line width of phonon with respect to temperature can provide further valuable insights regarding anharmonicity of vibration. Temperature-dependent Raman investigations have already been reported for various photovoltaic-semiconducting materials including copper indium selenide (CIS) thin films, compounds with wurtzite-type structure, gallium arsenide, and silicon [6–15]. Temperature-dependent Raman study is still a relatively unexplored area for CZTS. In this chapter, results and analysis on the Raman spectroscopy of kesterite phase CZTS, performed over the temperature range 100–378^{o}K, are reported.

9.2. CZTS crystal structure and Raman mode

Copper zinc tin sulfide crystallizes in three phases, namely, kesterite (space group $I\bar{4}$), stannite (space group $I\bar{4}2m$) and the primitive mixed CA structure (PMCA) (space group $P\bar{4}2m$) [1]. Of these three phases, kesterite and stannite are most widely studied. The kesterite consists of a ccp array of sulfur atoms, with metal atoms occupying one half of the tetrahedral voids. Crystallization of stannite-type compounds occurs in the tetragonal space group $I\bar{4}2m$ (D_{2d}^{11}) with two formula units in each unit cell.

Based on the Wyckoff position of an atom in a unit cell, the group analysis of stannite type structure with (K= 0) is [3, 9, 10]:

$$\Gamma = 2A_1 + A_2 + 2B_1 + 4B_2 + 6E \quad (9\text{-}1)$$

Out of these B_2 and E modes are IR active while A_1, B_1, B_2, and E are Raman-active vibrations [9, 10]. The Raman spectrum for stannite structure shows an intense peak, assigned to species A_1. The A_1 peak is observed at frequency 336cm^{-1}[9]. Unlike the stannite phase, no information about the group analysis for the kesterite phase is available in the literature. In this study a group analysis for kesterite phase using the Bilbao Crystallographic server was performed [10]. The result of the kesterite group analysis is [3, 10]:

$$\Gamma_{Raman} = 3A + 6B + 6E_1 + 6E_2 \quad (9\text{-}2)$$

Here, B, E_1, and E_2 modes are IR-active, while A, B, E_1, and E_2 modes are Raman-active modes. It is evident from group analysis that the only entirely symmetric vibrations correspond to "A" mode and therefore is expected to result in the strongest line for the kesterite phase of CZTS [9, 10]

9.3 Experiments

Copper zinc tin sulfide thin-film grown on transparent conducting oxide was prepared using an electrodeposition technique followed by an annealing step. Electrodeposition was carried out in the potentiostatic mode using an electrolyte containing copper (II) sulfate pentahydrate, zinc chloride, and sodium stannate along with a suitable complexing agent. Fluorinated tin oxide (FTO) coated glass (area ~1.5–2.0 cm^2) was used as the substrate. Electrodeposited films were annealed in an argon environment with evaporated elemental sulfur (99.99%) in a tube furnace. Annealing was done at a substrate temperature of 560 °C for 2 h (working pressure ~ 5×10^{-1} mbar).

Thin films were characterized by XRD, scanning electron microscopy (SEM), Raman spectroscopy, and transmission/absorption spectroscopy. XRD scans were run using a Philips X'Pert XRD diffractometer with Cu Kα radiation over the 2θ range 20–80°. Step sizes of 0.005° and a receiving slit size of 1/8° were used in order to achieve high resolution. Raman spectroscopy was carried out using an R 3000 QE Raman spectrometer (made by Raman Systems).

The wavelength of the laser excitation for Raman measurements was 785 nm and the laser power was ~ 90 mW. The spectral range covered in this study extends from 315 to 365 cm^{-1}. All the experiments were performed in the backscattering geometry, focusing on the study of "A" mode vibration. Temperature-sensitive Raman modes of electrochemically grown CZTS film were collected using an indigenous cryostat setup, having capability of measurements from 77 to 500 K. The Raman lines obtained were

calibrated for all experiments. Peak parameters were obtained by least square Lorentzian fitting using Peakfit® software.

9.4. Results and discussion

Figure 9.1 shows a characteristic θ–2θ XRD pattern of a CZTS thin film. This pattern matches very well with the kesterite structure of CZTS (JCPDS card 26-0575). The Raman spectra of CZTS thin film over the wave number range 315–365 cm^{-1} are shown in Figure 9.2. The strongest Raman peak (at room temperature) was found at ~338 cm^{-1}. This peak position matches well with previously published results for kesterite phase of CZTS [9–12]. The non-resonant Raman modes of CZTS were obtained using an appropriate backscattered geometry at various temperatures. The strongest peak at ~338 cm^{-1} assigned as "A" mode, is consistent with earlier reports [11, 12]. A decrease in the frequency and intensity of "A" mode is observed with an increase in temperature. An increase in linewidth/damping is also observed with increase in temperature.

In order to account for the accurate value of the phonon frequency and linewidth of "A" modes at different temperatures, the damped harmonic oscillator (DHO model) to fit the Raman profile (see Figure 9.3) was used. All spectra were fitted by means of linear combination of DHOs with a background term. Baseline correction was done based on the method described by Schrader [16]. Two-point and common tangent baseline methods were adopted for analysis. The intensity of Raman peaks at absolute zero temperature follows the expression [5-23]:

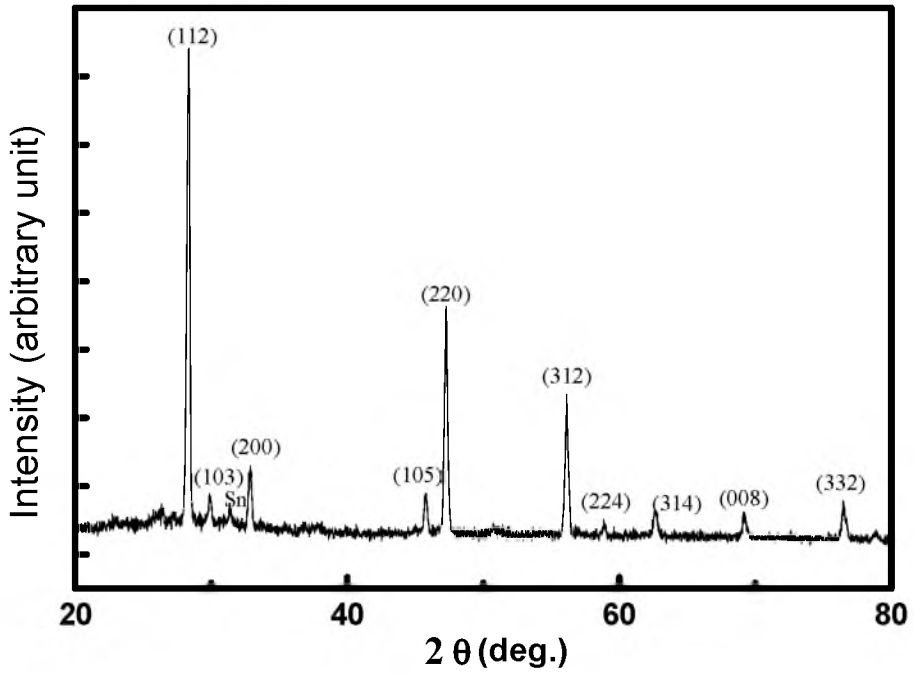

Figure 9.1: X ray diffraction (XRD) pattern of CZTS thin film.

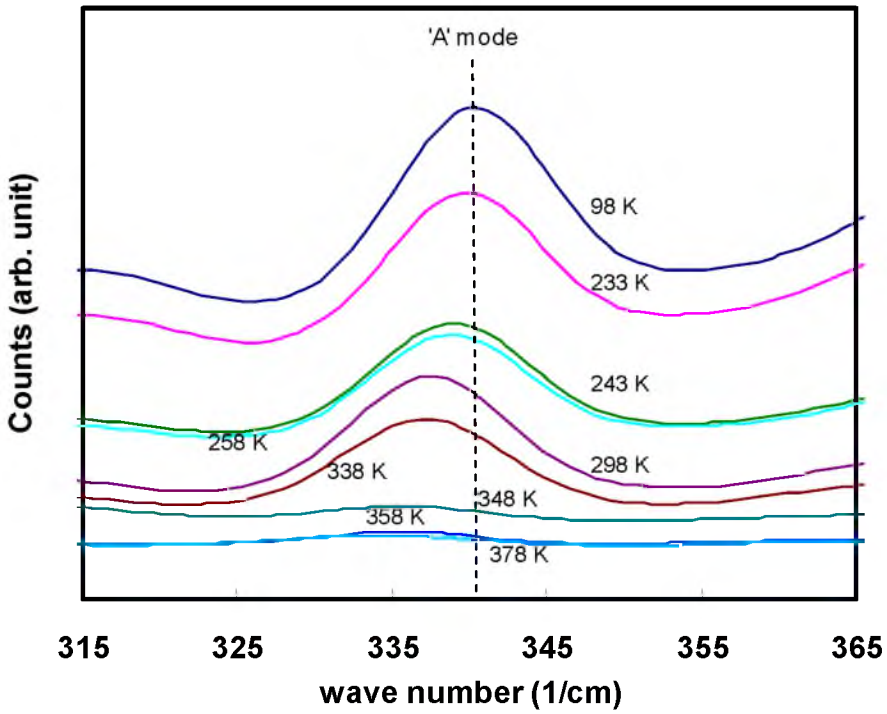

Figure 9.2: Raman spectra for CZTS thin film recorded at various temperatures.

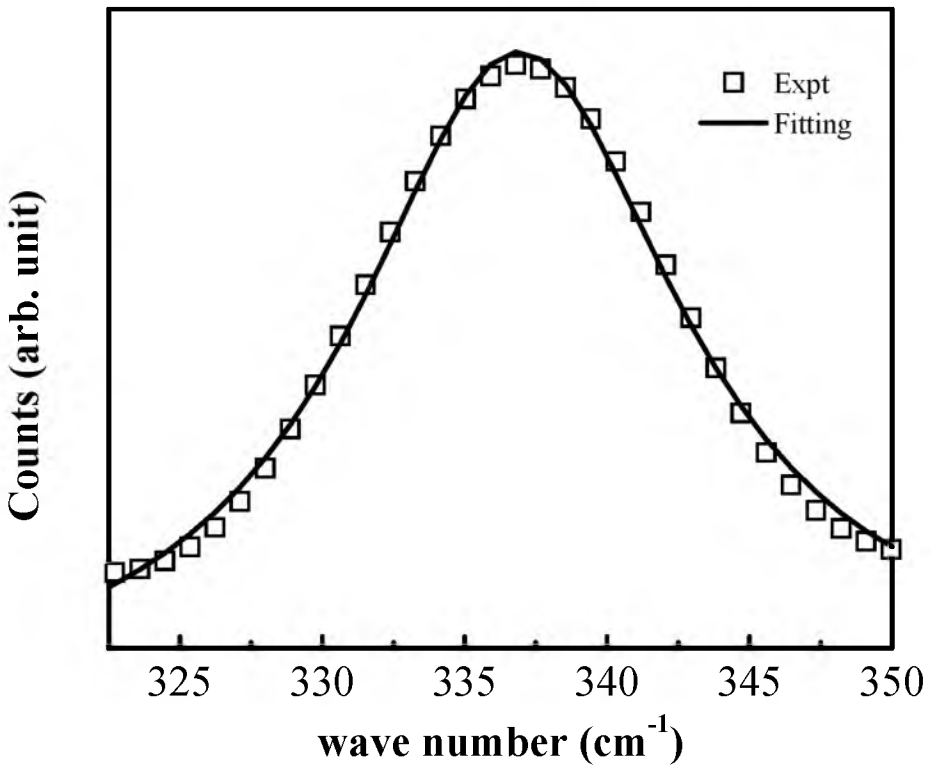

Figure 9.3: Room-temperature Raman spectrum of CZTS thin film and theoretical fitting using damped harmonic oscillator (DHO) model.

$$I(w) = I_{BKG}(w) + \frac{A\Gamma^2\omega_P\omega}{(\omega_P^2 - \omega^2) + \Gamma^2\omega^2} \tag{9-3}$$

where $I_{BKG}(\omega)$ is contribution from the background and second term is contribution from phonon peak of wave number ω_P , width Γ, and amplitude A. At finite temperature a temperature dependent term (n + 1) needs to be multiplied to the second term of equation (3), to take care of thermal effects. Where $n = (\exp(\hbar\omega/k_b T) - 1)^{-1}$ is the phonon occupation number. In Figure 9.3 we have shown the fitting of room temperature Raman data to equation (3). A very good fitting can be clearly seen.

9.4.1 Temperature dependence of Raman peak frequency

The variation of peak frequency of the 'A' mode with temperature is shown in Figure 9.4. A continuous decrease in the peak frequency with temperature can be clearly seen. The decrease of the phonon frequency with increase in temperature can be explained by the perturbation model according to which the frequency shift is due to the combined effect of thermal expansion and the anharmonic coupling to other phonon [18, 24]. In this model the temperature dependent Raman frequency shift can be written as:

$$\omega_P(T) = \omega_0 + \Delta\omega_{expansion}(T) + \Delta\omega_d(T) \tag{9-4}$$

where ω_0 is harmonic frequency of optical mode, $\Delta\omega_{expansion}$ (T) is contribution due thermal expansion, $\Delta\omega_d$(T) is contribution due to anharmonic coupling to phonons of other branches.

The value of $\Delta\omega_{expansion}$ (T) depends on mode polarization and thin film composition. Its value can be determined using following expression [18, 24]:

$$\Delta\omega_{expansion}(T) = \omega_0\left[\exp\left[-\gamma\int_0^T[\alpha_c(T) + 2\alpha_a(T)]dT\right] - 1\right] \tag{9-5}$$

where α_c and α_a are parallel and perpendicular expansion coefficient; γ is the Grüneisen parameter for optical Raman mode. For the experimental temperature range [17]: $2\alpha_a \sim \alpha_c$

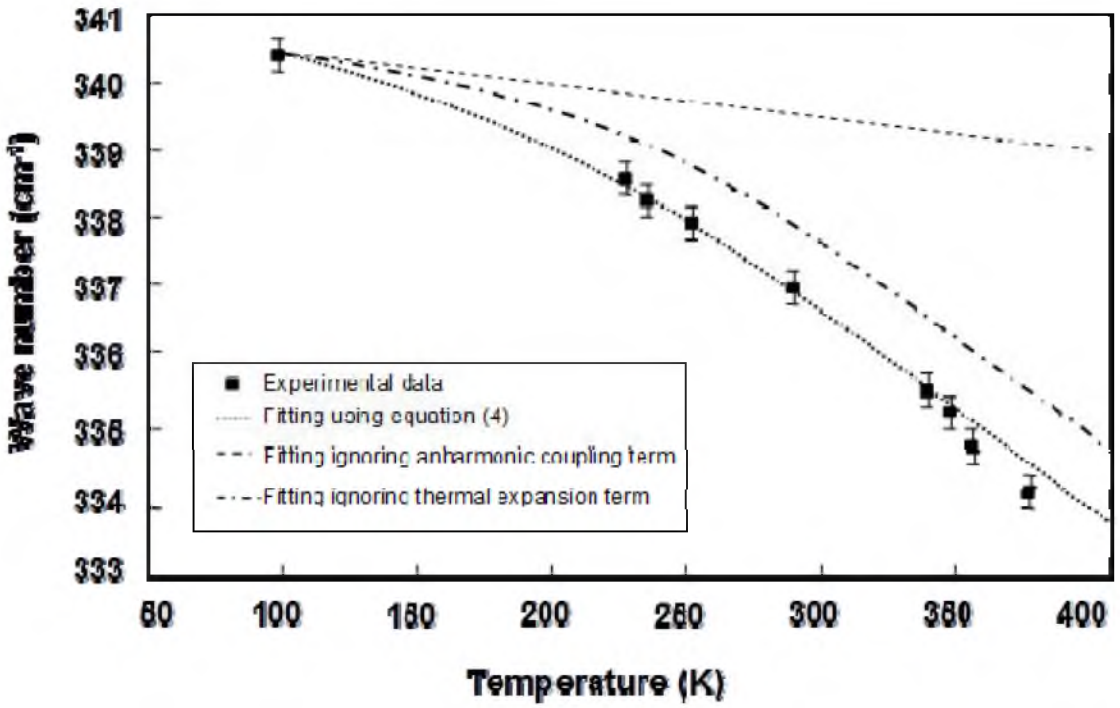

Figure 9.4: The shift in peak frequency versus temperature. Theoretical fitting using quartic process (solid line), and by ignoring (i) the thermal expansion and (ii) the damping term in Eq. (4) are also shown.

Hence equation (5) can be simplified to:

$$\Delta\omega_{\exp ansion}(T) = -\omega_0 \gamma \int_0^T [4\alpha_a(T)]dT \qquad (9\text{-}6)$$

In order to estimate the contribution (to overall frequency shift) due to thermal expansion, the value of (α_a) was taken from the work of Selivanov *et al* [17] and the Grüneisen parameter was assumed to be 1.01. [19, 20]

The contribution from the anharmonic coupling of phonon can be expressed as [22,23]:

$$\Delta\omega_d(T) = A\left[1 + \frac{2}{\exp(\hbar\omega/2k_BT) - 1}\right] + B\left[1 + \frac{3}{\exp(\hbar\omega/3k_BT) - 1} + \frac{3}{\{\exp(\hbar\omega/3k_BT) - 1\}^2}\right]$$

.....(9-7)

where the first term is due to the coupling of optical phonon to two identical phonons (cubic process) and second term is due to the coupling to three identical phonons (quartic process).[18, 23] Here 'A' and 'B' are the weight parameters for cubic process and quartic process, respectively.

In Figure 9.4 we have shown the fitting of experimentally observed Raman frequency shift data to equation (4). For comparison we have also shown the fitting by ignoring the: (i) thermal expansion term and (ii) damping term in equation (4). As can be seen, the experimental data fits very well in equation (4). However, if the thermal expansion term or damping term is ignored, significant deviation is observed. This implies that both the thermal expansion as well as damping term are playing important role in the system. The

values of fitting parameter A, B, and ω_o are found to be -1.0×10^{-22} cm^{-1}, -9.1×10^{-20} cm^{-1} and 340.8 cm^{-1} respectively. Further analysis showed that contribution to $\Delta\omega_d(T)$ coming from the cubic process (first term in equation (7)) is much smaller compared to the contribution from second term. This implies that 4-Phonon (quartic process) is the dominant damping process.

9.4.2 Temperature dependence of linewidth

Analogous to peak frequency shift, linewidth can also be modeled based on work of Klemens [22] and Balkanski *et al.* [23]. According to this, temperature dependent linewidth can be written as:

$$\Gamma(T) = \Gamma_0 + \Delta\Gamma_d(T) \tag{9-8}$$

where Γ_0 is the linewidth at T = 0 K while $\Delta\Gamma_d(T)$ is the linewidth due to the anharmonic coupling. Here it is to be noted that though thermal expansion contributes to shift in peak frequency, it has no effect in linewidth.

Using the approach proposed by Klemens [22], shift in linewidth, due to the anharmonicity can be written as:

$$\Delta\Gamma_d(T) = C\left[1+\frac{2}{\exp(\hbar\omega/k_BT)-1}\right] + D\left[1+\frac{3}{\exp(\hbar\omega/3k_BT)-1}+\frac{3}{\{\exp(\hbar\omega/3k_BT)-1\}^2}\right] \tag{9-9}$$

where first term is due to cubic process while second term is due to quartic process. 'C' and 'D' are constant related to decay process. Fitting was performed by using the

expression for $\Gamma(T)$ as shown in equation (8). In addition to this, we also performed fitting by ignoring the cubic term (dotted line) and by ignoring the quartic term (dash line). Figure 9.5 shows the variation of the linewidth between 98 and 378 K. Fitting of experimentally observed linewidth data to equation (8) is also shown. Based on least square fit analysis, theoretical fit using 3-phonon process demonstrated viability only for short (100 – 250 K) temperature range while the agreement between experimental data points and theoretical fitting is best found for four phonon process for the entire temperature range (100- 350 K). For the best fit, the value of Γ_0, C and D were found to be 10.7 cm^{-1} , 2 $\times 10^{-10}$ cm^{-1} and 1.09 $\times$ 10^{-20} cm^{-1} respectively. Above analysis is very consistent with the conclusion of section 9.4.1, implying the 4-Phonon process as the dominant damping process.

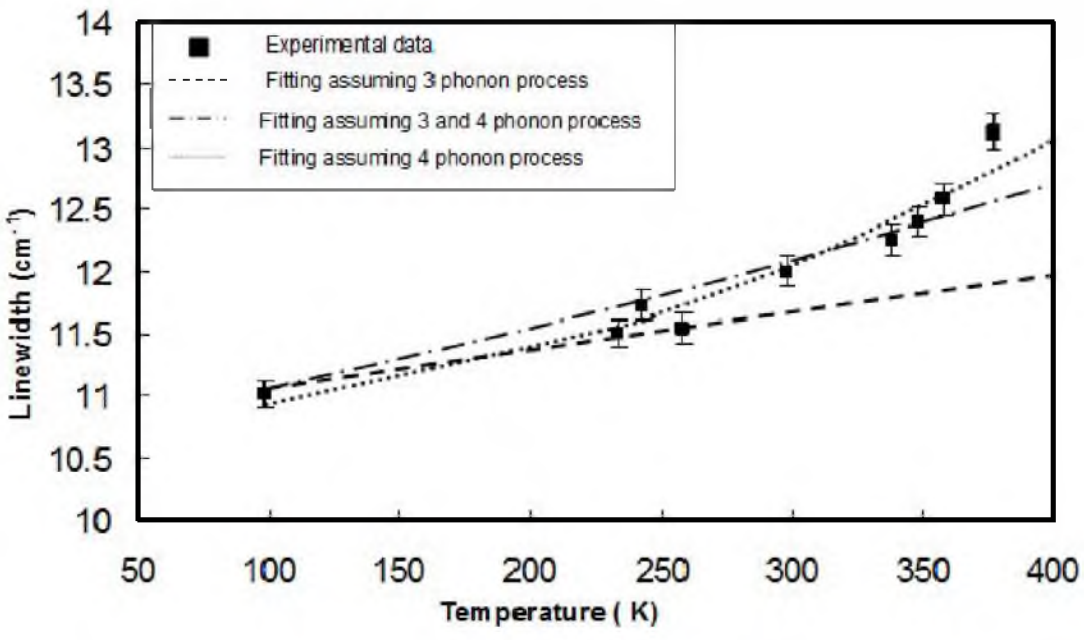

Figure 9.5. The shift in linewidth versus temperature. Theoretical fitting using 3-phonon, 4-phonon, and generalized (3–4-phonon) process is also shown.

9.5. Conclusions

The effect of temperature on the frequency and linewidth of Raman active 'A' mode of kesterite phase CZTS films has been investigated. Detailed quantitative analysis of temperature dependent Raman data showed that the four phonon damping process is the main factor responsible for the observed frequency shift as well as for the linewidth variation.

9.6. References

[1] S. Chen, X. G. Gong, A. Walsh, and S. H. Wei, Appl. Phys. Lett. 94 (2009) 041903.

[2] S. Chen, X. G. Gong, A. Walsh, and S. H. Wei, Appl. Phys. Lett. 96 (2010) 021902.

[3] S. Schorr and G. Gonzalez-Aviles, Phys. Status Solidi A 206 (2009) 1054.

[4] S. Schorr, H. Hoebler, and M. Tovar, Eur. J. Mineral. 19 (2007) 65.

[5] T. Maeda, S. Nakamura, and T. Wada, in: Materials Research Society Symposium Proceedings 1165-M04-03, Strasbourg, France, 2009.

[6] D. Wang, L. Wan, Z. Bai, and Y. Cao, Appl. Phys. Lett. 92 (2008) 211912.

[7] Y. B. Kishore Kumar, G. S. Babu, P. U. Bhaskar, and V. S. Raja, Sol. Energy Mater. Sol. Cells 93(2009) 1230.

[8] T. M. Friedlmeier, H. Dittrich, and H. W. Schock, in: Proceeding of 11th International Conference on Ternary and Multinary Compounds, Salford, 1997, p. 345.

[9] M. Himmrich and H. Haeuseler, Spectrochim. Acta 47A(1991) 933.

[10] M. I. Aroyo, J. M. Perez-Mato, C. Capillas, E. Kroumova, S. Ivantchev, G. Madariaga, A. Kirov, and H. Wondratschek, Z. Kristallogr. 221 (2006) 15.

[11] P. A. Fernandese, P. M. P. Salomé, and A. F. da Cunha, Thin Solid Films 517(2009) 2519.

[12] M. Altosaar, J. Raudoja, K. Timmo, M. Danilson, M. Grossberg, J. Krustok, and E. Mellikov, Phys. Status Solidi A 205 (2008) 167.

[13] G. S. Doerk, C. Carraro, and R. Maboudian, Phys. Rev. B 80 (2009) 073396.

[14] H. F. Liu, N. Xiang, S. Tripathy, and S. J. Chua, Thin Solid Films 515 (2006) 459.

[15] M. S. Liu, L. A. Bursill, S. Prawer, K. W. Nugent, Y. Z. Tong, and G. Y. Zhang, Appl. Phys. Lett. 74 (1999) 3125.

[16] B. Schrader, Infrared and Raman Spectroscopy (VCH Publishers, New York, 1995),

p.414.

[17] E. N. Selivanov, R. I. Gulyaeva, and A. D. Vershinin, Inorg. Mater. 43(2007) 653.

[18] S. Ishizuka, A. Yamada, P. Fons, and S. Niki, J. Renew. Sustain. Energy 1 (2009) 013102.

[19] S. Q. Wang, Appl. Phys. Lett. 88 (2006) 061902.

[20] H. Tang and I. P. Herman, Phys. Rev. B 43 (1991) 2299.

[21] S. B. Segletes and W. P. Walters, J. Phys. Chem. Solids 59 (1998) 425.

[22] P. G. Klemens, Phys. Rev. 148 (1966) 845.

[23] M. Balkanski, R. F. Wallis, and E. Haro, Phys. Rev. B 28 (1983) 1928.

[24] J. Menéndez and M. Cardona, Phys. Rev. B 29 (1984) 2051.

CHAPTER 10

A STUDY OF ENERGY BANDGAP VERSUS TEMPERATURE FOR Cu_2ZnSnS_4 THIN FILMS

10.1 Introduction

Temperature dependence of the electronic interband transition can provide valuable information concerning excitonic effects and electron–phonon interactions. Research, which discusses the effect of lattice vibration and the resulting shift of the energy levels for silicon, was reported by Fan, decades ago [1]. Since then, significant research has been accomplished to evaluate the effect of temperature on various semiconductors and photovoltaic materials. For example, optical absorption dependence on temperature for strongly quantized, low dimension semiconductor was reported by Pejova *et al.* [2]. Nepal *et al.* [3] utilized deep ultraviolet photoluminescence spectroscopy to study band gap temperature dependence in AlGaN. Rincon *et al.* [4] reported energy band gap temperature dependence of bulk crystals of $CuIn_3Se_5$ and $CuGa_3Se_5$. Hu *et al.* [5] reported band gap measurements for films grown by chemical solution based methods. Recently, Cu_2ZnSnS_4 (CZTS) and similar quaternary chalcogenides have received considerable attention due to a high absorption coefficient ($\sim 10^4$ cm^{-1}) and an optimal

fundamental band gap energy (~1.5 eV) [6-15]. However, the authors are not aware of research reported regarding the band gap temperature dependence of CZTS absorber material. It is important to note that the near band edge transition with respect to temperature is an important parameter for optimizing the performance with respect to operating temperatures of CZTS based photovoltaic devices, which can vary significantly daily and seasonally.

Amongst the reported band gap models three popular models have been evaluated in this study: (1) the Varshni model [16], (2) Pässler model [17] and (3) the Bose–Einstein model [18]. These models suggest that band gap shift in semiconductors as a function of temperature is mainly due to electron–phonon interactions. However, thermal expansion also plays a minor role, which was considered by several research groups. For example, Manoogian *et al.* [19] and [20] used a modified Varshni model to consider the effects of lattice expansion, and Rincon *et al.* [4] used the contribution of lattice dilation to evaluate the shift of band gap energy. In view of these issues, a study of fundamental energy band gap variation of CZTS thin films, (grown by electrodeposition and elevated temperature sulfurization) as a function of temperature has been performed. UV–Vis spectroscopy was utilized to measure band gap parameters. A comparative study between different models has been performed in order to determine the best model for CZTS from 77 to 400 K.

10.2. Experimental details

CZTS thin films were grown on a conducting transparent substrate by a solution based method. Cu–Zn–Sn layers were electrochemically grown. The Cu layer was deposited using a CN^- medium bath whereas zinc and tin were deposited using a Cl^- medium bath [10]. Thin films, coated with metal precursors (Cu, Zn and Sn), were sulfurized by annealing in a sulfur environment. Annealing was performed in an argon environment with evaporated elemental sulfur (99.99%) in a tube furnace for 2 h at ~560 °C.

Figure 10.1 shows a characteristic θ–2θ XRD pattern for a film after sulfurization. This pattern matches well with the kesterite structure of CZTS (JCPDS card 26-0575). Peaks corresponding to (1 1 2), (1 0 3), (2 0 0), (1 0 5), (2 2 0), (3 1 2), (2 2 4), (3 1 4), (0 0 8) and (3 3 2) planes were detected, revealing the polycrystalline nature of CZTS film. Raman analysis was also performed to distinguish phases. All three major peaks, which correspond to the CZTS phase, can be seen in the inset of Fig. 10.1[8]. No distinct peaks corresponding to impurity copper sulfide, zinc sulfide and tin sulfide were observed. The lack of peaks or shoulders for copper tin sulfide (CTS) at 355, 348, 351 and 295 cm^{-1} provides additional evidence of CZTS film purity [14]. Prior to transmittance measurements, elemental and morphological characterization of film was carried out using various techniques such as scanning electron microscopy, EDS, atomic force microscopy and ICP spectroscopy [10]. All elemental characterizations reveal that the elemental ratio of Cu:Zn:Sn is close to 2:1:1. Melting point testing showed that the film

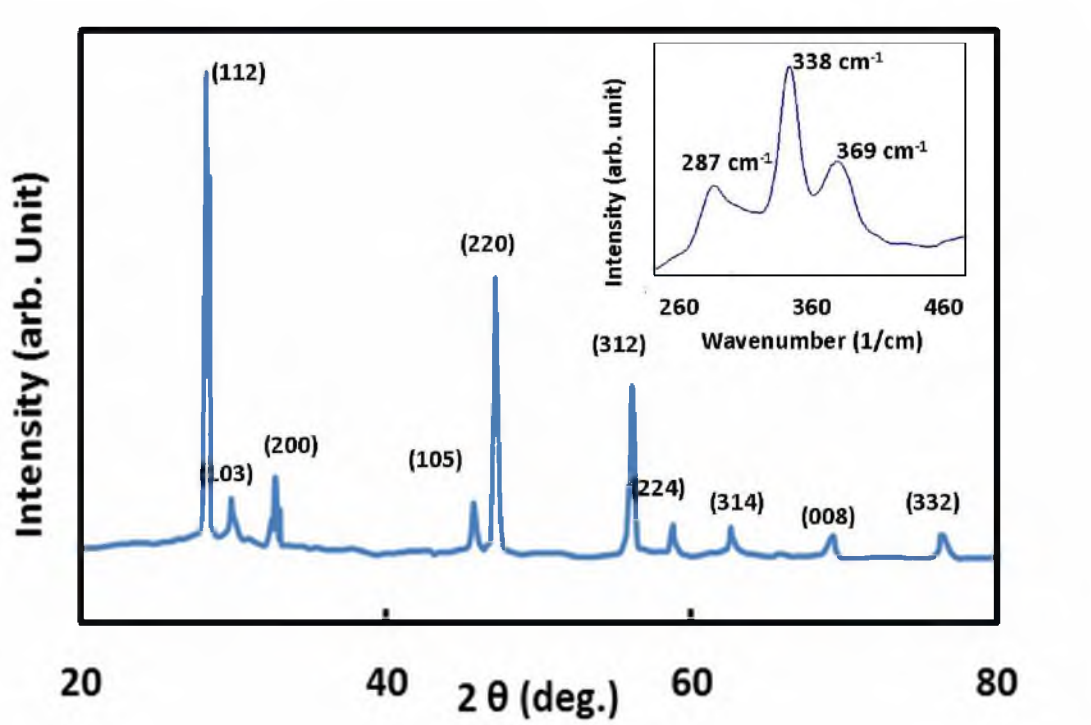

Figure 10.1: XRD pattern of CZTS thin film used for temperature dependent energy band gap measurements; Raman spectrum of CZTS thin film (shown in inset).

melted far above the melting point of CTS (~735 °C) and very near the melting point of CZTS (~820 °C) [21] and [22].

These observations suggest that films are relatively pure for band gap measurements. The surface morphology of film is found to be smooth with an average roughness of ~30 nm in most regions of the film. An AFM 3D micrograph (Figure 10. 2) of CZTS surface shows that height between lowest feature and highest feature is ~69 nm. Temperature sensitive transmittance measurements of CZTS film were done using a cryostat setup coupled with an Ocean optics spectrophotometer (see Figure 10.3), which is capable of measurements from 77 K to 450 K. The normalized transmittance data were utilized for

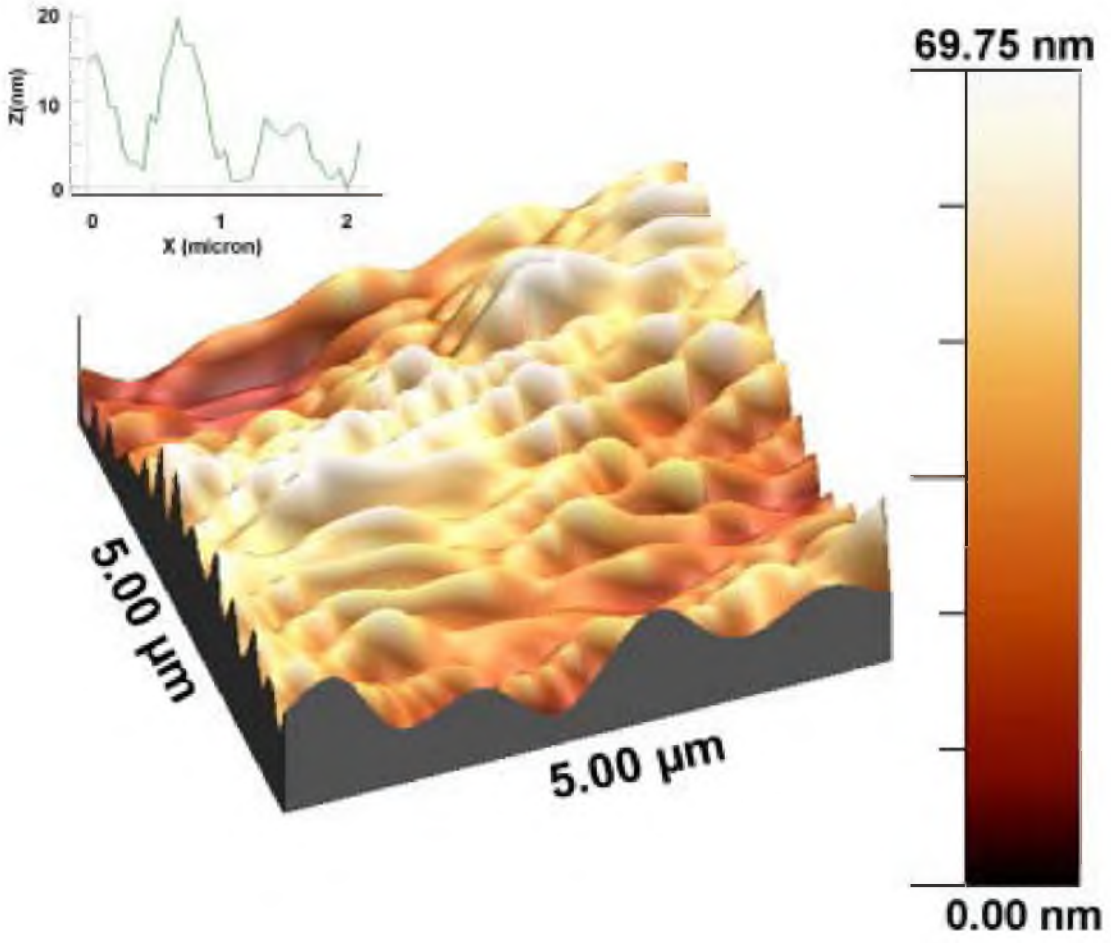

Figure 10.2: An AFM 3D micrograph of CZTS thin film (a roughness profile is shown in inset).

band gap energy evaluation [15]. The band gap energies of CZTS films were estimated by extrapolating the linear portion of graphs of $(\alpha E)^2$ versus energy to zero (Figure 10. 4) [10]:

$$\alpha = A(h\nu - Eg)^{1/2} \qquad (10\text{-}1)$$

The band gap at 0 K was obtained by extrapolating the band gap obtained near 77 K, using various models. Optical absorption spectra (and Tauc plot) generally reveal some evidence of defects (such as disordered semiconductor, joint density of states, indirect semiconductor property) by the presence of a largely exponential Urbach tail when defects are present. The authors carefully measured all transmittance data and did not find evidence of such defects. The observation also suggests that likelihood of weak bond

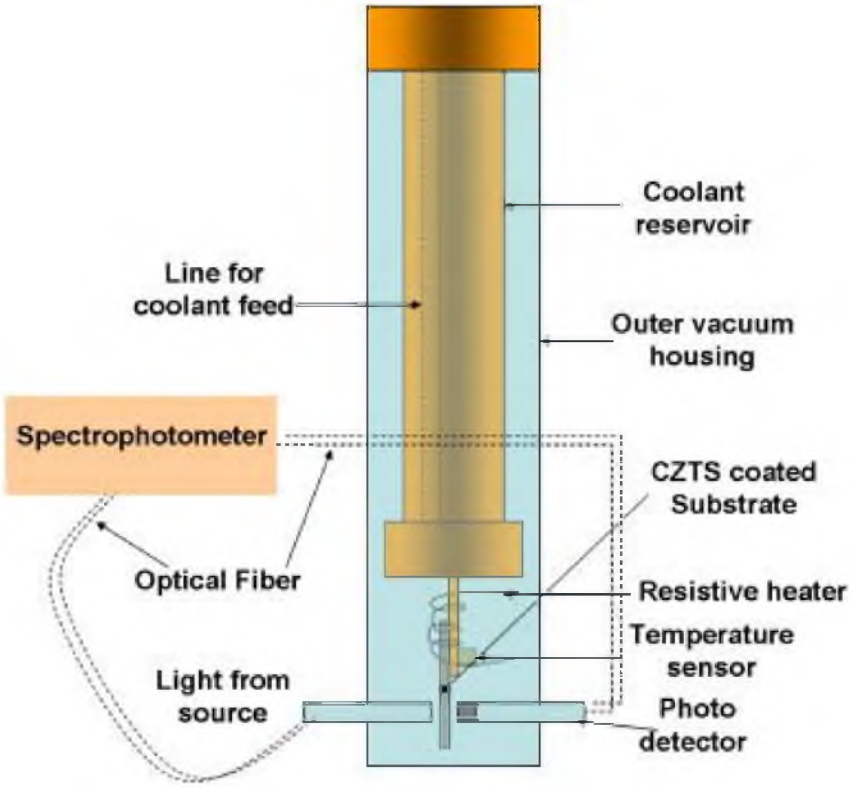

Figure 10.3: A Schematic diagram showing a portion of cryostat setup used for temperature sensitive band gap measurements.

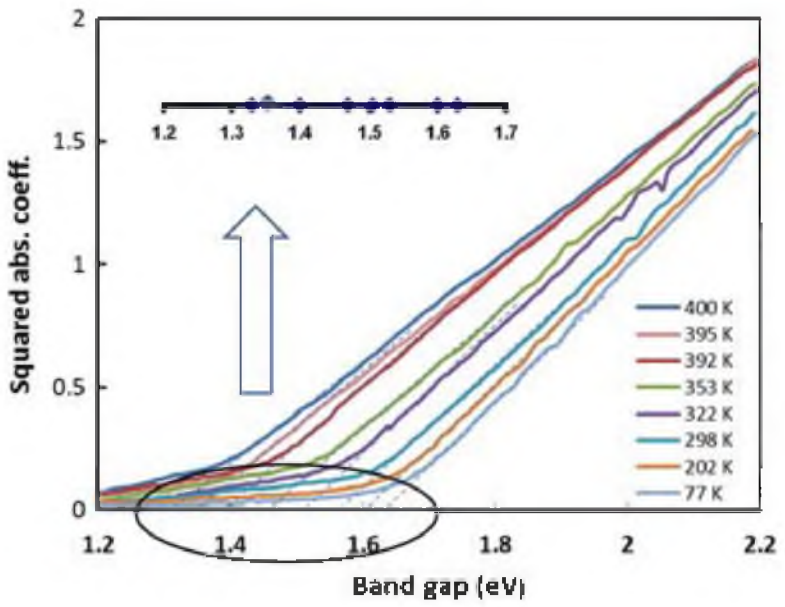

Figure 10.4: Squared absorption coefficient vs. band gap energy is shown for CZTS thin film at different temperatures.

density is also low. Possible exponential dependence of alpha on the photon energy was examined. Results show that possibility of the disorder is low.

10.3. Results and discussion

The effect of temperature on band gap energy decrease has been quantified through several empirical or semi-empirical relations. Among the empirical relationships, the Varshni relationship is often used to assess non-linear temperature dependent band gap shift. The Varshni [16] equation for the band gap variation as a function of temperature is

$$E_g(T) = E_g(0) - \frac{AT^2}{T+B} \qquad (10\text{-}2)$$

where A and B are fitting parameters, which are characteristic of a given semiconductor. Eg(0) is the band gap of the semiconductor at 0 K. The Varshni relation is a combination of quadratic low temperature asymptotic behavior with linear high temperature dependence [2] and [3]. Although this relation fits appropriately for various III–V and II–VI semiconductors, it gives negative values for the fitting parameters (A and B) for various known wide band gap semiconductors. Moreover, the physical significance of parameter B was not explained, which is believed to be related with the Debye temperature of the material [2] and [3]. Figure 10.5 shows experimental band gap shift as well as fitting using Eq. (2), based on the Varshni model. The values of fitting parameters A and B are 10.10×10^{-4} eVK^{-1} and 340 K, respectively, whereas Eg(0) was 1.64 eV. It can be seen that the Varshni relation fits well for low temperatures (up to 360 K); however, it shows deviation from experimental values, above 360 K.

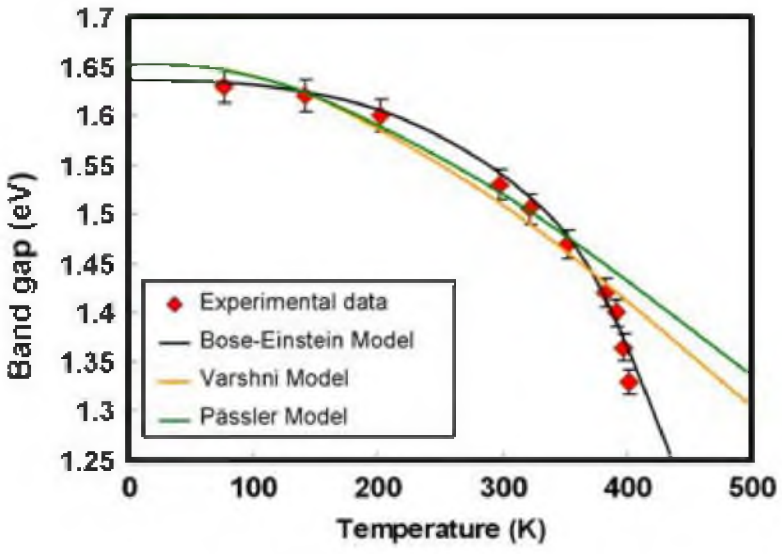

Figure 10.5: Experimental band gap energy vs. temperature; Fitting based on Varshni model, Pässler model and Bose–Einstein model is shown by continuous lines of different colors.

Another model, proposed by Pässler [17], considers a power law type spectral function, which is related to electron–phonon interaction. This model explains curvilinear behavior of band gap shift at moderate temperatures. It accommodates band gap shift resulting from contributions of phonons with various energies. The expression for band gap shift is given by [17]:

$$E_g(T) = E_g(0) - \frac{\alpha\Theta}{2}\left[\left(1+\left(\frac{2T}{\Theta}\right)^q\right)^{1/q} - 1\right] +$$

Contribution of thermal dilation (10-3)

Here Θ is a constant closely related with average phonon temperature, the parameter q=η+1, where η is shape factor of spectral function and α is the limiting slope of band gap shift at high temperatures [16]. Figure 10.5 includes experimental band gap and Pässler model data. The contribution of thermal dilation is ignored for simplicity. This model also fits well below 355 K; however significant deviation can be seen at temperatures above 350 K. The values of adjustable parameters obtained are: Θ=260 K; q=2.7 and $\alpha=7.7\times10^{-4}$ eVK^{-1}. The Debye temperature that is proportional to Θ, can also be estimated by a method described by Rincon *et al.* [4] The estimated Debye temperature is ~360 K.

The Bose–Einstein model, which considers electron interaction within crystals, also relates energy shift and temperature with Debye energy [18]. According to this model, the band gap energy can be determined from:

$$E_g(T) = E_g(0) - \frac{2a_B}{\exp\left(\frac{\Theta_E}{T}\right) - 1} \tag{10-4}$$

where a_B is a parameter associated with the strength of exciton–phonon interactions within the crystal; Θ_E is an average temperature (Einstein characteristic temperature) of phonons interacting with the electronic subsystem. The Debye temperature for an Einstein oscillator can be determined from the relationship: $\Theta_D=4/3\Theta_E$ [2]. Although the Debye temperature or Einstein temperature for CZTS based compounds or other similar quaternary chalcogenides is not readily available, available data for ternary compounds can be utilized for a rough estimation. According to Madelung [23] and Einstein [24], the Debye temperature Θ_D for solids can be expressed in terms of bulk modulus:

$$\Theta_D = C_B\left(\frac{h}{k_B}\right)\left(\frac{B_o V^{1/3}}{M}\right)^{1/2} \tag{10-5}$$

where C_B is a dimensionless parameter, K_B and h are Boltzmann's and Plank's constants, respectively, V is mean atomic volume of lattice, M is mean atomic weight per site and B0 is bulk modulus. Ca'ceres et al. [24] used this equation for the calculation of Debye temperature. They used a B_0 value at V=0.024 nm^3 which was found to decrease with increase in V. For CZTS, the value of available lattice parameters can be utilized for evaluation of V and M[12]. The resulting value of V is utilized to estimate the bulk modulus. The final estimated value of Debye temperature for CZTS is ~333 K. The CB value used for this calculation is $\sim 2.85\times10^7$[25].

A similar estimation can also be made based on the work of Hailing et al. [23]. This research explored various elastic constants for chalcopyrite type structures as well as the Debye temperature.

Debye temperature can be calculated by integrating over velocity space using the equation [26]:

$$\Theta_D = \left(\frac{9N}{4\pi V}\right)^{1/3}\left(\frac{h}{k}\right)\left[\int\left(\frac{1}{V_j^3}+\frac{1}{V_k^3}+\frac{1}{V_l^3}\right)\frac{d\Omega}{\pi}\right]^{-1/3} \quad (10\text{-}6)$$

where V_j, V_k and V_l are eigenvalues of the Christoffel equation, N/V corresponds to number of atoms per unit volume of lattice, Ω is the solid angle, k is the Boltzmann constant, and h is Plank's constant [26]. The value of the integral inside the bracket was calculated for known material such as $CdGeAs_2$ and is utilized to estimate the Debye temperature for CZTS. The N/V value for CZTS can be calculated based on reported data [12]. Based on Eq. (6), the Debye temperature for CZTS is ~349 K, which is close to that obtained from the Madelung–Einstein approximation (~333 K). Figure 10.5 shows the theoretical band gap shift using Eq. (4) together with the experimental band gap shift. It can be seen that this model shows the best fit for the entire temperature range examined. In contrast, other models reveal a significant deviation from the measured data above 350 K. The value of fitting parameter αB obtained from least squares fitting of the model to the measured data is 90.25 meV.

The Varshni equation is a second order approximation to the Bose–Einstein model, and it has been validated for a certain range of temperature [19] and [20]. However,

Bose–Einstein expression, a more generalized expression, best describes band gap shrinkage behavior of $CuInS_2$, whose crystal structure is quite similar to CZTS [27]. Bose–Einstein best fit for CZTS absorber suggests that a small shift of atoms or ion from balance sites (arises due to lattice vibration) will diminish lattice periodic field, which further affect chemical bond length and band gap energy [28]. The results also suggest that increase in temperature enhances the activated population of phonons in CZTS absorber material, which in turn causes more electron–phonon interaction. This interaction results in band gap shrinkage at elevated temperatures. Another possibility is domination of the dynamic part of electron–phonon coupling up to a certain range of temperature, which is not considered in the extended range of temperature in the Varshni equation. The Pässler model which considers some contribution of thermal dilation was ignored in fitting. Incorporation of this contribution will certainly improve fitting. The average band gap narrowing coefficient (dEg/dT) was $\sim -8.63\times10^{-4}$ eV/K (Bose–Einstein Model), -5.8×10^{-4} eV/K (Pässler model) and -6.6×10^{-4} eV/K (Varshni Model), respectively. A summary of fitting parameters is listed in Table 10.1.

10.4. Conclusions

In summary, the fundamental band gap relationship with temperature for CZTS thin film was measured using transmittance data from 77 to 410 K. Band gap data shows inadequate fitting with the Varshni model and Pässler model. The Bose–Einstein model best describes the band gap temperature dependence for CZTS, which can be understood

Table 10.1: List of various fitting parameters

Serial no.	Model or equation	Fitting parameter	Fitting parameter	Debye temperature	(dE_g/dT)
1	Varshni model	A=10.10×10^{-4} eVK^{-1}	B=340 K		−6.6×10^{-4} eVK^{-1}
2	Pässler model	q=2.7	α=7.7×10^{-4} eVK^{-1}	360 K	−5.8×10^{-4} eVK^{-1}
3	Bose–Einstein model	a_B=90.25 meV			−8.63×10^{4} eVK^{-1}
4	Eq. (5)			333 K	
5	Eq. (6)			349 K	

as existence of carrier–phonon coupling in CZTS. Estimated Debye temperatures obtained from various theories and approximations lie in close proximity to Debye temperatures obtained from fitting parameters determined from best fit Bose–Einstein and Pässler models. This information provides useful data for predicting the effect of temperature on CZTS band gap for solar cell applications that are affected by daily temperature variations.

10.5 References

[1] H. Y. Fan, Phys. Rev. 82 (1951) 900-9005.

[2] B. Pejova, B. Abay, and I. Bineva, J. Phys. Chem. C 114 (2010)15280.

[3] N. Nepal, J. Li, M. Nakarmi, J. Y. Lin, and H. X. Jiang, Appl. Phys. Lett. 87(2005)242104.

[4] C. Rincón, S. M. Wasim, G. Marin, and I. Molina, J. Appl. Phys. 93 (2003)780.

[5] Z. G. Hu, Y. W. Li, F. Y. Yue, J. H. Chu, and Z. Q. Zhu, Appl. Phys. Lett. 91 (2007) 221903.

[6] P. K. Sarswat, M. L. Free, and A. Tiwari, Mater. Res. Soc. Symp. Proc. Vol. 1315, Boston, USA, 2010.

[7] P. K. Sarswat, M. L. Free, and A. Tiwari, Mater. Res. Soc. Symp. Proc. Vol. 1288, Boston, USA, 2010.

[8] P. K. Sarswat and M. L. Free, Phys. Status Solidi A 208 (2011) 2861.

[9] P. K. Sarswat, M. L. Free, and A. Tiwari, Phys. Status Solidi B 248(2011)2170.

[10] P. K. Sarswat, M. L. Free, A.Tiwari, M. Snure, Thin Solid Films 520 (2012) 1694.

[11] H. Araki, Y. Kubo, A. Mikaduki, K. Jimbo, W. S. Maw, H. Katagiri, M. Yamazaki, K. Oishi, and A. Takeuchi, Sol. Energy Mater. Sol. Cells 93 (2009)996.

[12] S. Chen, X. G. Gong, A. Walsh, and S. H. Wei, Appl. Phys. Lett. 94 (2009)41903.

[13] P. A. Fernandese, P. M. P. Salomé, and A. F. D. Cunha, Thin Solid Films 517(2009)2519.

[14] P. A. Fernandese, P. M. P. Salomé, and A. F. D. Cunha, Phys. status solidi C 7(2010) 901.

[15] N. Kamoun, H. Bouzouita, and B. Rezig, Thin Solid Films 515 (2007)5949.

[16] Y. P. Varshni, 34 (1967)149.

[17] R. Pässler, Phys. status solidi B 200 (1997)155.

[18] P. Lautenschlager, M. Garriga, S. Logothetidis and M. Cardona, Phys. Rev. B 35 (1987) 9174.

[19] A. Manoogian and A. Leclerc, Can. J. Phys. 57(1979)1766.

[20] A. Manoogian and J. C. Wooley, Can J. Phys 62 (1984) 285.

[21] G. H. Moh, Chem. Erde 34 (1975)1.

[22] S. Fiechter, M. Martinez, G. Schmidt, W. Henrion, and Y. Tomm, J. Phys. Chem. Solids 64 (2003)1859.

[23] E. Madelung , Phys. Z. 11(1910)898.

[24] A. Einstein, Ann. Phys. (Leipzig) 34, (1911)170.

[25] J. Cáceres and C Rincón, Phys. status solidi B 234 (2002) 541.

[26] T. Hailing, G. A. Saunders, W. A. Lambson, and R. S. Feigelson, J. Phys. C: Solid State Phys. 15, (1982)1399.

[27] M. V. Yakusheva, A. V. Mudryi, I. V. Victorov,J. Krustok, and E. Mellikov, Appl. Phys. Lett. 88, (2006) 011922.

[28] J. Yang, Y. Q. Gao, J. Wu, Z. M. Huang, X. J. Meng, M. R. Shen, J. L. Sun, and J. H.Chu, J. Appl. Phys. 108 (2010)114102.

CHAPTER 11

CONTACT ENGINEERING FOR THE Cu_2ZnSnS_4-ALTERNATIVE BACK CONTACT: A PRELIMANRY EVALUATION

11.1 Introduction

Electrical contact engineering of Cu_2ZnSnS_4 (CZTS) absorber material has been investigated using metals with a wide range of work functions and a fluorinated tin oxide (FTO) substrate. A significant difference in barrier height-work function relationships was observed when CZTS/metal device was fabricated by two different methods. Such behavior of the metal (or FTO)/CZTS contact interface is explained on the basis of 'Fermi level depinning. This depinning arises in this study due to the presence of an ultrathin, interfacial sulfur layer grown during elevated temperature sulfurization. A detailed investigation based on various experimental results and available models has been discussed in this chapter.

Copper zinc tin sulfide (CZTS) is emerging as a wide bandgap quaternary chalcogenide for use in inexpensive and environment friendly thin film solar cells [1,2]. Although significant research for efficiency improvement of CZTS devices has been accomplished over the last decade, contact engineering of CZTS-back contact, a key factor for high performance photovoltaic devices, is not fully understood. An ohmic

contact between kesterite or chalcogenide absorber and back contact is desirable for good solar cell performance [2, 3]. In most of the cases Mo has been utilized as back contact. It is advantageous to use Mo because formation of $MoSe_2$ / MoS_x promotes barrier height lowering [2,3,4]. Although CZTS-Mo band alignment and ohmic behavior can be explained on the basis of a nonideal charge transfer mechanism, little information is available for CZTS-M ('M' represents various back contact materials and FTO (not Mo)) band alignment. Because of various advantages of FTO, it has been recently utilized for CIGS and CZTS in superstrate and bifacial configurations, respectively [5, 6]. It was also reported that CZTS growth on various alternative metal contacts is viable [7]. A study of CZTS-M contact will provide more details related with fundamental properties such as Fermi level pinning and barrier height modulation. Hence, it is essential to examine CZTS-M contact behavior.

11.2 Experiments

To investigate CZTS-M contact behavior, *J-V* characteristics were examined. In these experiments a CZTS layer was grown on a substrate by two different methods. In method (1), CZTS layer was grown by electrodeposition-annealing while in method (2) CZTS nanoparticles were grown separately using hot injection [8] and immobilized on substrate of interest. In some cases (such as Ti and Cu), it was not possible to fabricate device using method (1). None of the samples were selenizied in these experiments. Details of experiments for these methods are discussed elsewhere [1,8]. The simulation of dark *J-V* characteristics for many of these devices was done using a one diode model with

reverse saturation current J_o and diode ideality factor n. The Schottky barrier height can be extracted using this model. The current is given as [5]:

$$J = J_o\left[\exp\left\{\frac{q(V - JR_S}{nkT}\right\} - 1\right] + \frac{V - JR_s}{R_P} \tag{11-1}$$

The dark saturation current depends on barrier height (ϕ_B), absolute temperature (T) and saturation current density pre-factor (A).

$$J_o = A^* T^2 \exp\left(\frac{-q\phi_B}{kT}\right) \tag{11-2}$$

where k is the Boltzmann constant, q is the electronic charge, n is the diode quality factor, R_s and R_p are parasitic series and parallel resistances. Various fitting parameters were extracted and summarized in Table 11.1.

11.3 Results and discussions

Figure 11.1 shows that low work function metal such as Al forms a rectifying contact with CZTS. It can be seen that an Al-CZTS device exhibits good thermionic behavior and follows the one diode model given by equation (2). A similar behavior was observed for Mg-CZTS device. On the other hand, a relatively high work function material such as Ni shows ohmic behavior (Fig. 11.2) when CZTS layer was grown by method (1). It is also important to observe that Fe, Co, Pd, and Au form ohmic contact with CZTS, when CZTS is grown by method (1). However, both Fe and Co showed quasi-ohmic behavior when CZTS layer was grown by method (2). In the case of FTO-CZTS, ohmic contact was not observed for all cases. In some cases *J-V* (Figure 11.3)

Table 11.1: Metal/CZTS diode parameters

Metal	Barrier height (eV)	Ideality Factor (n)	Series Resistance R_s (Ω)	A	Method of device fabrication	Parallel conductance G_P ($1/R_P$)
Al	0.89	1.95	12	140	Nanoparticle coating	5.8×10^{-4}
Al	0.87	1.95	13.5	140	Electrodeposition-sulfurization	5.6×10^{-4}
Cu	0.80	1.41	0.70	140	Nanoparticle coating	3.5×10^{-2}
Ti	0.82	1.50	5.0	140	Nanoparticle coating	3.8×10^{-3}
Co	Ohmic contact	-	16.0	140	Electrodeposition-sulfurization	-
Co	0.79	1.41	5.0	140	Nanoparticle coating	2.1×10^{-3}
Fe	0.20	1.45	30	140	Electrodeposition-sulfurization	3.6×10^{-3}
Ni	0.69	1.51	14	140	Nanoparticle coating	3.5×10^{-2}
Ni	Ohmic contact	-	25	140	Electrodeposition-sulfurization	-

characteristics reveal rectifying behavior, while in some cases it is close to tunneling behavior (Figure 11.4). The barrier height (ϕ_B) versus metal work function (ϕ_m) graph is shown in Figure 11.5. The values of work function were taken from literature [10]. A linear behavior, given by following relation [2]: $\phi_B = IP - \phi_{CNL} + S(\phi_{CNL} - \phi_m)$ is validated, where $S = \frac{\partial\phi}{\partial\phi_m}$ is Schottky barrier interface parameter and IP and ϕ_{CNL} are the semiconductor ionization potential and charge neutrality level respectively (measured from vacuum level). From linear fitting of experimental data, we obtained S = 0.19 (method 2) and S = 0.98 (method 1).

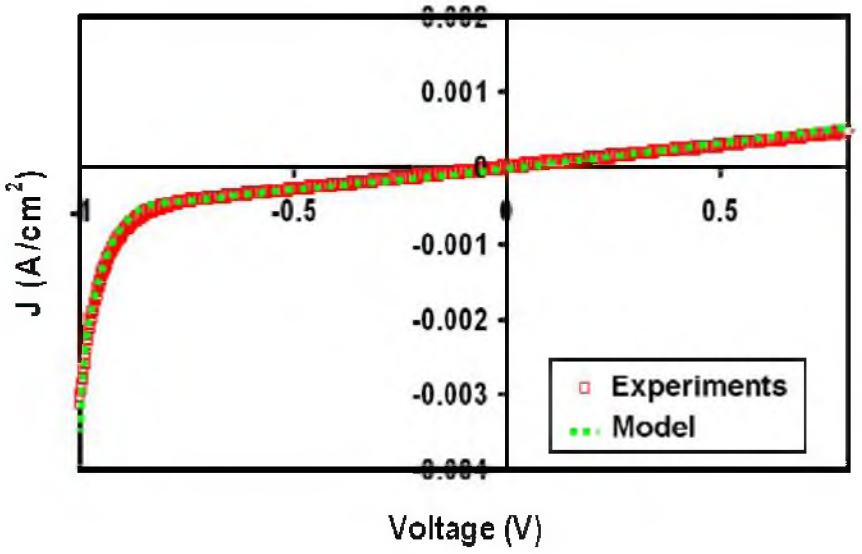

Figure 11.1: J-V characteristics for Al/CZTS device (grown by method 2).

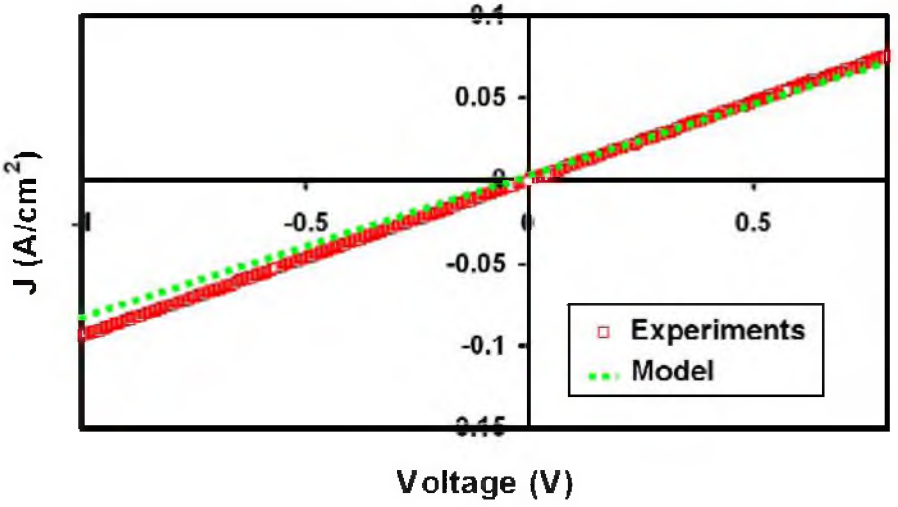

Figure 11.2: J-V characteristics for Ni/CZTS device (grown by method 1).

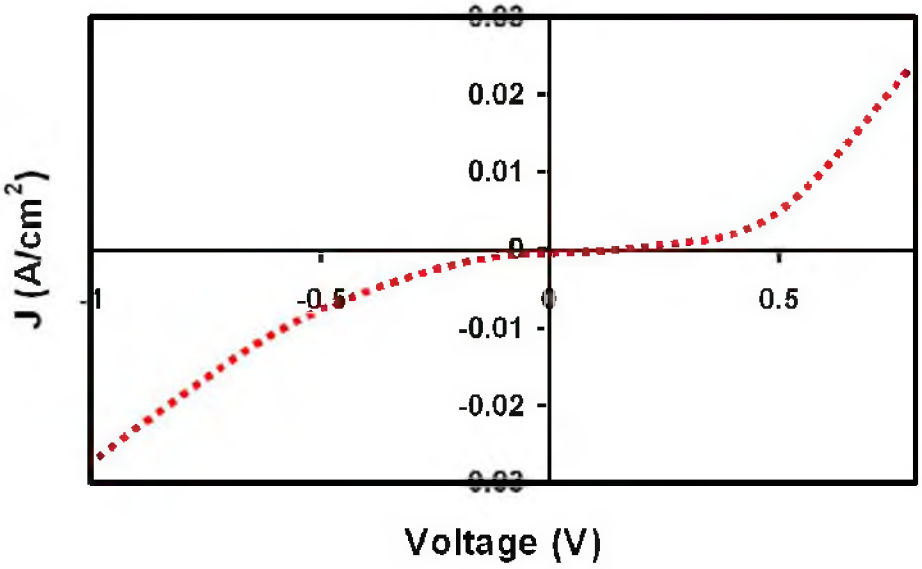

Figure 11.3: J-V characteristics for FTO/CZTS device (grown by method 1).

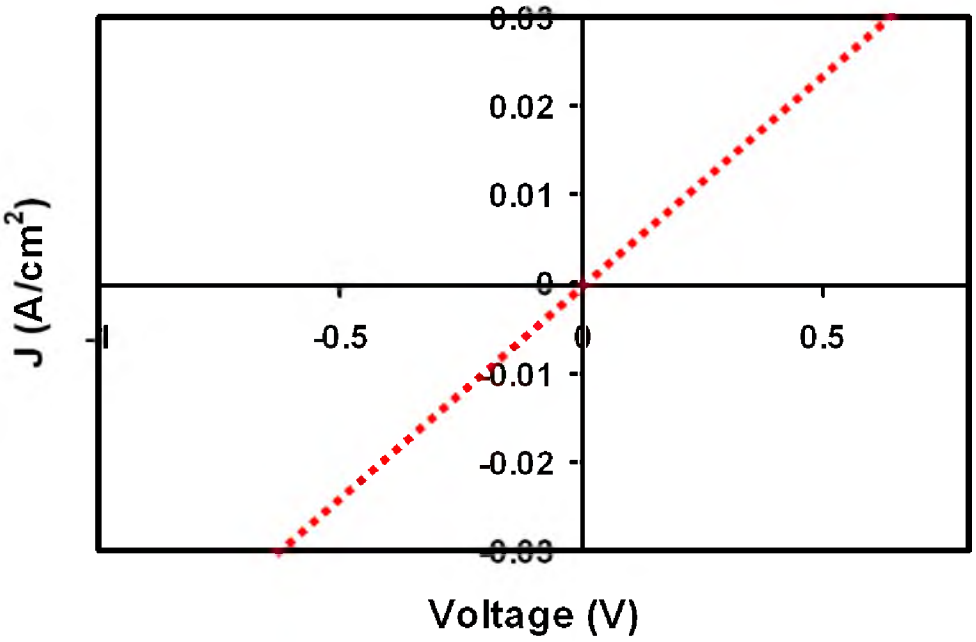

Figure 11.4: J-V characteristics for FTO/CZTS device (grown by method 1).

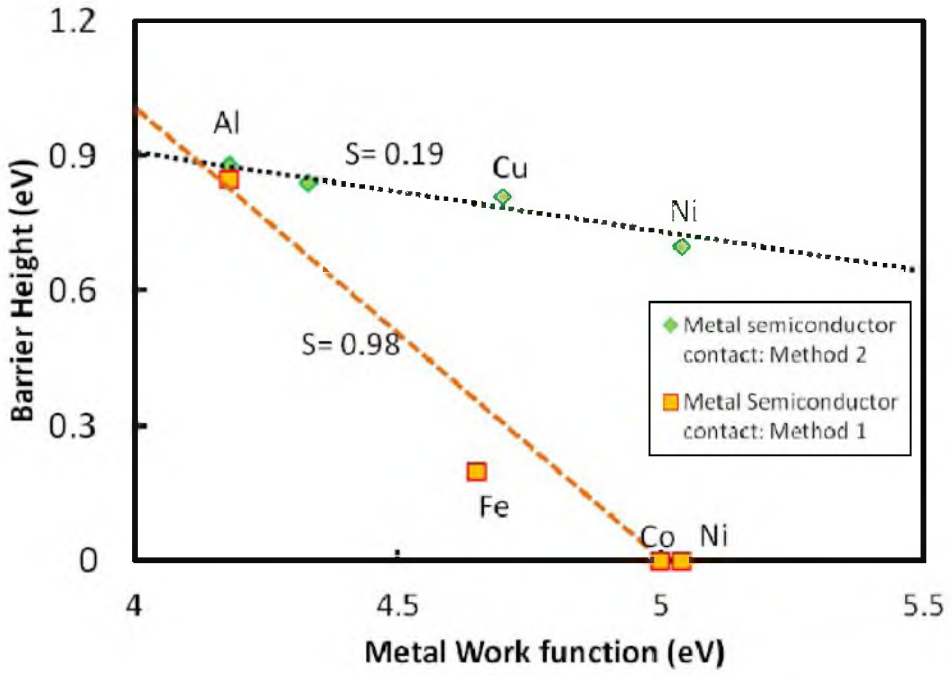

Figure 11.5: Barrier height vs. metal work function graph for CZTS/M device, grown by two different methods. In method-1, CZTS layer was grown by electrodeposition-annealing while in method -2 CZTS nanoparticles were grown separately and immobilized on substrate of interest.

The value of 'S' can also be calculated using following empirical relation [3]:

$$S = \frac{1}{1 + 0.1(\varepsilon - 1)^2}, \qquad (11\text{-}3)$$

where 'ε' is high frequency dielectric constant for semiconductor. Using value of 'ε' from literature [9], S ~0.21 was obtained for CZTS, which closely matches with that obtained from fitting (method 2). The relative low value of S ~ 0.19 indicates that schottky barrier height is not much dependent on metal work function. This observation is an indication of apparent pinning of Fermi level at interface [11]. However, when CZTS-metal device was fabricated using method 1, the value of S is ~ 0.95, which is very close to ideal Schottky limit [11]. Based on this observation, it can be said that method (1) promotes Fermi level depinning.

An understanding regarding the difference in method of CZTS growth on back contact material is essential to explain the fact behind different contact behavior. There is least possibility for presence of interfacial sulfur and other associated possible secondary phases (containing back contact material), when device is fabricated by method (2). However, method (1) utilizes direct sulfurization of metallic layer at elevated temperature; hence it is more prone to produce such phases as well as a passivation layer containing sulfur. It has been shown that by varying the thickness of an insulating layer between metal and semiconductor, contact behavior can be modified [12]. Sarswat *et al.* [7] reported the formation of a passivation layer on FTO substrate after sulfurization. Raman spectroscopy of this layer was carried out by removing the CZTS layer and comparing it with the Raman spectrum of an FTO coated glass substrate.

The Raman spectrum in Figure 11.6 shows major peaks at 218 and 471 cm^{-1}. The observed spectrum closely matches with Raman spectra of rhombic sulfur crystals. The peaks centered at 218 cm^{-1} and 471 cm^{-1} correspond to the A_1 mode of vibrations [13]. These peak positions are different than the positions of Raman peaks for FTO films coated on glass substrate [14]. Indeed this observation suggests the presence of a sulfur layer on FTO substrates, which can cause a change in barrier height and, therefore, current transport between conductor-semiconductor junctions. In this situation current flow is predominantly due to tunneling [12]. It can be seen that a very small change in thickness of interfacial layer ~ 2nm, causes a change in *J-V* characteristics of the junction [11,12]. A similar change, which is observed for the CZTS-back contact interface is possibly due to non uniform thickness of interfacial layer. *J-V* behaviors of various FTO-CZTS devices were recorded to strengthen this assumption for cases with different extents of sulfurization. Most of the CZTS films which were grown at moderate sulfurization condition (using method (1)) showed ohmic behavior while tunneling behavior was observed for most films grown at excess sulfurization. This phenomenon can be understood as superimposition of two competing mechanisms. The density of metal induced gap state (MIGS) reduces when interfacial sulfur layer thickness increases up to a certain range [12]. However, tunneling resistance increases as sulfur layer thickness increases beyond a certain range. Hence, there is a minimum optimal thickness at which CZTS-M shows ohmic behavior. The reasoning behind sulfur sandwiched between CZTS and back contact material is not fully evaluated. It is anticipated that the polycrystalline nature of as-deposited films promotes fast diffusion of sulfur [15]. The grain boundaries are pathways for such diffusion. A regional non-stoichiometric sulfidiz-

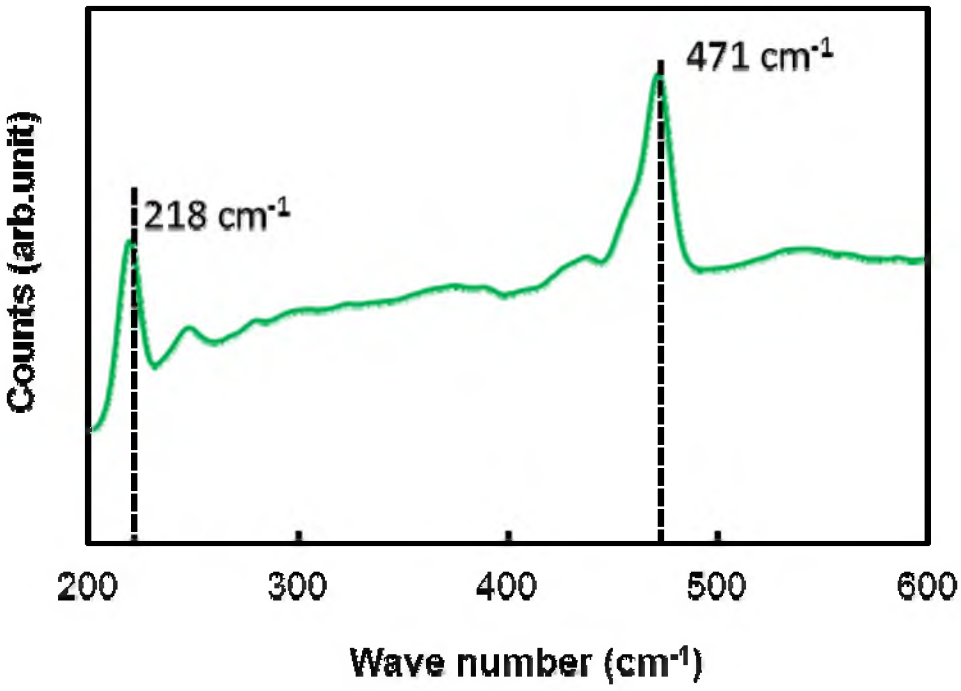

Figure 11.6: Raman spectra of FTO film that was underneath of CZTS layer.

-tion can cause accumulation of sulfur along the interface. The randomness in *J-V* behavior of CZTS-back contact can be originate from polycrystalline CZTS-back contact interface, where there is existence of different bonding geometry at different place, which lead to locally varying interface dipole [16].

11.4 Conclusions

In summary, contact engineering of CZTS with various alternative back contact materials was investigated. It was observed that CZTS-M device fabricated using electrodeposition- elevated temperature sulfurization is more prone to alter the Schottky barrier height as compare to device fabricated by nanoparticle (synthesized separately) coating. For FTO/CZTS device, current transport mechanism showed tunneling behavior, whereas in some cases ohmic behavior was observed. Although contacts are described based on barrier height and symmetricity of the *J-V* curve, still there is an absence of boundary between space charge limited and injection current regime. The ohmic behavior is an intermediate region between these two extreme cases. The moderate sulfurization condition also depends on various parameters such as thickness of as-deposited film, duration of sulfurization and sulfurization temperature. It may be possible that moderate sulfurization conditions for thick as-deposited films are excess sulfurization conditions for thin films. The quaternary nature of CZTS and hence possible various secondary phases, which were not detected by techniques used in this work can modulate contact behavior. Techniques such as Ballistic electron emission microscopy will provide more detailed insights of band bending and alignment.

11.5 References

[1] P. K. Sarswat, M. Snure, A.Tiwari, M.L.Free, Thin Solid Films 520 (2012) 1694.

[2] K. Wang, O. Gunawan, T. Todorov, B. Shin, S. Chey, N. Bojarczuk, D. Mitzi, S. Guha, Appl. Phys. Lett 97 (2010) 143508.

[3] J. Spies, R. Schafer, J. F. Wager, P. Hersh, H. Platt, D. Keszler, G. Schneider, R. Kykyneshi, J. Tate, X. Liu, A. D. Compann, W. N. Shafarman, Sol. Energy. Mat. Sol.Cells. 93 (2009)1296.

[4] J. H. Scofield, A. Duda, D. Albin B. L. Ballard, P. K. Predecki, Thin Solid Films 260 (1995) 26.

[5] F. J. Haug, D. Rudmann, A. Romeo, H. Zogg, A. N. Tiwari, 3rd World Conference on Photovoltaic Energy Conversion, May 11-18, 2003, Osaka, Japan, pp-2853-2858.

[6] P. K. Sarswat, M.L.Free, Phys. Status Solidi A 208 (2011) 2861.

[7] P. K. Sarswat, M. L. Free, and A. Tiwari, Mater. Res. Soc. Symp. Proc. Vol. 1315, Boston, USA, pp. mm07.

[8] Q Guo, H. W. Hillhouse, R Agrawal, J. Am. Chem. Soc. 131 (2009) 11672.

[9] C. Persson, J. Appl. Phys. 107 (2010) 053710.

[10] CRC Handbook of Chemistry and Physics, 59th ed. (CRC, West Palm Beach, FL, 1978), pp. E81-82.

[11]A. V. Thathachary, K. N. Bhat, N. Bhat, and M. S. Hegde, Appl. Phys. Lett. 96 (2010) 152108.

[12] Z. Liu, M. Kobayashi, B. C. Pal, Z. Bao, Y. Nishi, Phys. Rev. B 82 (2010) 035311.

[13] A. T. Ward, J. Phys. Chem. 72 (1968) 4133.

[14] R. Chandrasekhar, K.L. Choy, J. Cryst. Growth 231 (2001) 215.

[16] A. J. Cheng, M. Manno, A. Khare, C. Leighton, S. A. Campbell, E. S. Aydil, J. Vac. Sci. Technol. A 29 (2011) 051203.

[17] R. T. Tung, Phys. Rev. Lett. 84 (2000) 6078.

CHAPTER 12

CONCLUSIONS AND FUTURE RESEARCH

In this dissertation, alternative back contact materials were utilized for CZTS thin film growth using a variety of techniques. FTO, a transparent conducting oxide, was used extensively as the alternative back contact. One of the advantages of FTO is its highly transparent nature, which allows sunlight to pass through the whole device. This enables utility of CZTS-FTO photovoltaic device for bifacial solar cell applications. Techniques such as sequential electrodeposition, co-electrodeposition, and spin coating were used to grow a metal presursor layer, which was subsequently annealed in an evaporated elemental sulfur environment to obtain CZTS.

Photoelectrochemical examination of CZTS film grown on FTO coated glass was done using europium redox couple, which revealed that CZTS films exhibit photocurrent response for front and rear illumination. This result suggests that there is potential for CZTS-FTO bifacial photovoltaic device development. However, increase in sheet resistance of FTO is one of the challenges, which should be controlled by adjusting processing parameters. A comparative study was also done to examine properties of co-electrodeposited-diffusion annealed CZTS films grown on FTO and molybdenum

substrate. Mott-schottky analyses of films suggest that doping density of both films are ~ $10^{15}/cm^3$. Photoelectrochemical response exhibited by the films grown on molybdenum substrates is greater than that obtained for film grown on FTO substrates. The experimental investigation and simulation of the J-V characteristics of illuminated CZTS-electrolyte junctions was carried out at different illumination levels.

Temperature dependent Raman study showed that the Raman data for the "A" mode of vibration, the strongest peak for kesterite CZTS films, fit very well to a damped harmonic oscillator (DHO) model. An energy band gap-temperature study was conducted for CZTS thin film. The Bose–Einstein model best describes the band gap temperature dependence for CZTS, which can be explained based on the existence of carrier–phonon coupling in CZTS.

Electrical contact behavior for CZTS-FTO was also investigated. Preliminary results suggest that current-potential behavior can be modified by controlling growth technique, sulfurization parameters, and the substrate. Some experiments to complete photovoltaic device fabrication, using FTO, were conducted. More experiments related to complete photovoltaic device fabrication using environmentally friendly n-type buffer layer and an understanding of contact engineering of various layers are needed.